From single-cell to whole-body: developing a molecular neuroscience toolkit

Thesis by

Nicholas C. Flytzanis

In Partial Fulfillment of the Requirements for

the degree of

Doctor of Philosophy

CALIFORNIA INSTITUTE OF TECHNOLOGY

Pasadena, California

2019

Defended September 10th, 2018

Nicholas C. Flytzanis
ORCID: 0000-0002-7921-9392

ACKNOWLEDGEMENTS

First and foremost, I want to thank my Ph.D. advisor, Dr. Viviana Gradinaru. When I first came to graduate school, I had no idea what I wanted to study. I had some vague ideas in my mind about protein engineering and synthetic biology, and had I not met her, my career would have taken a very different path. Not worse, just different. Most people have an idea of what they want to work on, and end up, if not in the lab they had originally set out to join, in a lab doing something similar. I enrolled at Caltech with no background in neuroscience and ended up joining a lab whose stated goal was to study rodent behavior. All it took was a single seminar, at the start of my first semester. I will never forget that seminar, as it is not unreasonable to say that that it changed the course of my life. In that one seminar, on clear display, were three things: 1) First and foremost, Viviana's passion, drive, and love for what she did. I wanted to feel the same passion for my own work, and here was someone I could observe, learn from, emulate. 2) Second, I could see someone who cared about other people. She wasn't just up there, talking about what she was interested in and what she wanted to do. She was up there hoping to convert people to her cause. She wanted them to love her science as much as she did. She answered questions, however asinine, with patience and understanding. 3) Oh, and it doesn't hurt that the science was really, REALLY cool. Within a few days, I was in her office asking to rotate in her lab. I was the first to rotate in her lab, and I'd like to think that she also saw something in me and didn't just need new students! I couldn't have asked for a better, more supportive mentor, and in everything I do and accomplish from here on out, a large part is due to her.

Before I acknowledge those that have played a role in my scientific development throughout my Ph.D., I need to mention some people that played a role on a personal level, as I believe that no Ph.D. is successful without the support of external factors. Thankfully, a lot of the good friends I have made along the way have also contributed to my scientific successes.

First, Dr. Ken Chan. While we began as first year graduate students together, you finished a year before me, and have since gone on to greener pastures. Our paths were ever parallel, and I'd like to think that we carried each other for parts of the way. At least I know you did for me. Same year, same department, same lab, same scientific interests. Same

taste in food, same taste in music, many of the same likes and dislikes. I couldn't possibly ask for a better friend and scientific peer, all wrapped in one. Not few were the times that I looked toward you for support, both personally and scientifically. Not often do you find someone who can both be there at 4 in the morning when you need to complain about something, and there the next day at the bench when you need help with an experiment. You were always there, and one of my deepest hopes is that this will continue. If we can avoid competing with each other, that is!

Dr. Nick Goeden. I don't even know where to begin about this guy. Many around us joke that we are the same person…and oftentimes the line does become a bit blurred. Same name, same interests, same lab bench at times…heck…almost the same birthday (he's 2 days older). While I didn't get to know you until my Ph.D. was in its waning years, it feels like we've worked together all along. At any given moment, we are probably thinking the same exact thing about whatever is going on…best expressed by a single look. Even when we disagree, we just end up convincing one another. And at every moment, we push each other to accomplish more. Thankfully, I don't have to worry about not working with you any more, since I think we have a bright scientific future together. In all seriousness, though, we should probably spend less time together…

One more person I need to mention on both a personal and professional level is Dr. Jennifer Treweek. You're an inspiration. Whatever you do, you devote yourself to it fully…something I envy and aspire to in my own life. From reading a paper for journal club (yeah, she's the one that will read 10 other papers to get more background material), to taking care of pets and loved ones (she's spent more money on her cat than most people would spend on food for a family of four), to mixing cocktails (I will always defer to you on this), to pranking labmates (I refuse to get a license plate that says CAGELVR…). Always continue living life a quarter mile at a time.

Next, I want to thank some people that have been instrumental to my scientific adventure throughout the years, instilling knowledge, collaborating, or just plain providing comic relief. Dr. Claire Bedbrook and I wrote our first paper together. Working with you was both a pleasure and one of the most daunting tasks of my life, due to your intensity. You are going to achieve great things in your life. Just don't forget about "Closing Time

Radio". Bin Yang, we grew apart over the years, but I will always be thankful for your role in my first few years at Caltech. Not only did you walk me into Viviana's office to talk to her about rotating ("You have to join this lab" – Bin Yang, without even knowing me), but you were instrumental in all our experiments working throughout the first few years. If you hadn't set up the lab, no one would have gotten anything done. Greg Stevens, my first undergraduate student, inspired me to be a better scientist. To this day, I have yet to meet anyone with as much potential. As a junior undergraduate, he was holding scientific conversation and performing experiments up there at a post-doc level…it made you ask yourself, what am I doing if this undergrad is at this level? I can't wait to see the things you achieve. Ryan Cho, both my introduction to all things Korea, as well as an impressive and inspiring scientist in his own right. I've never seen anyone accomplish so much, while making it look like he does nothing at all. Dr. Alon Greenbaum, who came to our lab without knowing a single thing about Biology, and by asking all the questions he was never embarrassed to ask, made us all second guess what we knew and look at things in a new light. Plus, I've never met someone who's more of a straight shooter. If I ever need to be told how something is, I know where to go. Dr. Max (Maxellende: yes, I know what your full name is!) Ezin, another person I didn't have the pleasure of meeting until late in my Ph.D., but who has had a tremendous impact on me in a short time. Thank you, both for your belief in me, but also for cutting through my BS. You not only introduced a whole new world of chickens to me, but also taught me to be a better person. Like Alon, I can always expect you to tell me when I'm being an idiot, and that is invaluable. Last, and FAR from least, Dr. Benjamin Deverman. I aspire to one day be the scientist that you are, in terms of knowledge, passion and selflessness. You ended up introducing me to the science that I love the most, and I hope one day to be worthy of it.

I also want to thank the members of my committee, Dr. David Anderson, Dr. Frances Arnold, Dr. Mikhail Shapiro, and Dr. Markus Meister on my candidacy committee. I am extremely grateful for your support, your input, and sometimes your harsh criticism. You are all pinnacles in your fields, and tremendous inspiration.

Over the years, there have been countless collaborators, labmates, and friends, and each one of them has played a role, large or small. I couldn't ever hope to name them all,

but every single one of them has left an impression on me and shaped who I have become. I thank you all.

Finally, I want to thank my wonderfully supportive parents, Kostas and Semie, and my aunt and uncle, Miretta and Gregory, without whom I wouldn't be here today. You all set me out on the path I have taken and nurtured it to its completion. I wouldn't be the person, nor the scientist, I am today without you. My mom has a story she likes to tell: When I was very young, and after seeing her spending long nights in her office writing proposals, I took to saying: "I want to grow up to be a doctor. Not the kind in the hospital, but the kind that writes grants!" Well, Mom, that day has come. I will forever be thankful.

ABSTRACT

Throughout my Ph.D. I have worked on technology development, at first to answer basic scientific questions and eventually for therapeutic applications. This technology development applied to a variety of fields, from neuroscience to development to gene therapy, and acted upon biological systems in a wide range of scale, from the single-cell monitoring to organism-wide gene-transfer. My graduate research began with the engineering of microbial rhodopsin spectral properties and fluorescence. By making use of their ability to absorb light and emit fluorescence in a voltage-dependent manner, I aimed to interrogate neuronal activity during behavior at the single-cell level. That line of research ended with publication of the voltage-sensor Archer, which I used to track activity of a single cell *in vivo* in awake, behaving worms. I then shifted from tracking activity at the single cell level, to visualizing entire organisms, by developing clearing techniques that enable a high-resolution, three-dimensional analysis of a diverse range of tissues. I began by optimizing tissue-clearing parameters for various tissue types and a wide variety of experimental needs. I then took that knowledge and applied it to visualizing and tracking the developing neural crest in cleared, whole-mount chicken embryos, discovering some unexpected derivates. Finally, I became interested not only in visualizing entire organisms, but in developing technologies to facilitate gene transfer throughout the body. The rapidly growing field of gene therapy is in constant need of new tools that target specific tissues, avoiding off-target effects. The end of my Ph.D. has been spent engineering viruses that can be delivered body-wide, but target only specific areas of therapeutic interest, like the brain and lungs.

PUBLISHED CONTENT AND CONTRIBUTIONS

[1] Ezin, M.*, Flytzanis, N. C.* et al. “Bringing CLARITY to the classics: embryonic neural crest contribution in 3D”. *In preparation.*

N.C.F designed and performed experiments, analyzed the data and helped write the manuscript.

[2] Flytzanis, N. C.*, Goeden, N. S.*, Deverman, B. E., Gradinaru, V. “Engineering tissue-specific AAVs for gene therapy”. *In preparation*.

N.C.F helped conceive the project, designed and performed all experiments, analyzed the data and wrote the manuscript with support from all authors.

[3] Gradinaru, V., Flytzanis, N. C. (2016). “Neuroscience: Fluorescent boost for voltage sensors”. In: *Nature* 529(7587), pp. 469-70. doi: 10.1038/529469a.

N.C.F helped write the manuscript.

[4] Treweek, J. B. et al. (2015). “Whole-body tissue stabilization and selective extractions via tissue-hydrogel hybrids for high-resolution intact circuit mapping and phenotyping”. In: *Nature Protocols* 10(11), pp. 1860-1896. doi: 10.1038/nprot.2015.122.

N.C.F. designed and performed experiments, analyzed the data and prepared figures.

[5] Engqvist, M. K. et al. (2015). “Directed evolution of Gloeobacter violaceus rhodopsin spectral properties”. In: *Journal of Molecular Biology* 427(1), pp. 205-20. doi: 10.1016/j.jmb.2014.06.015.

N.C.F. performed experiments.

[6] Flytzanis, N. C.*, Bedbrook, C. N.* et al. (2014). “Archaerhodopsin variants with enhanced voltage-sensitive fluorescence in mammalian and Caenorhabditis elegans neurons”. In: *Nature Communications* 5:4894. doi: 10.1038/ncomms5894.

N.C.F. helped conceive the project, designed and performed experiments, analyzed the data and wrote the manuscript with support from all authors.

[7] McIsaac, R. S. et al. (2014). “Directed evolution of a far-red fluorescent rhodopsin”. In: *Proceedings of the National Academy of Sciences of the United States of America* 111(36), pp. 13034-9. doi: 10.1073/pnas.1413987111.

N.C.F. performed research, contributed new reagents/analytic tools and analyzed data.

TABLE OF CONTENTS

Chapter 1

INTRODUCTION

Biological systems are unfathomably complex, and even with all the scientific advances of the past century, we are still only beginning to scratch the surface. At all scales, from the network of billions of cells in the brain to 60 proteins expressed from the same gene coming together to form a viral capsid, the more we learn, the more we realize that we don't know. The marriage of biology with engineering that has taken place in the last decades has provided a rapid increase in technological development to help address the myriad questions that abound. For my Ph.D., instead of attempting to answer a specific biological question, I adopted to develop technologies that would empower the research of others, from monitoring the activity of a single neuron and how it performs within a circuit to developing techniques to visualize or affect entire organs or organisms at once.

1.1 Microbial rhodopsins: flexible tools across disciplines

Rhodopsins are a very diverse family of proteins, found across all walks of life, but with a very singular purpose: detecting and responding to light. They are subdivided into two distinct groups, microbial and animal opsins[1]. Animal opsins are found in higher order eukaryotes and are primarily responsible for vision[2]. Microbial opsins, on the other hand, are found in prokaryotes, algae, and fungi, and perform basic survival functions related to the sensation of light, such as development and phototaxis. While animal opsins have been studied for their role in the visual pathway, it is microbial opsins that provide a wealth of novel applications for biology. Made famous by the advent of optogenetics[3], microbial rhodopsins in neuroscience are used for their ability to pump or channel protons or ions in and out of cells in response to light. These responses allow scientists to control neuronal activity of genetically defined populations with great temporal and spatial specificity. A variety of opsins have been discovered[4], or engineered[5], that respond to different wavelengths of light, at different speeds, and fluxing a variety of ions, in order to fulfill the various needs for activating or inhibiting neuronal activity. In Chapter 2.2, I discuss my

efforts in collaboration with the Arnold lab at Caltech, to engineer the *Gloeobacter violaceus* rhodopsin proton pump (GR) to respond to vastly different wavelengths from the wild-type, beyond the range of known, natural protein pumping rhodopsins[6]. This proof of principle of rhodopsin engineering set the stage for our continued work on opsin engineering for other applications.

Another application, not well studied until recent years, of microbial rhodopsins, and proton pumps specifically, is the ability to not only absorb and respond to light but emit it in return as fluorescence[7]. This ability to fluoresce, albeit very weakly, also happens in a pH or voltage dependent manner. This property of opsins to exhibit voltage-dependent fluorescence in response to light was first utilized by the Cohen group at Harvard[8] in studying the use of Archaerhodopsin-3 (Arch) as a voltage sensor in mammalian cells, similar to how it had first been utilized as an inhibitor of neuronal activity less than a decade earlier. Voltage or calcium dependent sensors were not a new concept for monitoring neuronal activity[9–11], but Arch provided greatly increased speed and dynamic range of fluorescence in comparison to existing tools. Arch never gained momentum as a neuroscience tool, though, in large part due to its incredibly weak fluorescence, a function of the highly inefficient quantum yield of rhodopsins naturally. In Chapter 2.3, I discuss my efforts, also in conjunction with the Arnold lab, to evolve Arch for brighter fluorescence in mammalian cells[12]. This was built upon the previous work with GR, using the mutations found in that paper as a starting point, and was also achieved by manipulating the amino acids in direct proximity with the light absorbing and emitting retinal chromophore. While this work resulted in a variant of Arch, Arch-7, that exhibited between 10-100-fold increased brightness in *E. coli*, at a maximal emission wavelength of 730nm, my interest was in the parent variant, Arch(DETC), which showed ~4.5-fold improved fluorescence over Arch in HEK293 cells.

The focus of Chapter 2.4 is my characterization of Arch(DETC), or Archer, for use as a voltage-sensitive fluorescence protein for neuroscience applications. As mentioned above, neuroscience has already made great use of microbial rhodopsins, by utilizing their ability to control neuronal activity through the application of light. I now wanted to be able to also record their activity using the same light sensitivity and utilizing the speed which set them apart from other voltage or calcium indicators. The GCaMP family of calcium sensors[9]

is the gold standard for measuring neuronal activity, but utilizes a secondary measure, calcium, instead of being able to report on changes in voltage directly. For this reason, a voltage indicator like Arch would be a cleaner measure of activity. Thankfully, we had already found a variant of Arch, Archer, which exhibited greatly enhanced fluorescence, bypassing Arch's main limitation. In characterizing Arch's voltage sensitivity in cultured neurons[13], we discovered that Arch was able to follow quick changes in voltage, on the order of the fastest neurons in the brain, and presented the largest change in fluorescence in response to voltage of any genetically encoded voltage indicator to date. As a proof of principle for its feasibility to be used *in vivo*, we used it in awake, behaving worms, where we accurately detected changes in voltage in response to known stimuli.

1.2 Tissue clearing flexibility across diverse tissue types

The study of biological specimens at a microscopic scale has always been dependent on the availability of optical access. This, along with the ease of doing genetic manipulations, is one of the chief regions why model organisms like the worm *Caenorhabditis elegans* and zebrafish *Danio rerio* have gained such tractability. While studying larger organisms, like mice, chickens, and non-human primates, allows scientists to approach more complex biological questions, it comes hand in hand with the inability to visualize the myriad processes going on below the surface. For this reason, traditional histological practices of sectioning tissue into two-dimensions to visualize under a microscope have taken prevalence across biological disciplines. The downside of this practice is the loss of high-resolution, three-dimensional representations of anatomical and functional characteristics. With the advent of tissue clearing, though, we can render large, opaque sections of tissue transparent, allowing for unperturbed study of cells, their interaction with each other and their native environment. This concept is not a recent one, with the use of organic-solvents to clear tissue dating back over a century. Those traditional methods were not without their downsides, though, chief among which was damage to the specimens under observation. In recent years, a method for visualizing intact sections of tissue, organs, or entire organisms was developed, coined CLARITY[14]. CLARITY sought to remove the chief limitation to optical access throughout a tissue, the light-scattering lipids, without perturbing the rest of the molecular

content, namely proteins and nucleic acids. In this way, CLARITY brought tissue clearing to the main stream, providing a method theoretically compatible with the diverse needs of the biological community.

Biological specimens come in a variety of sizes, densities and macromolecular contents. Additionally, experimental concerns usually include the presence of endogenous fluorescence, type of labeling required, antibody or nucleic acid, epitope retention, and relative positions of imaging targets to each other for a fully three-dimensional study. Passive CLARITY, or PACT[15], as a methodology, is able to address all of these concerns: PACT is able to retain endogenous fluorescence, allows for immunohistochemistry and *in situ* hybridization, and avoids anisotropic shrinking or swelling of tissue. To achieve these results, though, a variety of experimental parameters need to be characterized, and their effects upon experimental outcome explored. In Chapter 3.2, I detail my work on characterizing the various conditions under which PACT can be performed for varied needs[16].

One experimental need that benefits from the use of tissue clearing is the study of the neural crest and its derivatives in developing embryos. The neural crest is a multipotent stem cell population with the capacity to self-renew and to differentiate into numerous cell types, the dysregulation of which leads to a multitude of neurocristopathies[17] with extremely detrimental phenotypes. Neural crest cells arise within the forming central nervous system but then undergo an epithelial to mesenchymal transition to become migratory cells that undertake some of the longest migrations of any embryonic cell type. Upon reaching their final destinations, they differentiate into numerous cell types, ranging from craniofacial cartilage and bone to pigment cells of the skin, peripheral neurons and glia, and many other cell types[18]. Much of what we know about the cell types formed by and migratory routes followed by neural crest cells dates back to the pioneering studies of LeDouarin and colleagues[19] in the 1970s and 80s. Using interspecific grafts of donor quail cells into host chick embryos, they created “chimera” in which neural folds of quail origin were grafted in place of chick neural folds, allowing for their derivatives and contributions to be distinguished in a species-specific manner.

Despite their elegance and utility, these experiments are not without limitations. Because quail/chick grafts were conducted with two different species of birds, one cannot

rule out the possibility of artifacts caused by species-specific differences. As a case in point, quail cells are more invasive than chick cells[20]. In addition, as embryos grow, it becomes increasingly difficult to follow a small number of quail cells in a sea of chick tissue, making it possible that some neural crest contributions to various organs have gone unnoticed. This is particularly problematic given that amniote embryos are opaque and thus require serial sectioning to identify grafted cells at single-cell resolution. This is not only tedious, but sections can be lost, and neural crest derivatives underestimated. For these reasons, it is critical to revisit these classical experiments, not only to verify but also extend the results with modern technology. This is where the advantages of tissue clearing appear. In Chapter 3.3, I detail how I adapted PACT to clearing chicken embryos and tested labeling methodologies for antibodies and nucleic acids to be able to fully characterize the neural crest derivative populations we were interested in studying. By utilizing intraspecific grafts from GFP-labeled donor chick neural folds into wild-type hosts and PACT to clear the entire embryos, we were able to analyze the sites to which GFP-labeled neural crest cells migrate in whole mount. By doing so, we were able to verify several previously characterized populations arising from the cardiac neural crest, as well as discover the possibility that populations previously attributed to other areas of the neural crest were instead cardiac crest derived.

1.3 Engineered AAVs for systemic delivery in gene therapy

In recent years, we have witnessed the development and clinical use of gene therapies at an accelerated pace. The ability to change or introduce new genes greatly increases the therapeutic options for a variety of diseases. Amongst gene therapy vehicles, adeno-associated viruses (AAVs) are preferred due to their low immunogenicity, stable expression, and strong clinical safety record. In the clinic, AAVs have shown incredible promise, being the first vector approved in 2012 for use in humans to treat lipoprotein lipase deficiency[21], with other trials just approved in 2017 (e.g. vision, hemophilia)[22,23] and many more ongoing (Parkinson's, Alzheimer's)[24]. In addition, systemic AAV administration through the blood allows for gene delivery to widespread regions of the body in a non-

invasive manner. However, naturally occurring AAVs have limited and highly overlapping tropism[25], motivating us to work towards enhancing AAV functionality and versatility.

Most gene therapies currently in clinical trials utilize naturally occurring AAV serotypes, which have evolved to broadly infect cells without much specificity. While this is a desirable characteristic for the survival of the virus, it is undesirable for its use to target gene therapies to specific cells. Two problems arise: 1) off-target effects and 2) the necessity for a larger viral load to achieve sufficient therapeutic levels. Traditionally, in gene therapy, these problems are addressed by directly injecting virus into the area of interest. This approach greatly limits the scope for therapeutic applications as direct injections are often impractical (i.e. the brain), and other times, inadequate at applying the therapy to a wide enough area. Systemic administration via the blood is an option in cases where direct administration is not practical and widespread areas need to be reached but runs up against the problem of the lack of target specificity. While naturally occurring AAVs have differing tropisms, they mostly target similar tissues at high levels, like the liver[25–27]. This results in a substantial number of viruses transducing the liver, while very few transduce another tissue of interest, for instance the central of peripheral nervous systems. A notable target is the brain, which naturally occurring AAVs cross into extremely inefficiently. In order to achieve a high enough level of expression in the target of interest, an abnormally high viral load can become necessary, which can induce a T-cell immune response producing systemic inflammation and, in severe cases, proving lethal[28].

In order to address the above issues and develop AAVs with high efficiency after systemic administration, a screening method, CREATE[29], was developed by Deverman and colleagues which allowed for the screening of large libraries of viral variants *in vivo*. This approach differs from previous efforts utilizing *in vitro* platforms[30–32] or multiple rounds of selection *in vivo* without strong selective pressure[33]. Viruses found from *in vitro* screens often had difficulty translating to *in vivo* applications due to not having been selected in the complex environment the virus needed to act upon, while those developed from *in vivo* screens lacked the ability to distinguish between viruses just present in a tissue from those correctly unpackaging, traveling to the nucleus, and stably expressing their payload. These factors often lead to the necessity for many rounds of selection and evolution to narrow

libraries down to interesting variants[30–33]. CREATE, on the other hand, is built upon performing Cre-dependent selections in Cre-transgenic mouse lines, addressing both previous concerns. Utilizing this methodology, Deverman, Chan, and colleagues[29,34] selected for vectors that, when delivered systemically, could cross anatomical barriers (such as the blood-brain) and efficiently transduce cells, with a notable finding being the recently published PHP.eB variant, which most efficiently targets the murine brain.

In Chapter 4.2, I detail an evolution of the CREATE screening method. We employ parallel *in vivo* selections in multiple transgenic lines with positive and negative selective pressure, screening large libraries of engineered viral variants to select for the ones that, after systemic administration, very specifically enter cells and organs of interest and not others. By engineering viruses to more efficiently and specifically target certain cell types and regions, we can ensure effective therapeutic expression only to the areas where it is needed, while lowering the total systemic viral load introduced to the body and therefore minimizing side-effects. In Chapters 4.3 and 4.4, I discuss our results in engineering two such viruses, AAV9.RWT4 and AAV9.ReB10, which display increased specificity toward lung and brain respectively, and detargeting from other organs. AAV9.ReB10 also shows bias toward a specific cell-type within the brain, neurons, and significantly reduced levels in others. In both cases, these two engineered variants represent targeted evolution away from their parent virus, AAV9 and PHP.eB respectively, toward areas of therapeutic significance, providing candidates for non-human primate testing for eventual clinical applications or as scaffolds for further evolution.

Chapter 2

ENGINEERING MICROBIAL RHODOPSIN SPECTRAL PROPERTIES AND VOLTAGE SENSITIVITY

[5] Engqvist, M. K. et al. (2015). "Directed evolution of Gloeobacter violaceus rhodopsin spectral properties". In: *Journal of Molecular Biology* 427(1), pp. 205-20. doi: 10.1016/j.jmb.2014.06.015.
[7] McIsaac, R. S. et al. (2014). "Directed evolution of a far-red fluorescent rhodopsin". In: *Proceedings of the National Academy of Sciences of the United States of America* 111(36), pp. 13034-9. doi: 10.1073/pnas.1413987111.
[6] Flytzanis, N. C.*, Bedbrook, C. N.* et al. (2014). "Archaerhodopsin variants with enhanced voltage-sensitive fluorescence in mammalian and Caenorhabditis elegans neurons". In: *Nature Communications* 5:4894. doi: 10.1038/ncomms5894.

2.1 Summary

Proton-pumping rhodopsins (PPRs) are photoactive retinal-binding proteins that transport ions across biological membranes in response to light. These proteins are interesting for light-harvesting applications in bioenergy production, in optogenetics applications in neuroscience, and as fluorescent sensors of membrane potential. Little is known, however, about how the protein sequence determines the considerable variation in spectral properties of PPRs from different biological niches or how to engineer these properties in a given PPR. Here we report a comprehensive study of amino acid substitutions in the retinal-binding pocket of Gloeobacter violaceus rhodopsin (GR) that tune its spectral properties. Directed evolution generated 70 GR variants with absorption maxima shifted by up to ± 80 nm, extending the protein's light absorption significantly beyond the range of known natural PPRs. We discovered a subset of red-shifted GRs that exhibit high levels of fluorescence relative to the WT protein.

Another member of this protein family, Archaerhodopsin-3 (Arch) of halobacterium Halorubrum sodomense, was shown to function as a fluorescent indicator of membrane potential when expressed in mammalian neurons. Arch fluorescence, however, is very dim and is not optimal for applications in live-cell imaging. We used directed evolution to identify mutations that dramatically improve the absolute brightness of Arch, as confirmed biochemically and with live cell imaging. In some fluorescent Arch variants, the pKa of the protonated Schiff-base linkage to retinal is near neutral pH, a useful feature

for voltage-sensing applications. These bright Arch variants enable labeling of biological membranes in the far-red/infrared and exhibit the furthest red-shifted fluorescence emission thus far reported for a fluorescent protein (maximal excitation/emission at ~620 nm/730 nm).

Probing the neural circuit dynamics underlying behavior would benefit greatly from improved genetically encoded voltage indicators. Arch, usually used as an optogenetic tool for neuronal inhibition, has also been shown to emit voltage-sensitive fluorescence. Here we report two Arch variants with enhanced radiance (Archers) that in response to 655 nm light have 3–5 times increased fluorescence and 55–99 times reduced photocurrents compared with Arch WT. The most fluorescent variant, Archer1, has 25–40% fluorescence change in response to action potentials while using 9 times lower light intensity compared with other Arch-based voltage sensors. Archer1 is capable of wavelength-specific functionality as a voltage sensor under red light and as an inhibitory actuator under green light. As a proof-of-concept for the application of Arch-based sensors *in vivo*, we show fluorescence voltage sensing in behaving *Caenorhabditis elegans*. Archer1's characteristics contribute to the goal of all-optical detection and modulation of activity in neuronal networks *in vivo*.

2.2 Directed evolution of Gloeobacter violaceus rhodopsin spectral properties

[5] Engqvist, M. K. et al. (2015). "Directed evolution of Gloeobacter violaceus rhodopsin spectral properties". In: *Journal of Molecular Biology* 427(1), pp. 205-20. doi: 10.1016/j.jmb.2014.06.015.

2.2.1 Targeted mutagenesis for spectral tuning of GR

The retinal-binding pocket forms all the retinal chromophore contacts; we expected that these residues would provide a rich source of spectral tuning mutations. To identify amino acid substitutions in the GR retinal binding that led to shifts in λmax, we developed a moderate-throughput expression and purification assay (Fig. 1). Briefly, following GR expression in *E. coli*, we extracted protein from the cell membrane using lysozyme treatment in the presence of the detergent n-dodecyl β-D-maltoside (DDM) and subsequently purified it in 96-well filter plates pre-loaded with Ni-NTA resin (Fig. 1). The absorption properties of engineered variants were determined in 96-well format using a

standard plate reader (Fig. 1, see Materials and Methods for details). The limits of spectral shifting were further explored by recombination of single mutations identified from saturation mutagenesis libraries and additional mutagenesis and screening of the most red- and blue-shifted recombined variants.

To identify putative binding pocket residues in GR, we generated a homology model (see Materials and Methods) based on the crystal structure of its xanthorhodopsin (XR) homolog (44% protein sequence identity). In the GR model, 20 residues (D121, W122, T125, V126, L129, M158, I159, G162, E166, G178, S181, T182, F185, W222, Y225, P226, D253, A256, and K257) are within 5 Å of the retinal chromophore (Fig. 2). D121, W222, Y225, P226, D253, and K257 (which forms the Schiff base) are completely conserved between GR and the two best-studied PPRs, PR and BR (Table 1 and Fig. S1). While PPRs show extensive sequence diversity (with overall sequence identities as low as ~ 20%), the binding pocket residues show a marked degree of conservation (Table 1 and Fig. S1). Site-saturation mutagenesis was performed at each of the binding pocket positions except K257, which forms the critical retinal linkage. Screening 88 clones for each saturation mutagenesis library (94% library coverage) identified a total of 52 unique blue- and red-shifted variants (Figs. 2 and 3 and Table S1). Mutagenesis at 15 of the 19 binding pocket residues yielded one or more spectral tuning mutations (Figs. 2 and 3). Thirteen of these fifteen positions gave rise to variants with exclusively blue or red shifts, but not both (the exceptions being D121 and A256, which gave both) (Figs. 2 and 3). Eighty percent of red-shifted variants contained mutations within 4 Å of the Schiff base linkage, whereas blue-shifting mutations were distributed along the retinal chromophore (Fig. S2). Blue-shifting mutations far from the Schiff base (N10 Å) tended to increase local hydrophobicity, while blue-shifting mutations closer to the Schiff base tended to decrease local hydrophobicity (Fig. 4). Most mutations that cause a red shift were identified at D121 and T125, which had 12 and 6 tuning mutations, respectively. Three residues, G162, E166, and A256, each had four blue-shifting mutations. Residues G178, W222, and Y225 had a single tuning mutation apiece: G178Q (blue shift), W222M (red shift), and Y225A (red shift). While most binding pocket residues had two or fewer mutations that only modestly

affected λmax, a handful of hot spots (D121 and G162) had many tuning mutations that led to large shifts in λmax (Fig. 3).

2.2.2 Recombination for further mutagenesis

To test whether the tuning mutations could be combined to generate even larger spectral shifts, we generated two recombination libraries, one for blue-shifting mutations (the "blue" library) and one for red-shifting mutations (the "red" library). A fractionated plasmid amplification (Fig. S5a) approach allowed us to rapidly generate all possible combinations of targeted mutations with high confidence. Mutations that resulted in small spectral shifts and/or eliminated proton pumping were not included in these libraries. Recombining mutations V126A, M158L, G162C, G162L, G162S, G162V, E166P, E166W, S181G, A256C, A256D, A256G, and A256S with the WT codon for each position gave a blue library having 600 possible variants (Fig. S5b). We screened 1760 clones (95% coverage). Five mutants were found to be more blue-shifted than GRb1 (G162L). The most blue-shifted variant had three mutations (G162L, E166W, and A256S) and exhibited a further shift of −22 nm with respect to GRb1. This variant is called GRb2 (Figs. 3 and 5 and Table S2).

The red library recombined T125C, T125D, T125G, T125N, T125V, L129K, L129W, W222M, P226I, P226V, and A256M with the WT codon for each position (216 possible variants) (Fig. S5b). Screening 880 clones (98% coverage) yielded three variants more red-shifted than GRr1 (T125N) (Fig. 3 and Table S2). The T125C/A256M (GRr2) and T125V/A256M variants were the most red-shifted: each had an ~ 16-nm additional shift compared to GRr1 (Figs. 3 and 5 and Table S2). None of the eight recombined further blue- or red-shifted variants showed measurable proton-pumping activity (Fig. 3).

We wished to explore whether even larger shifts in GR λmax were possible. We therefore performed site-saturation mutagenesis on GRb2 and GRr2 at all sites within the retinal-binding pocket that were not already mutated (excluding K257). For the GRb2 libraries, 1408 (16 × 88) clones were screened for 94% coverage, and for the GRr2 libraries 1496 (17 × 88) clones were screened for 94% coverage. Further shifted variants, with respect to their GRb2 and GRr2 parents, were sequenced. This led to the identification of

ten tuning mutations, eight of which had not been identified in the first round of site-saturation mutagenesis (Fig. 3 and Table S3). The libraries generated with GRr2 yielded two unique mutations that further red-shifted the protein (Fig. 3). The most red-shifted variant (GRr3; λmax = 619 nm), with a + 81-nm shift relative to WT GR, contained the D121E mutation in addition to the T125C and A256M mutations in GRr2 (Figs. 3 and 5 and Table S3). The spectral shift of GRr3 was greater than predicted by simply adding effects from single tuning mutations (Fig. S6). The three most blue-shifted variants, with −79 to −80 nm shifts, had the W122L, W122M, or D121E mutations in addition to the parental G162L, E166W, and A256S mutations. The W122L/G162L/E166W/A256S variant is referred to as GRb3 (Figs. 3 and 5 and Table S3). Its λmax is 458 nm. Overall, screening 7216 clones (1672 in the first round of site-saturation mutagenesis, 2640 for the recombination libraries, and 2904 in the second round of site-saturation mutagenesis) for shifted absorption maxima resulted in 70 unique shifted variants (Fig. 3). GRb3 and GRr3 differ by only seven mutations, yet their λmax are 161 nm apart.

2.2.3 GR mutants exhibit increased fluorescence

We tested the fluorescence properties of all 70 spectrally tuned GRs using a 96-well assay developed for this purpose. The full excitation spectrum was computed for each GR variant at multiple emission wavelengths (625–775 nm in 25-nm increments). The area under the curve (AUC) of the excitation spectra (at an emission wavelength of 725 nm) for each variant was used to score its overall fluorescence. AUC values were rank-ordered and color-coded according to their absorbance shift, revealing six outlier red-shifted variants (Fig. 8a). Measuring the full excitation-emission spectra of these variants confirmed increased fluorescence over the WT protein, which exhibited no measurable fluorescence under our assay conditions (Fig. 8b). The variant displaying the greatest *in vivo* fluorescence was D121E/T125C/A256M (Fig. 8b), which also had the highest quantum yield in vitro (1.2×10^{-2}) of the six bright mutants (Table 2). Increasing the external pH from 6 to 11 attenuated fluorescence ~ 2-fold (Fig. 8c).

2.2.4 Main figures and tables

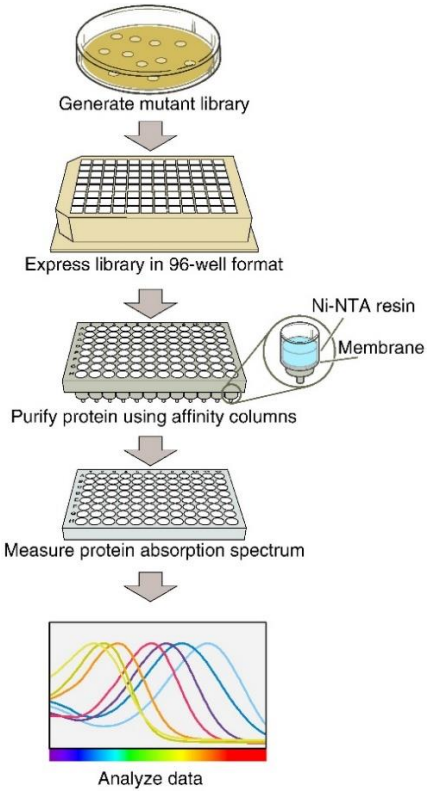

Fig. 1. Schematic of screen for GR spectral tuning. Briefly, mutant GR libraries were transformed into *E. coli* followed by growth on selective solid media.
Single *E. coli* colonies were picked with toothpicks and grown in 96-well plates. Following induction, His-tagged mutant GRs were purified using Ni-NTA resin. Absorbance spectra of mutant GRs were measured with a standard plate reader, from which the absorption maxima were determined.

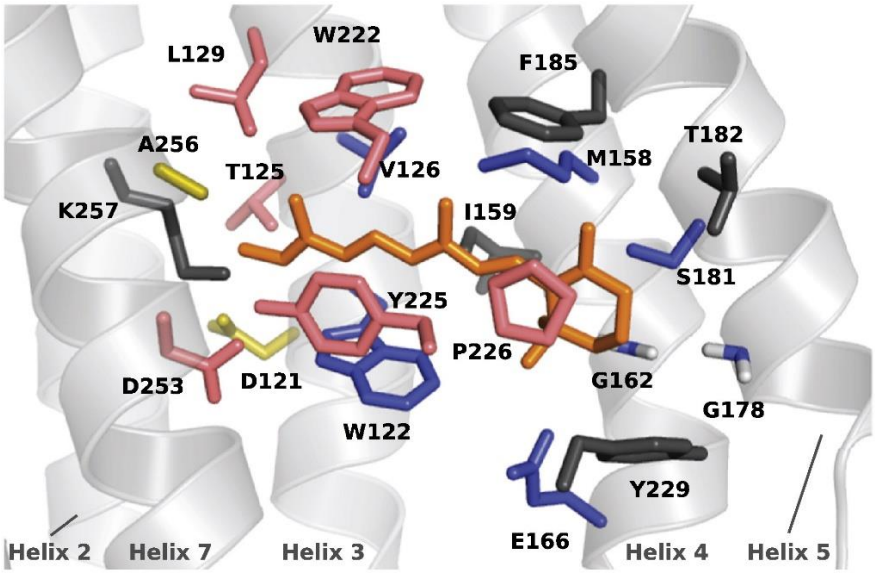

Fig. 2. Retinal-binding pocket in GR homology model. Side chains of amino acids within 5 Å of retinal are shown. Glycines are displayed with hydrogen atoms visible. Residues for which only blue shifts were detected are colored blue (W122, V126, M158, G162, E166, G178, S181), residues with only red shifts are colored red (T125, L129, W222, Y225, P226, D253), and residues that yield both blue and red shifts are colored yellow (D121, A256). Black indicates positions for which no shifts were identified (I159, T182, F185, Y229) and the conserved Schiff base residue (K257), which was not targeted for mutagenesis. The retinal molecule is shown in orange. Helix six is omitted for clarity.

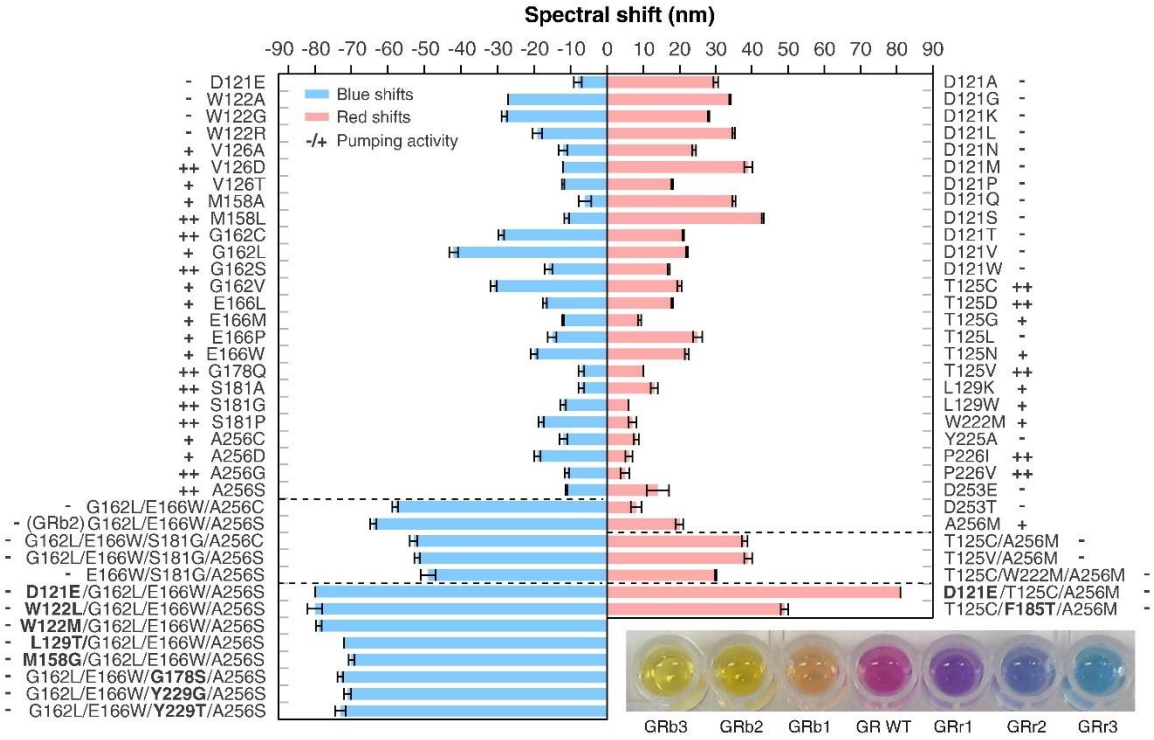

Fig. 3. Spectrally shifted variants identified by site-saturation mutagenesis and recombination. The absorption maxima (λ_{max}) represent averages, with standard error, of three biological replicas that were grown and extracted separately. Shifts are reported with respect to λ_{max} of WT GR (538 nm). H^+-pumping activities were determined using a dye-efflux assay (see Materials and Methods): (−) no detectable activity, (+) activity that is less than 50% of WT, and (++) activity that is more than 50% of WT. Broken lines separate mutants resulting from different rounds of directed evolution. From the top, these are (1) site-saturation mutagenesis of WT GR, (2) recombination libraries, and (3) second round of site-saturation mutagenesis, performed on G162L/E166W/A256S and T125C/A256M. New mutations are shown in boldface and parent mutations are shown in plain text. (insert) Purified variants of GR, including the WT protein (GR WT), three GR variants with red-shifted λ_{max} (GRr1, GRr2, and GRr3), and three GR variants with blue-shifted λ_{max} (GRb1, GRb2, and GRb3). GRr1 = T125N, GRr2 = T125C/A256M, GRr3 = D121E/T125C/A256M, GRb1 = G162L, GRb2 = G162L/E166W/A256S, and GRb3 = W122L/G162L/E166W/A256S.

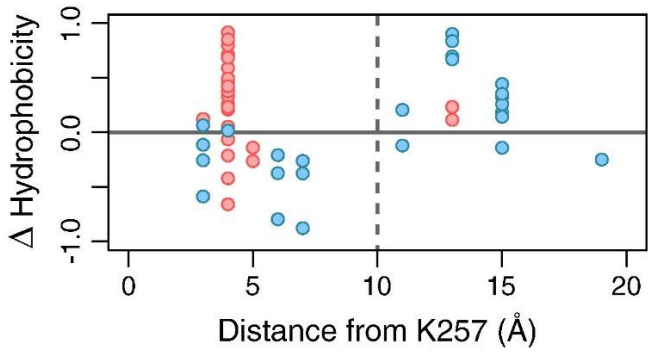

Fig. 4. Relationship between hydrophobicity and residue distance from the Schiff base (K257) for blue- and red-shifting mutations. Amino acid substitutions that are more hydrophobic than the parental residues result in ΔHydrophobicity > 0, while those that are less hydrophobic than the parental residues have ΔHydrophobicity < 0. For blue-tuning mutations, the Pearson correlation between ΔHydrophobicity and distance from K257 is 0.55 (p = 0.0045), while for red tuning mutations, there is no correlation. Amino acid hydrophobicity scores were obtained from Black and Mould[35].

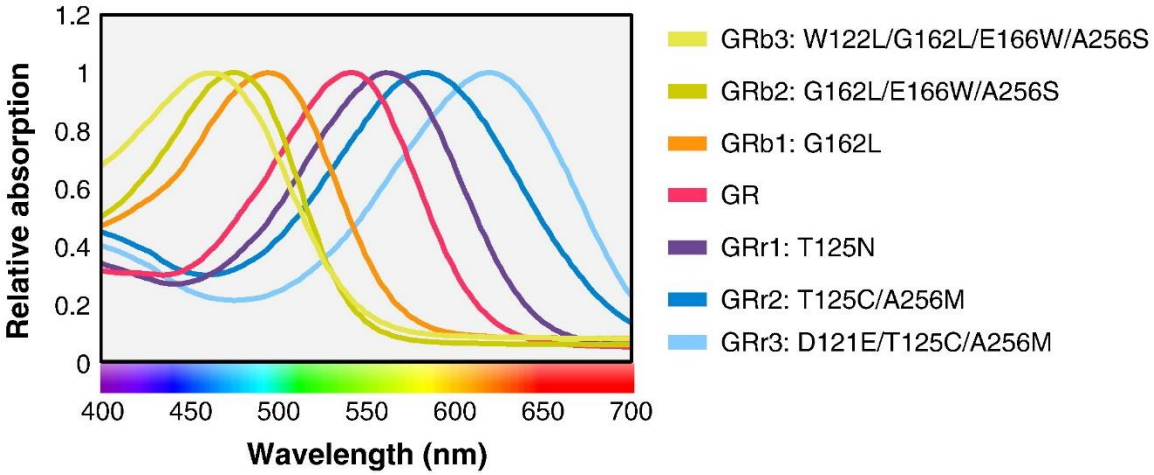

Fig. 5. Normalized absorption spectra of WT GR and key variants from each round of directed evolution. Absorption spectra are colored to match the colors of the rhodopsin pigments.

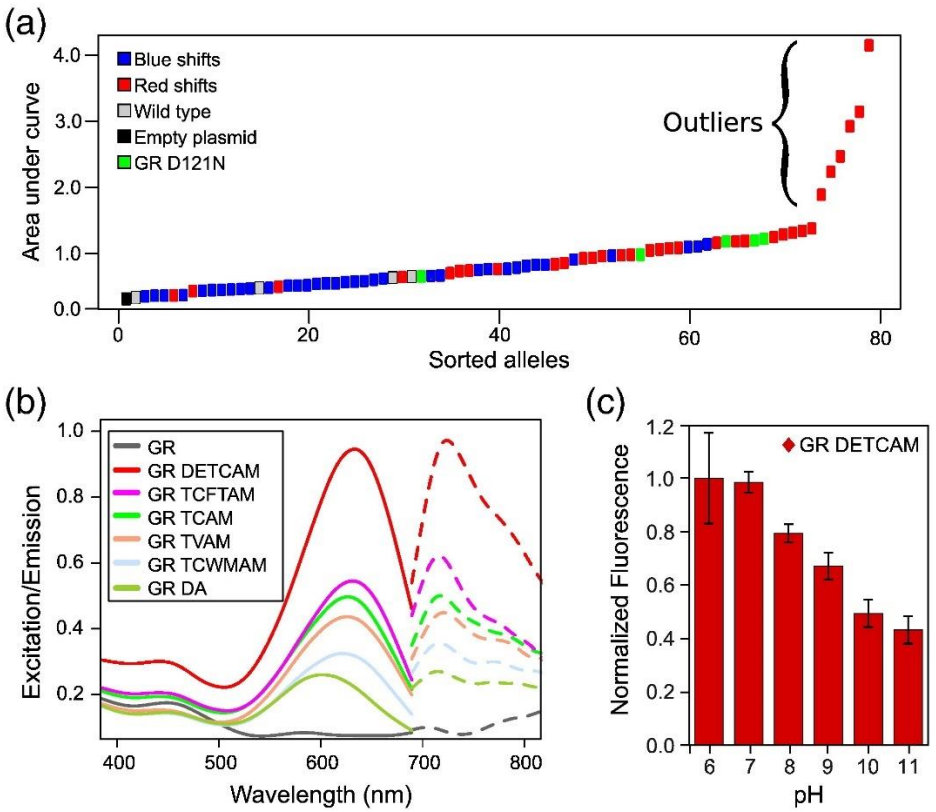

Fig. 8. Fluorescent properties of GR variants measured in live *E. coli*. (a) The AUC was computed from the excitation spectra of 70 unique GR, ranked-ordered, and color-coded according to spectral shift [technical replicates of GR(D121N), a red-shifted variant, are shown in green]. (b) Spline-fit excitation/emission spectra (performed in biological quadruplicate) of six outliers from (a) and WT GR. The mutations are written in shorthand without the residue numbers: GR(DETCAM) = GR(D121E/T125C/A256M), GR(TCFTAM) = GR(T125C/F185T/A256M), GR(TCAM) = GR(T125C/A256M), GR(TVAM) = GR(T125V/A256M), GR(TCWMAM) = GR(T125C/W222M/A256M), GR(DA) = GR(D121A). (c) Fluorescence of GR(D121E/T125C/A256M) normalized for total expression measured from pH 6 to pH 11.

GR Position[a]	121	122	125	126	129	158	159	162	166	178	181	182	185	222	225	226	229	253	256	257
Natural variation[b]	D	W	T	V	L	M	I L V	G	E D	G F W	S A	T M S	F	W	Y	P	Y F	D	A	K
Mutations[c]	A, P E, Q G, S K, T L, V N, W M	A G R	C D G L N V	A D T	K W	A L	–	C L S V	L M P W	Q	A G P	–	–	M	A	I V	–	E T	C D G M S	–

BR Position[a]	85	86	89	90	93	118	119	122	126	138	141	142	145	182	185	186	189	212	215	216
Natural variation[b]	D	W	T	T	L	M	I V	G	A T	W	S	D T	F L M	W	Y	P	W	D	A S	K
Mutations[c]	A[52] E[53] N[53] V[54] S[54] T[55]	F[56]	A[57] D[58] N[59] V[60]	A[61] V[61]	A[62] T[62] V[62]	A[26]	–	C[63]	–	C[60]	A[26] C[57]	V[57]	A[63]	F[56]	F[64]	A[65] L[66] V[60]	F[67]	E[68]	N[26] T[26]	–

PR Position[a]	97	98	101	102	105	133	134	137	141	151	154	155	158	197	200	201	204	227	230	231
Natural variation[b]	D	W I	T P Q	V C	L Q A V Y E	V A I L	M	A F G V	G	A C G	I L V	A G	A G	W	Y	P	Y	D	N	K
Mutations[c]	N[69]	G[25]	A[25]	A[25]	K[70]	–	–	–	–	–	–	–	–	–	H[25] N[25]	–	–	E[71]	–	–

Table 1. Comparison of natural variation and introduced mutations in retinal-binding pocket of GR and homologs

[a]Homologous residues in the retinal-binding pocket were identified through structure-guided alignment of protein sequences.

[b]Natural variation represents variants retrieved from BLAST searches of the NCBI database with GR, BR, and PR.

[c]Mutations conferring spectral tuning in each of the three proteins and close homologs. The coloring of the mutations indicates whether they are blue- or red-shifted. For GR, the 52 single mutations were discovered in the first round of site-saturation mutagenesis. For BR and PR, mutations were identified through a literature search. (See references[36–50] as indicated in the table). GR mutations that correspond to mutations previously described in BR or PR are underlined.

Mutant	Quantum yield
D121A	5×10^{-3}
T125C/W222M/A256M	8×10^{-3}
T125C/A256M	9×10^{-3}
T125V/A256M	9×10^{-3}
T125C/F185T/A256M	9×10^{-3}
D121E/T125C/A256M	1.2×10^{-2}

Table 2. Quantum yields of bright GR variants identified in this study

2.2.5 Supplementary figures and tables

GR	D121	W122	T125	V126	L129	M158	I159	G162	E166	G178	S181	T182	F185	W222	Y225	P226	Y229	D253	A256	K257
BR	D85	W86	T89	T90	L93	M118	I119	G122	A126	W138	S141	T142	M145	W182	Y185	P186	W189	D212	A215	K216
gPR	D97	W98	T101	V102	L105	V133	M134	F137	G141	A151	I154	G155	A158	W197	Y200	P201	Y204	D227	N230	K231
Arch	D95	W96	T99	T100	L103	M128	I129	G132	A136	W148	S151	T152	M155	W192	Y195	P196	W199	D222	A225	K226

Figure S1: Summary of a structure-based alignment of retinal binding pocket residues for PR, Arch, BR, and GR.

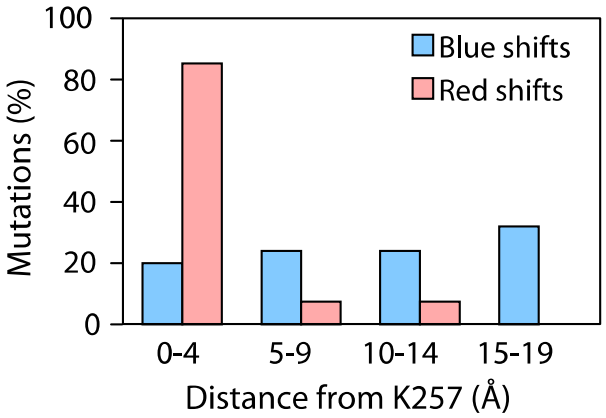

Figure S2: Proportion of blue- and red-shifting mutations found within a given distance from K257. Measurements were done in PyMOL on a GR homology model based on the XR structure (see Methods).

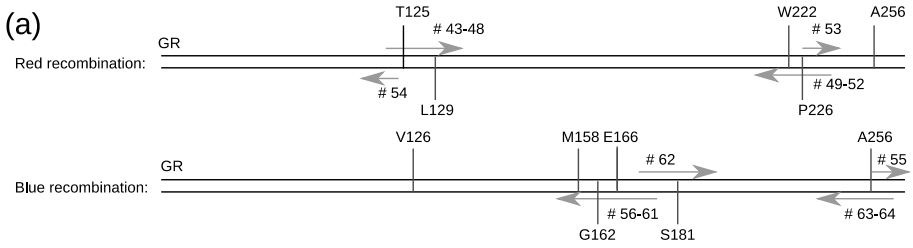

(b)

Blue shift recombination						Red shift recombination				
V 126	M 158	G 162	E 166	S 181	A 256	T 125	L 129	W 222	P 226	A 256
A	L	C L S V	P W	G	C D G S	C D G N V	K W	M	I V	M
2	2	5	3	2	5	6	3	2	3	2
600						216				

Figure S5: Generation of recombination libraries. (a) Schematic of primer design for fractionated plasmid amplification to generate GR recombination libraries. Where several numbers are given a mix of primers was used to ensure equal distribution of amino acid codons. (b) Summary of residues in blue-shifted and red-shifted recombination libraries, which have 600 and 216 members, respectively.

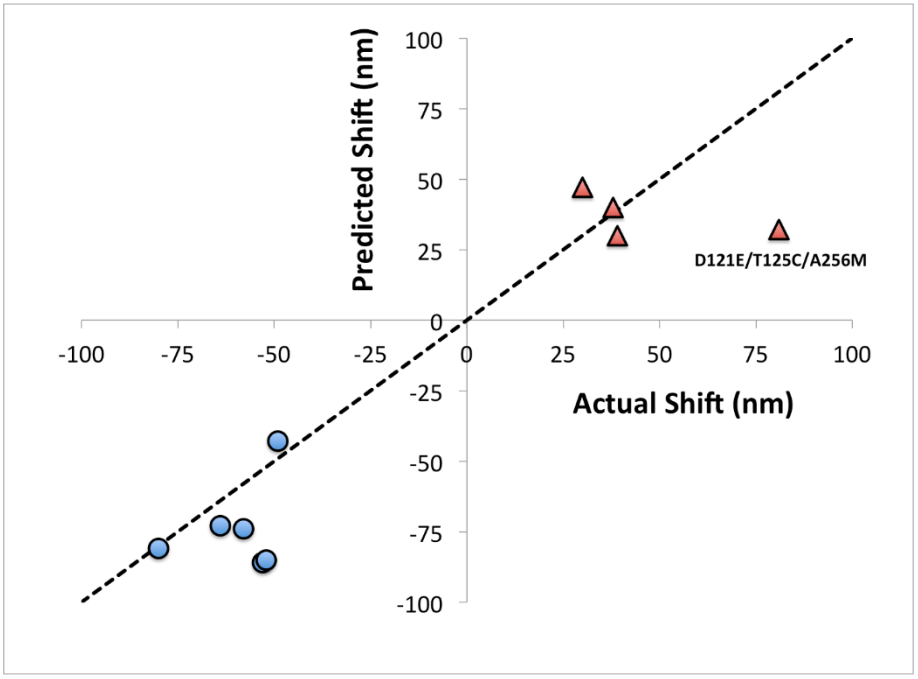

Figure S6: Plot of spectral shift predicted from simply adding effects of single tuning mutations versus the actual spectral shift of selected GR mutants. Data for generating this figure can be obtained from Tables S1-S3.

Variant	λ_{max} (nm)	Shift (nm)	H^+ pumping	Variant	λ_{max} (nm)	Shift (nm)	H^+ pumping
WT (GR)	538 ± 0	0	++				
Blue shifts				**Red shifts**			
D121E	530 ± 1	-8	-	D121A	568 ± 1	30	-
W122A	511 ± 0	-27	-	D121G	572 ± 0	34	-
W122G	510 ± 1	-28	-	D121K	566 ± 0	28	-
W122R	519 ± 1	-19	-	D121L	573 ± 0	35	-
V126A*	526 ± 1	-12	+	D121N	562 ± 1	24	-
V126D	526 ± 0	-12	++	D121M	577 ± 1	39	-
V126T	526 ± 0	-12	+	D121P	556 ± 0	18	-
M158A	532 ± 2	-6	+	D121Q	573 ± 0	35	-
M158L*	527 ± 1	-11	++	D121S	581 ± 0	43	-
G162C*	509 ± 1	-29	++	D121T	559 ± 0	21	-
G162L* (GRb1)	496 ± 1	-42	+	D121V	560 ± 0	22	-
G162S*	522 ± 1	-16	++	D121W	555 ± 0	17	-
G162V*	507 ± 1	-31	+	T125C*	558 ± 1	20	++
E166L	521 ± 1	-17	+	T125D*	556 ± 0	18	++
E166M	526 ± 0	-12	+	T125G*	547 ± 0	9	+
E166P*	523 ± 1	-15	+	T125L	563 ± 1	25	-
E166W*	518 ± 1	-20	+	T125N* (GRr1)	560 ± 1	22	+
G178Q	531 ± 1	-7	++	T125V*	548 ± 0	10	++
S181A	531 ± 1	-7	++	L129K*	551 ± 1	13	+
S181G*	526 ± 1	-12	++	L129W*	544 ± 0	6	+
S181P	520 ± 1	-18	++	W222M*	545 ± 1	7	+
A256C*	526 ± 1	-12	+	Y225A	546 ± 1	8	-
A256D*	519 ± 1	-19	+	P226I*	544 ± 1	6	++
A256G*	527 ± 1	-11	++	P226V*	543 ± 1	5	++
A256S*	527 ± 0	-11	++	D253E	552 ± 3	14	-
				D253T	546 ± 2	8	-
				A256M*	558 ± 1	20	+

Table S1. Spectrally-shifted variants identified in first round of site-saturation mutagenesis. The absorption maxima (λ_{max}) represent averages, with standard error, of three biological replicas that were grown and extracted separately. Shifts are reported with respect to wild-type λ_{max}. H^+-pumping activities were determined using a dye-efflux assay (see Methods), with (-) no detectable activity, (+) activity that is less than 50% of WT, and (++) activity

that is more than 50% of WT. Variants that were included in the blue- and red-shifted recombination libraries are indicated with a *.

Genotype	λ_{max} (nm)	Shift (nm)	H^+ pumping
Blue recombination library			
G162L/E166W/A256C	480 ± 1	-58	-
G162L/E166W/A256S (GRb2)	474 ± 1	-64	-
G162L/E166W/S181G/A256C	485 ± 1	-53	-
G162L/E166W/S181G/A256S	486 ± 1	-52	-
E166W/S181G/A256S	489 ± 2	-49	-
Red recombination library			
T125C/A256M (GRr2)	576 ± 1	38	-
T125V/A256M	577 ± 1	39	-
T125C/W222M/A256M	568 ± 0	30	-

Table S2. Spectrally-shifted variants identified from recombination libraries. The absorption maxima (λ_{max}) represent averages, with standard error, of three biological replicas that were grown and extracted separately. Shifts are reported with respect to wild-type λ_{max}. H+-pumping activities were determined using a dye-efflux assay (see Methods), with (-) no detectable activity, (+) activity that is less than 50% of WT, and (++) activity that is more than 50% of WT. Variants that were included in the blue- and red-shifted recombination libraries are indicated with a *.

Variant	λ_{max} (nm)	Shift (nm)	H^+ pumping
Blue site-saturation mutagenesis			
D121E/G162L/E166W/A256S	458 ± 0	-80	-
W122L/G162L/E166W/A256S (GRb3)	458 ± 2	-80	-
W122M/G162L/E166W/A256S	459 ± 1	-79	-
L129T/G162L/E166W/A256S	466 ± 0	-72	-
M158G/G162L/E166W/A256S	468 ± 1	-70	-
G162L/E166W/**G178S**/A256S	465 ± 1	-73	-
G162L/E166W/**Y229G**/A256S	467 ± 1	-71	-
G162L/E166W/**Y229T**/A256S	465 ± 2	-73	-
Red site-saturation mutagenesis			
D121E/T125C/A256M (GRr3)	619 ± 0	81	-
T125C/**F185T**/A256M	587 ± 1	49	-

Table S3. Spectrally-shifted variants identified from the second round of site-saturation mutagenesis. New mutations are shown in bold and parent mutations in plain text. The absorption maxima (λ_{max}) represent averages, with standard error, of three biological replicas that were grown and extracted separately. Shifts are reported with respect to wild-type λ_{max}. H^+-pumping activities were determined using a dye-efflux assay (see Methods), with (-) no detectable activity, (+) activity that is less than 50% of WT, and (++) activity that is more than 50% of WT. Variants that were included in the blue- and red-shifted recombination libraries are indicated with a *.

2.2.6 Materials and methods

Plasmids and bacterial strains

The gene coding for GR was obtained on the GR_pkj900 plasmid from Janos Lanayi. GR was amplified by PCR using primers that excluded the stop codon (Table S6, primers 1 and 2). The PCR product was cloned by one-step isothermal assembly[51] into an NdeI and NotI digested pET21a expression plasmid (EMD Millipore, Darmstadt, Germany), adding a flexible C-terminal linker that is five amino acids long and a His_6-tag. This generated the pETME10 (GR) expression plasmid. To construct a translational fusion of GR with a C-terminal CFP, we linearized the pETME10 plasmid with XhoI and subsequently purified it using agarose gel. CFP was amplified by PCR using primers with an overhang to the linearized plasmid. DNA fragments were then assembled using one-step isothermal DNA assembly. All constructs were verified by sequencing (Laragen, Culver City, CA, USA) using T7-specific primers. Sequences for the finished His-tagged GR protein and GR-CFP fusion construct can be found in the supplement. All cloning was performed in the *E. coli* strain DH5α. The *E. coli* strain BL-21 (DE 3) was used for expression in all experiments.

Generation of recombination libraries

The red recombination library was designed by combining all red-shifting mutations that did not destroy the proton-pumping ability. This yielded a library of 216 variants (obtained by multiplying the possible codons at each mutagenized site; Fig. S5b). If the same criteria were used to make the blue-shifted recombination library, it would result in a library of over 9000 variants. This number was too large to screen, and the blue-shifted recombination library was therefore reduced by setting a threshold for clones with an

absorption maximum below 528 nm for sites with more than one mutation. This reduced the library size from 9000 to 600 variants (Fig. S5b). Recombination libraries were constructed by amplifying the gene in fragments such that all mutation sites were either covered by mutagenic primers or included by mixing mutated backbones as templates in PCR. The relative binding site of primers used to generate each fragment is shown in Fig. S5a. Primers are listed in Table S6. For each site where multiple primers are listed, these were mixed at ratios resulting in even generation of all desired codons. For the red library, primers 43–48 and 49–52 were used to mutate T125, L129, W222, and P226 in one PCR product. Primers 53 and 54 were used to amplify the plasmid backbone from a mix of plasmids containing the WT codon at A256 and the codon for A256M. For the blue library, primers 62 and 63 and 64 were used to generate a PCR product where sites S181 and A256 were mutated. Primers 55 and 56–61 were used to amplify the plasmid backbone while at the same time mutating sites M158, G162, and E166 from a mix of plasmid containing the WT codon at V126 and the codon for V126A. The PCR fragments were ligated using one-step isothermal assembly and transformed into *E. coli*.

Expression of libraries

Single *E. coli* BL21 (DE3) colonies transformed with library plasmids or control plasmid (parent) were picked to inoculate 200 µL LB media containing 100 µg/mL of ampicillin in 96-deep-well plates with 2 mL well volume (Greiner Bio-One, Kremsmünster, Austria). The plates were covered with a microporous membrane (Easy App™, cat. no. 2978-5827; USA Scientific, Ocala, FL) and incubated in a rotary shaker at 225 rpm, 37 °C, and 80% humidity. The overnight cultures were diluted 1:20 in LB–ampicillin media to a final volume of 1 mL in 96-deep-well plates and further incubated 225 rpm, 30 °C, and 80% humidity for 2 h. Expression was induced through the addition of 5 µL of 100 mM IPTG and 2 mM retinal in 95% EtOH/5% H_2O to a final concentration of 0.5 mM IPTG and 10 µM retinal. Protein expression proceeded for 4 h at 225 rpm, 30 °C, and 80% humidity in the dark. The *E. coli* cells were then collected by centrifugation at 4500 RCF (*r*elative *c*entrifugal *f*orce) for 10 min in a swing-out centrifuge (Allegra 25R; Beckman Coulter, Brea, CA).

Method for screening GR spectral tuning libraries

To measure the absorption spectrum, the GR protein first must be extracted from the *E. coli* membrane. Following library expression (see above), we re-suspended cell pellets in 100 μL extraction buffer [20 mM Tris–HCl, 200 mM NaCl, and 0.15% (w/v) DDM (pH 7.5)] and frozen at − 20 °C overnight to improve cell lysis. The pellets were thawed at room temperature. We added 100 μL extraction buffer containing 1.4 mg/mL lysozyme and a small amount of DNase I to the wells. Extraction was allowed to proceed at room temperature for 30 min in the dark. Cell debris was subsequently pelleted by centrifugation at 4500 RCF for 10 min. Rhodopsins were purified from the supernatant using Ni-NTA affinity chromatography in a 96-well plate format. For this purpose, each well of a 96-well filter plate (Acroprep™, 1 mL, 1.0 μm glass fiber, Pall Corp., Port Washington, NY) was filled with 125 μL Ni-NTA agarose beads (cat. no. 30230, QIAGEN). The rhodopsin-containing supernatant was transferred to the wells and incubated for 5 min at room temperature followed by a single washing step with 400 μL wash buffer [20 mM Tris–HCl, 200 mM NaCl, 0.15% (w/v) DDM, and 80 mM imidazole (pH 7.5); incubation, 1 min] and one elution step {200 μL elution buffer [20 mM Tris–HCl, 200 mM NaCl, 0.15% (w/v) DDM, and 400 mM imidazole (pH 7.5)]; incubation time, 5 min}. After each incubation step, liquids were forced through the filters by centrifugation (200 RCF, 2 min). Absorption spectra of the purified rhodopsins were recorded in a 96-well microtiter plate from 420 nm to 680 nm in 3 nm steps with 5 flashes per measurement (infinite M200; Tecan).

Analysis of spectral tuning data

Data from the spectral tuning libraries were analyzed and processed using Excel (Microsoft), as well as custom software in Python[§]. A nine-data-point smoothing function was applied to all measured spectra to decrease the effect of noise in the measurements. The λ_{max} of each clone was then computed. Those clones with a λ_{max} that was more than 5 nm shifted away from the parent protein and had an absorption level that was significantly above background were re-screened in quadruplicate and subsequently sequenced.

Fluorescence screening

Following library expression (see above), we re-suspended cell pellets in 700 μL of 200 mM NaCl. Transparent 96-well, flat-bottom plates were pre-aliquoted with 20 μL of 500 mM potassium phosphate buffer at pH 7. A multi-channel pipette was used to transfer

180 μL of cells to the buffer-containing wells, for a final concentration of 180 mM NaCl and 50 mM potassium phosphate buffer. Fluorescence measurements were performed using a Tecan plate reader, with the instrument mode that was set to "Fluorescence Top Reading" with multiple reads per well (2 × 2 square). Other instrument parameters included manually setting the gain (100), number of flashes (25), and integration time (20 μs). In Fig. 8c, GR(D121E/T125C/A256M) is fused to CFP and the *Normalized Fluorescence* is defined as A*(Opsin Fluorescence/CFP Fluorescence) where A is an arbitrary scalar.

2.3 Directed evolution of a far-red fluorescent rhodopsin

[7] McIsaac, R. S. et al. (2014). "Directed evolution of a far-red fluorescent rhodopsin". In: *Proceedings of the National Academy of Sciences of the United States of America* 111(36), pp. 13034-9. doi: 10.1073/pnas.1413987111.

2.3.1 Transferring GR mutations to Arch increases fluorescence

Although Arch and GR share low overall sequence identity, 16 of the 20 retinal binding pocket residues (defined as amino acids within 5 Å of retinal in Arch) are conserved between the two (Fig. S1). The mutations of a bright GR variant discovered in our previous directed evolution study of GR[6], GR(D121E/T125C/A256M), which contains the desirable D→E substitution at the Schiff-base counter ion, map to D95E, T99C, and A225M in Arch, respectively (Fig. S1). We recombined these mutations in Arch and identified two variants, Arch(D95E/T99C) (here referred to as Arch(DETC)) and Arch(D95E/T99C/A225M) (here referred to as Arch(DETCAM)), that exhibit large red shifts in λ_{max} compared with wild-type Arch (Fig. 1A) as well as an approximately fivefold increase in fluorescence in *Escherichia coli* at pH 6 (Fig. 1B). No other combinations of D95E, T99C, and A225M resulted in large changes in λ_{max} or improved fluorescence over wild-type Arch. Arch(DETC) and Arch(DETCAM) exhibited nearly identical levels of fluorescence (Fig. 1B). Because the A225M mutation did not further increase fluorescence in Arch(DETC), we chose to focus on Arch(DETC) for further characterization and engineering.

2.3.2 Increased Arch fluorescence is retained when expressed in mammalian cells

Because Arch is of interest for optogenetics applications in mammalian cells, we tested the ability of Arch(DETC) to express and fluoresce in a mammalian cell line. The D95E and T99C mutations were made in a mammalian codon-optimized version of Arch designed with golgi and endoplasmic reticulum export domains for enhanced membrane localization in mammalian neurons[52]. Human embryonic kidney (HEK293) cells were transfected with the mammalian Arch and Arch(DETC) constructs and imaged following stimulation with a 633-nm laser. We found that Arch(DETC) had ~4.5-fold improved fluorescence over Arch in HEK293 cells (**Fig. 5**).

2.3.3 Main figures

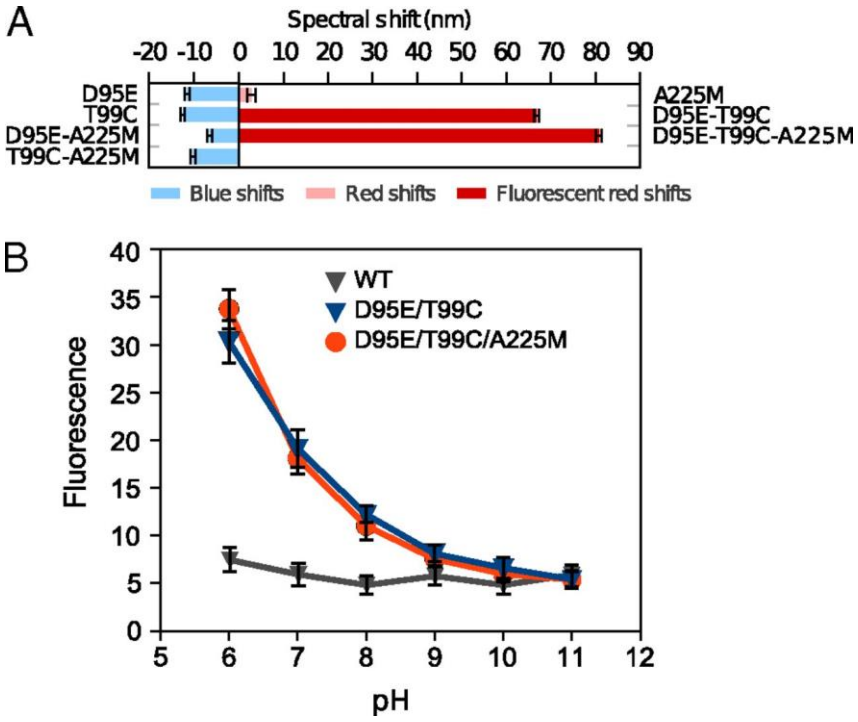

Fig. 1. Measuring the effects of mutations on Arch absorption maximum (λ_{max}) and fluorescence. (*A*) Quantifying the shift in λ_{max} between purified Arch and seven different mutants at pH 7.5. (*B*) Measuring the dependence of Arch, Arch(DETC), and Arch(DETCAM) fluorescence on pH.

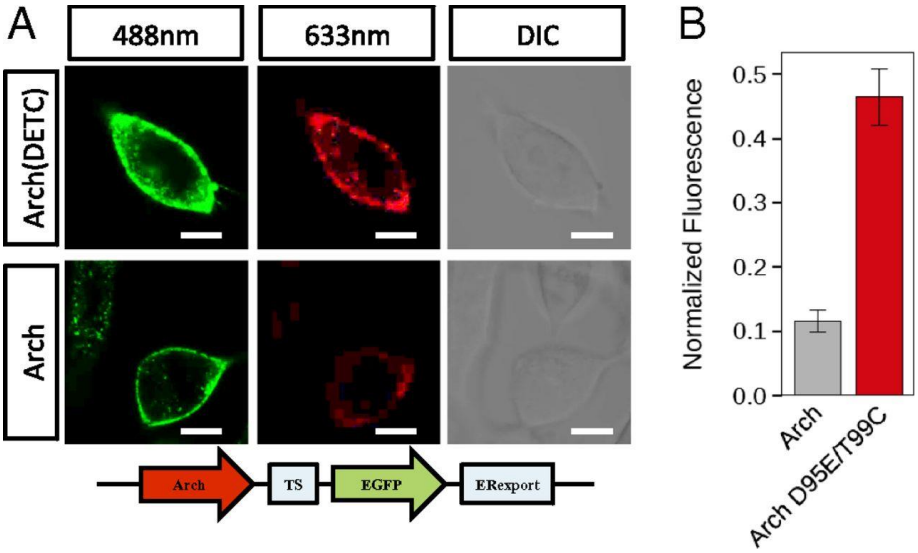

Fig. 5. Live-cell imaging of HEK293 cells expressing Arch and Arch(DETC) fused to EGFP. (*A*) HEK293 cells imaged following laser excitation at 488 nm or 633 nm. (Scale bars: 10 µm.) (*B*) Fluorescence of Arch and Arch(DETC) (12 cells each) normalized for total expression using the EGFP tag. Error-bars represent SEMs.

2.3.4 Supplementary figures

GR	D121	W122	T125	V126	L129	M158	I159	G162	E166	G178	S181	T182	F185	W222	Y225	P226	Y229	D253	A256	K257
Arch	D95	W96	T99	T100	L103	M128	I129	G132	A136	W148	S151	T152	M155	W192	Y195	P196	W199	D222	A225	K226

Fig. S1. Structure-guided alignment of amino acid residues in the retinal binding pockets of Arch and Gloeobacter violaceus rhodopsin (GR).

2.4 Archaerhodopsin variants with enhanced voltage-sensitive fluorescence in mammalian and Caenorhabditis elegans neurons

[6] Flytzanis, N. C.*, Bedbrook, C. N.* et al. (2014). "Archaerhodopsin variants with enhanced voltage-sensitive fluorescence in mammalian and Caenorhabditis elegans neurons". In: *Nature Communications* 5:4894. doi: 10.1038/ncomms5894.

2.4.1 Introduction

The study of brain circuitry encompasses three frames of reference: neuron-level spiking activity, circuit-level connectivity, and systems-level behavioral output. A pervasive goal in neuroscience is the ability to examine all three frames concurrently. Fluorescent sensors, which enable measurements of simultaneous changes in activity of specific populations of neurons, are envisioned to provide a solution[9,53–56]. Successful detection of both high-frequency trains of action potentials and subthreshold events in neuronal populations *in vivo* requires a genetically encoded voltage indicator (GEVI)[57] with

fast kinetics, high sensitivity, and high baseline fluorescence. Recent developments of genetically encoded calcium[9] and voltage sensors[58–60] have yielded progress towards achieving this goal. The calcium sensor family GCaMP has been used to monitor populations of neurons in intact behaving organisms[55]. However, the detection of fast-spiking activity, subthreshold voltage changes and hyperpolarization is difficult with GCaMP due to its relatively slow kinetics and reliance on calcium, a secondary messenger, flux into the cell[9,61,62]. Newer iterations of voltage-sensitive fluorescent proteins based on fusions with circularly permuted GFP, for example, ASAP1[58], improve on both the speed and sensitivity of previous sensors, for example, Arclight[63], but are still limited by the ability to be combined with optogenetic actuators[4,64,65]. This spectral overlap prohibits the combined use of these sensors with opsins for all-optical electrophysiology. Currently available sensors are not able to meet all the needs for optical imaging of activity *in vivo*, calling for continued efforts to evolve GEVIs.

Archaerhodopsin-3 (Arch)[4,64–66], a microbial rhodopsin proton pump that has recently been introduced as a fluorescent voltage sensor[8], is fast and sensitive but suffers from low baseline fluorescence and strong inhibitory photocurrents. Previous optimizations of Arch successfully reduced photocurrents, for example, Arch D95N[8] and Arch EEQ[67], and increased sensitivity and speed, for example, QuasArs[60], but have still to enable its use *in vivo*. All previous *in vivo* voltage sensing has been accomplished using lower power of fluorescence excitation light than is possible with reported Arch variants to date[9,54,59]. For example, Arch WT[8] uses × 3,600 higher intensity illumination than ASAP1[58]. The high laser power used to excite Arch fluorescence causes significant autofluorescence in intact tissue[57] and limits its accessibility for widespread use.

Here we report two Arch mutants (‘Archers’: Arch with enhanced radiance), Archer1 (D95E and T99C) and Archer2 (D95E, T99C and A225M) with improved properties for voltage sensing. These mutants exhibit high baseline fluorescence (× 3–5 over Arch WT), large dynamic range of sensitivity (85% $\Delta F/F$ and 60% $\Delta F/F$ per 100 mV for Archer1 and Archer2, respectively) that is stable over long illumination times, and fast kinetics, when imaged at × 9 lower light intensity (880 mW mm^{-2} at 655 nm) than the most recently reported Arch variants[60] (and × 20.5 lower than Arch WT[8]). We demonstrate that Archer1’s improved

characteristics enable its use to monitor rapid changes in membrane voltage throughout a single neuron and throughout a population of neurons *in vitro*. Although Archer1 has minimal pumping at wavelengths used for fluorescence excitation (655 nm), it maintains strong proton pumping currents at lower wavelengths (560 nm). We show that this single protein, Archer1, is a bi-functional tool that provides both voltage sensing with red light and inhibitory capabilities with green light. Finally, we demonstrate that Archer1 can detect small voltage changes in response to sensory stimulus in the context of intact multicellular organisms such as *C. elegans*.

2.4.2 Results

The combination of D95E, T99C and A225M mutations was first identified in a site-saturation mutagenesis library of the proton pump *Gloeobacter violaceus* rhodopsin (GR) designed to evolve for spectral shifts[6]. Far-red shifted mutants of the GR library were then screened for fluorescence intensity in *Escherichia coli*, which revealed numerous hits with higher fluorescence than GR WT[6]. The corresponding mutations found in the most intensely fluorescent variants can be transferred to the homologous residues of Arch WT (Supplementary Fig. 1) and greatly improve its quantum efficiency and absolute brightness[12]. The selected mutants were expressed in neurons to test if their improved characteristics were maintained in a mammalian system.

Characterization of two new mutant Arch voltage sensors

Arch variants designed with TS and ER export domains for enhanced membrane localization[52] (Fig. 1a and Supplementary Fig. 1b) were screened in neurons for enhanced baseline fluorescence and decreased photocurrents at imaging wavelengths, compared with Arch WT[8]. Of the Arch variants screened, Archer1 and Archer2 exhibited ~5 × and ~3 × increased fluorescence, respectively, over Arch WT (Fig. 1a). Archer1 and Archer2 also have × 55 and × 99 reduced photocurrents in response to 655 nm laser illumination, respectively, when compared with Arch WT (Fig. 1b and Supplementary Fig. 2a). Archer1 exhibits a peak current on initial laser exposure, which then reaches a residual average steady state of 5.6 pA, while Archer2 produces no peak current, and an average steady state of 3.1 pA (Fig. 1b and Supplementary Fig. 2b,c). Arch variants were also screened for increased voltage

sensitivity and faster kinetics compared with previously reported variant Arch EEQ[67]. Voltage sensitivity was measured as a fluorescence response to steps in membrane potential ranging from −100 mV to +50 mV. Due to Arch EEQ's lower baseline fluorescence, its single-cell fluorescence traces show considerably more noise than those for Archer1 and Archer2 (Fig. 1c). Archer1 shows the highest voltage-sensitive fluorescence, as depicted by single-cell sensitivity measurements (Fig. 1c and Supplementary Movie 1), and by the averaged traces (Fig. 1d, Supplementary Fig. 3). Facilitated by Archer1's increased baseline fluorescence, imaging can be done with short 1 ms exposure times and at lower laser intensities (880 mW mm^{-2}) than previously published Arch-based sensors[8,60,67]. To characterize the stability of Archer1's fluorescence, sensitivity was measured before and after prolonged laser illumination. Archer1 showed no reduction in voltage sensitivity over the 10–15 min timeframe measured (Supplementary Fig. 4).

Sensitivity kinetics enables comparison across sensors

The choice of a specific voltage sensor for a given experimental application depends on whether the sensor will yield a significant fluorescence change in response to a given voltage change within the timeframe of interest. Traditionally, sensitivity is quantified by measuring the steady-state fluorescence change for a step in voltage[8,58–60,63,67], but the steady-state value does not provide information about the initial dynamics of the fluorescence response (sensor kinetics). The methods for kinetic analysis vary with different types of sensors. Following a previously used method for Arch-based sensor kinetics[59,67] , we compared Archer1 with Arch WT by normalizing the fluorescent responses of each sensor during a 1 s voltage step (−70 mV to +30 mV) to the steps maximum fluorescence. These results indicate very similar kinetics between the two (Fig. 1e), without addressing Archer1's × 35 larger change in fluorescence. The large time scale of these voltage steps is not relevant for neuronal applications. However, normalizing over a shorter time scale produces variable results depending on the time point used for normalization (Fig. 2b). A method that considers the sensitivity of a sensor on the time scale relevant to an action potential is necessary.

Our proposed method for analysis, sensitivity kinetics (*SKi*), expands on the traditional method by providing $\%\Delta F/F$ for any given voltage change over time (Fig. 2a). With this method, both the sensitivity and kinetics can be compared simultaneously among

sensors. *SKi* is calculated by evaluating the slope of the fluorescence response to steps in voltage for each time point after the step's initiation. The sensitivity slopes are then plotted over time (Fig. 2a,c). Characterization of the *SKi* for Arch variants reveals that Archer1 produces the largest changes in fluorescence of the sensors we tested (Fig. 2d), within any timeframe.

Tracking action potentials in primary neuronal cultures

Action potentials were evoked in cultured rat hippocampal neurons expressing Archer1 through current injection. Archer1 fluorescence is capable of tracking action potentials in both individual processes and the cell body (Fig. 3a,b and Supplementary Movie 2). In addition, the magnitude and shape of dendritic fluorescence changes closely mimic that of the cell body in response to the same event. As predicted by the *SKi*, Archer1 fluorescence, with a >6 × increase in signal-to-noise ratio (SNR), more closely follows the electrical recording of action potentials than Arch EEQ at similar frequencies (Fig. 3c,d). Archer1 exhibits a large percentage change in fluorescence in response to action potentials (25–40% $\Delta F/F$), and can track 40 Hz firing rate as well as simulated changes in membrane voltage occurring at 100 and 150 Hz (>50% $\Delta F/F$) (Fig. 3e,f). The ability to follow action potential throughout neurons by imaging with significantly lower laser intensity (880 mW mm^{-2}) is enabling for monitoring voltage-sensitive fluorescence *in vivo*.

Archer1 functions as a voltage sensor and inhibitory actuator

All-optical electrophysiology requires an optical method for both sensing and perturbing cells. Recent work[60] presented a construct with dual capabilities: voltage sensing and neuronal activation at distinct wavelengths through co-expression of a sensor and a light-gated channel. Archer1 also provides two useful functionalities, both in a single protein. While minimally active with high intensity 655 nm laser illumination (880 mW mm^{-2}), Archer1 is significantly more active at low intensity 560 nm light-emitting diode (LED) illumination (3 mW mm^{-2}) (× 51 at peak and × 35 at steady state) (Fig. 4a,b). The hyperpolarizing photocurrents generated by Archer1 in response to green light successfully inhibit action potentials, while red light does not (Fig. 4c,d). Thus, Archer1 can induce inhibitory currents with green light and sense activity with red.

Optical monitoring of cultured neuronal networks

Fluorescent voltage sensors should enable the detection of spiking activity across all neurons in a population. Original Arch variants require the use of high optical magnification combined with binning and heavy pixel weighing[67] to detect modest changes in fluorescence, due to low baseline. Until recently[60], these stringent imaging requirements had prevented microbial rhodopsin-based voltage sensors from being used to monitor multiple cells simultaneously. Archer1, similar to QuasAr[60], by virtue of its increased fluorescence and higher *SKi,* allows simultaneous imaging of activity for a population of cells while perturbing only one of them through current injection (Fig. 5a, schematic). Within the same optical field, we tracked the fluorescence of three cells with different behaviors: one showed a step change (due to an induced voltage step), one had spontaneous spikes that increased concurrently with the step and one remained unchanged (Fig. 5a, traces).

Optical monitoring of sensory neurons in behaving C. elegans

A major application for voltage sensors is all-optical neuronal activity monitoring in model organisms in which electrophysiological recordings are inherently difficult, for example, *C. elegans.* The improved fluorescence and *SKi* of Archer1 have enabled us to extend its use from cultured cells to live, behaving nematodes. To test whether Archer1 will work in *C. elegans,* we examined the olfactory neuron AWC-ON (WormBase cell WBbt:0005832), one of the pair of C-type Amphid Wing cells. Previously, sensory-evoked Ca^{2+} transients that were monitored using GCaMP show fluorescence increase on odor removal, which peaks within 10 s and gradually decreases over minutes post stimulation[68]. To monitor the small voltage changes underlying this effect, we expressed Archer1 in AWC-ON, and observed fluorescence changes in response to turning off the odorant stimulus (isoamyl alcohol) in anesthetized and non-anesthetized animals. According to Kato *et al.*[69], the chemosensory responses in AWC neurons are not affected by the application of cholinergic agonist. As shown in Fig. 5b–d, Archer1's fluorescence indicates that voltage transients peak within 2 s and end 10 s after turning off stimulus (Fig. 5c and Supplementary Fig. 5). These observed fluorescence changes, which correspond to small reported changes in AWC membrane voltage[70], validate the sensor's *in vivo* utility. A combination of results from Archer1 and GCaMP experiments can be used to better understand the dynamics of *C. elegans* voltage-gated calcium channels.

2.4.3 Discussion

All-optical methods for *in vivo* recording will require a GEVI with fast kinetics, high sensitivity, high baseline fluorescence and compatibility with optical methods for controlling neuronal activity. Here we report an Arch mutant, Archer1, in which these combined improvements enable the accurate tracking of action potentials at high speed, the detection of simultaneous activity within populations of neurons, wavelength-specific inhibition of neuronal activity and the real-time observation of voltage changes in response to a stimulus in live nematodes. Fluorescence measurements of Archer1 and Archer2 were achieved at lower intensity of laser illumination than has been possible in experiments using previously reported Arch variants[8,60,67]. Reduction in excitation light intensity required for fluorescent measurements increases the accessibility of Arch-based voltage sensors and their potential use *in vivo*.

Archer1 is an enhanced voltage sensor under red light, and it also enables inhibition of action potentials under green light. Recent work has been done to generate an all-optical system for neuronal excitation and voltage sensing (Optopatch[60]). Archer1, on the other hand, provides the first example of a combination of wavelength-specific sensing and hyperpolarization with a single protein. This wavelength-specific bi-functionality can enable all-optical dissection of a neural network through targeted inhibition and global fluorescence monitoring. Tools like Archer1 and Optopatch could be used for all-optical loss and gain of function circuit analysis, respectively.

Voltage sensors can also provide insights into neuronal response to stimuli in organisms in which electrophysiology is challenging, such as *Caenorhabditis elegans* and *Drosophila melanogaster*. Archer1 represents the first genetically encoded voltage sensor that has been used in live, behaving nematodes. This work provides a foundation for more detailed characterization of cell types with unknown voltage dynamics as well as fast-spiking muscle cells in *C. elegans*[71]. Additional applications of this tool likely include other transparent organisms, such as fly larvae and zebrafish, where a fluorescent voltage sensor could be used to dissect neural circuitry.

Until recently, due to their low baseline fluorescence[57], Arch-based sensors were not compatible with *in vivo* applications. This work on Archer1, as well as recent work on

QuasArs[60], demonstrates that Arch-based sensors are not fundamentally limited, but can be used for a variety of neuronal applications, including *in vivo*. Our data show that variants of Arch are capable of increased fluorescence, enabling practical detection, while retaining Arch WT's superior speed and dynamic range compared to XFP-based sensors[72]. Even though this work uses the lowest excitation intensity for an Arch-based sensor (<5% original illumination intensity of Arch WT[8], ~60% of Arch EEQ[67] and 11% of QuasArs[60]), it is still ~200 times higher than that for XFP-based sensors. Given the already fast kinetics and high sensitivity of Archer1, further enhancements to baseline fluorescence could result in a GEVI capable of detecting activity in mammalian neuronal populations *in vivo*.

2.4.4 Main figures

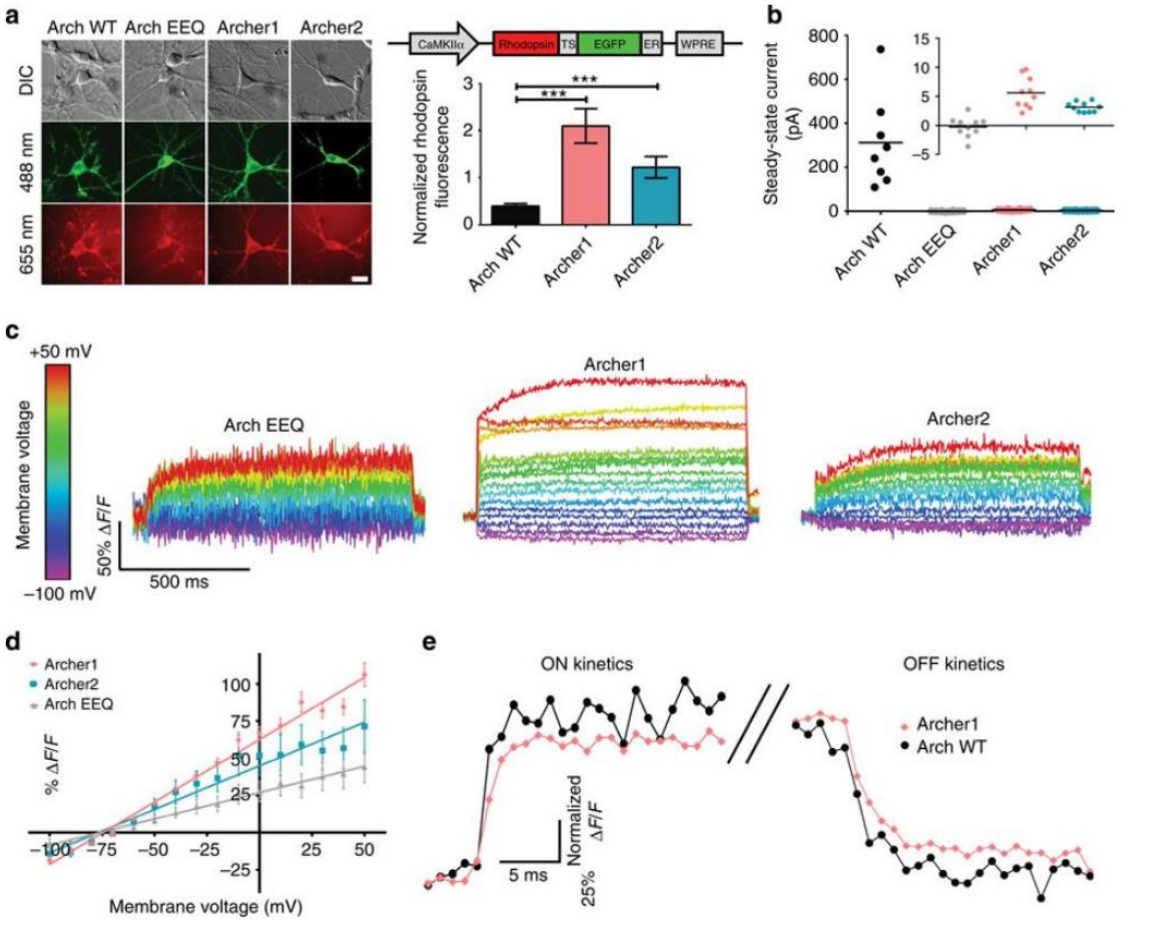

Figure 1: Characterization of Arch variants in mammalian neurons. (**a**) Quantification of Archer1 (*n*=12) and Archer2 (*n*=11) fluorescence compared with Arch WT (*n*=13). Left—

representative images of rhodopsin and fusion protein fluorescence; the published Arch EEQ–EYFP fusion[67] (Supplementary Table 1) is used, while all other sensors are fused to EGFP. Right graph—summary data. Baseline rhodopsin fluorescence normalized to EGFP fluorescence. Arch EEQ not included in comparison, as it has a different fluorescent protein fusion. Right construct—Arch-EGFP fusion vector design. Scale bar, 10 μm. (**b**) Average steady-state photocurrents generated by Arch WT (n=10) and different variants (n=9, 10 and 9 respectively for Arch EEQ, Archer1, and Archer2) in neurons voltage clamped at V=−50 mV. Inset shows low levels of photocurrents expanded to indicate differences between variants. (**c**) Fluorescent responses (imaged at 500 Hz) of single neurons expressing Arch EEQ, Archer1 and Archer2 to voltage-clamped steps in membrane potential. Neurons are held at −70 mV and stepped to voltages ranging from −100 mV to +50 mV in 10 mV increments. (**d**) Sensitivity of Arch variants measured as the functional dependence of fluorescence to change in voltage. Fluorescence changes are averaged over 1,000 ms voltage steps and plotted against voltage. Results exhibit linear dependence with R^2values of 0.98, 0.95, and 0.99 for Archer1 (n=10), Archer2 (n=3) and Arch EEQ (n=5) respectively. (**e**) On/Off kinetics in response to a 100 mV step (−70 mV to +30 mV) for Archer1 (n=10) compared with Arch WT (n=6). %ΔF/F for each time point is normalized to the maximum step response (%ΔF/F averaged over the whole step) (imaged at 1,000 Hz). Laser illumination for Arch WT, Archer1 and Archer2 (λ=655 nm; I=880 mW mm^{-2}) is lower than that used for Arch EEQ (λ=655 nm; I=1,500 mW mm^{-2}). Error bars represent s.e.m. ***P<0.001, NS P>0.05, unpaired student's t-test.

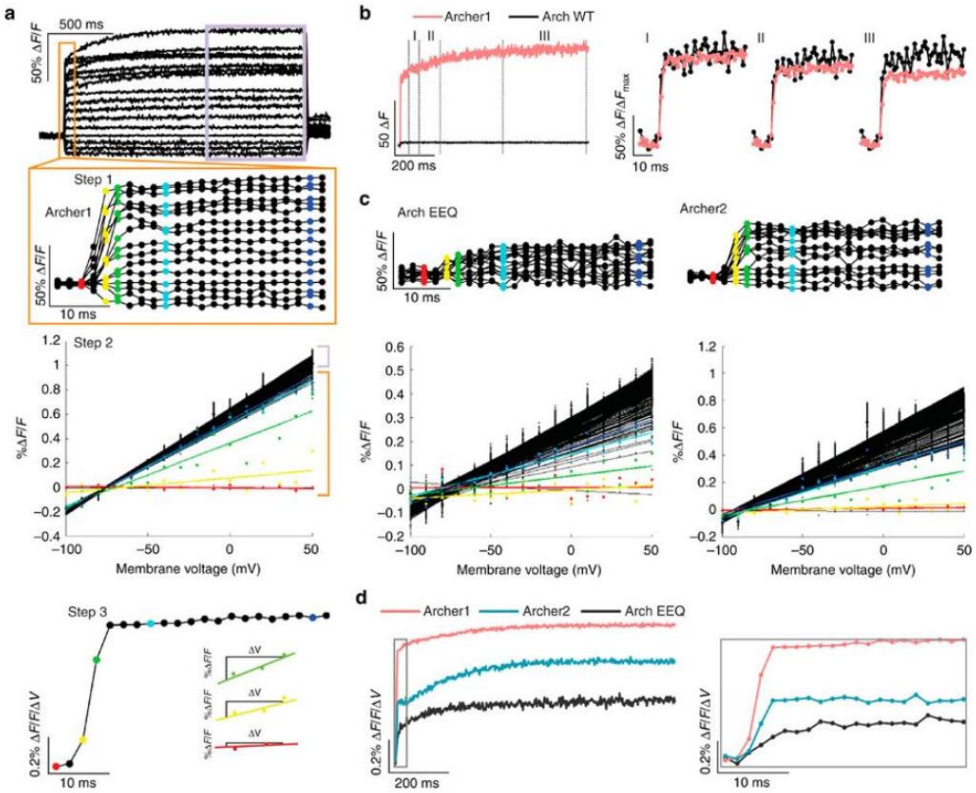

Figure 2: A method for comparing different voltage sensors. (**a**) Overview of the method used to quantify *SKi*. Step 1: averaged fluorescence responses (imaged at 500 Hz) of neurons expressing Archer1 (*n*=10) to voltage-clamped steps in membrane potential. Neurons are held at −70 mV and then stepped to voltages ranging from −100 mV to +50 mV in increments of 10 mV. Step 2: voltage sensitivity of fluorescence is plotted for each time point and a linear fit is calculated. This step assumes a linear dependence of fluorescence on voltage. Step 3: the slope for each linear fit is plotted over time. This measure allows one to calculate %Δ*F*/*F* for a desired voltage change over any time scale. (**b**) Averaged change in fluorescence due to a 100 mV step (−70 mV to +30 mV) of Archer1 (*n*=10) compared with Arch WT (*n*=6) shows significant differences in response magnitude (× 25–30). To compare the kinetics of the two sensors, normalization across the step is necessary. The maximum value within three different regions (I, II and III) is used as a normalization factor, resulting in different apparent kinetics and prompting the need for a different method for kinetic analysis. (**c**) Plotting the voltage sensitivity for each time point with linear best fits for Arch EEQ (*n*=5) and Archer2 (*n*=3) shows a slower rise to the steady-state value than Archer1 (*n*=10). (**d**) Summarizing the *SKi* comparison of Archer1, Arch EEQ and Archer2. Inset expands the first 40 ms. Laser illumination for Arch WT, Archer1 and Archer2 (λ=655 nm; I=880 mW mm^{-2}) and for Arch EEQ (λ=655 nm; I=1,500 mW mm^{-2}).

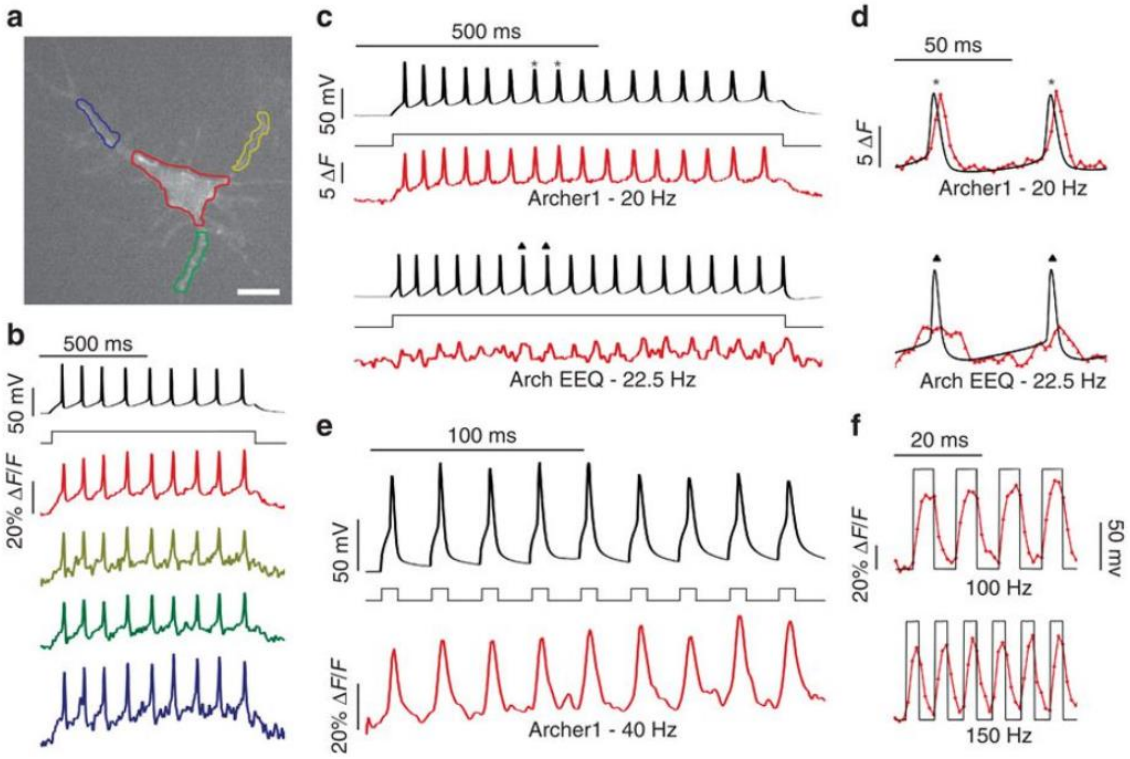

Figure 3: Archer1 fluorescence tracks action potentials in cultured neurons. (**a**) Fluorescence of Archer1 expressing rat hippocampal neuron. Cell body and individual processes are outlined. Scale bar, 10 μm. (**b**) Fluorescence (imaged at 500 Hz) from single-trial optical and electrophysiological recordings of action potentials induced by a step current injection

(800 ms, 50 pA) analyzed for the color-matched somatic and dendritic areas outlined in **a**. (**c**) Fluorescence (imaged at 500 Hz) from single-trial recordings of action potentials in neurons expressing Archer1 and Arch EEQ. Firing of 20 and 22.5 Hz, respectively is generated through a step current injection (800 ms, 50 pA) in current-clamped cells. Fluorescence change is measured in absolute terms, as opposed to a percentage change, due to the lower baseline fluorescence of Arch EEQ. (**d**) Expanded regions of action potentials from **c**. Archer1 shows ~2 × higher change in fluorescence and >6 × increase in SNR (24.03 versus 3.75) when compared with Arch EEQ, allowing it to better track action potential waveforms. Each fluorescent point is 2 ms apart. (**e**) Archer1 fluorescence (imaged at 1,000 Hz) successfully tracks action potentials in cultured rat hippocampal neurons at 40 Hz: higher limit for such cultures, generated through a succession of brief, large amplitude current pulses (5 ms, 500 pA). Individual action potentials at 40 Hz show ~40% change in $\Delta F/F$. (**f**) Single-trial recording of high frequency (100 Hz and 150 Hz) voltage steps (−70 mV to +30 mV) are generated in neurons to test Archer1's ability to detect fast trains of depolarization and hyperpolarization. Fluorescence changes (imaged at 1,000 Hz) exhibited by Archer1 are >50% $\Delta F/F$ for both frequencies and return near baseline between each pulse. Each fluorescent point is 1 ms apart. Laser illumination for Archer1 (λ=655 nm; I=880 mW mm^{-2}) and Arch EEQ (λ=655 nm; I=1,500 mW mm^{-2}). Fluorescence traces in **b**–**e** have undergone background subtraction and Gaussian averaging.

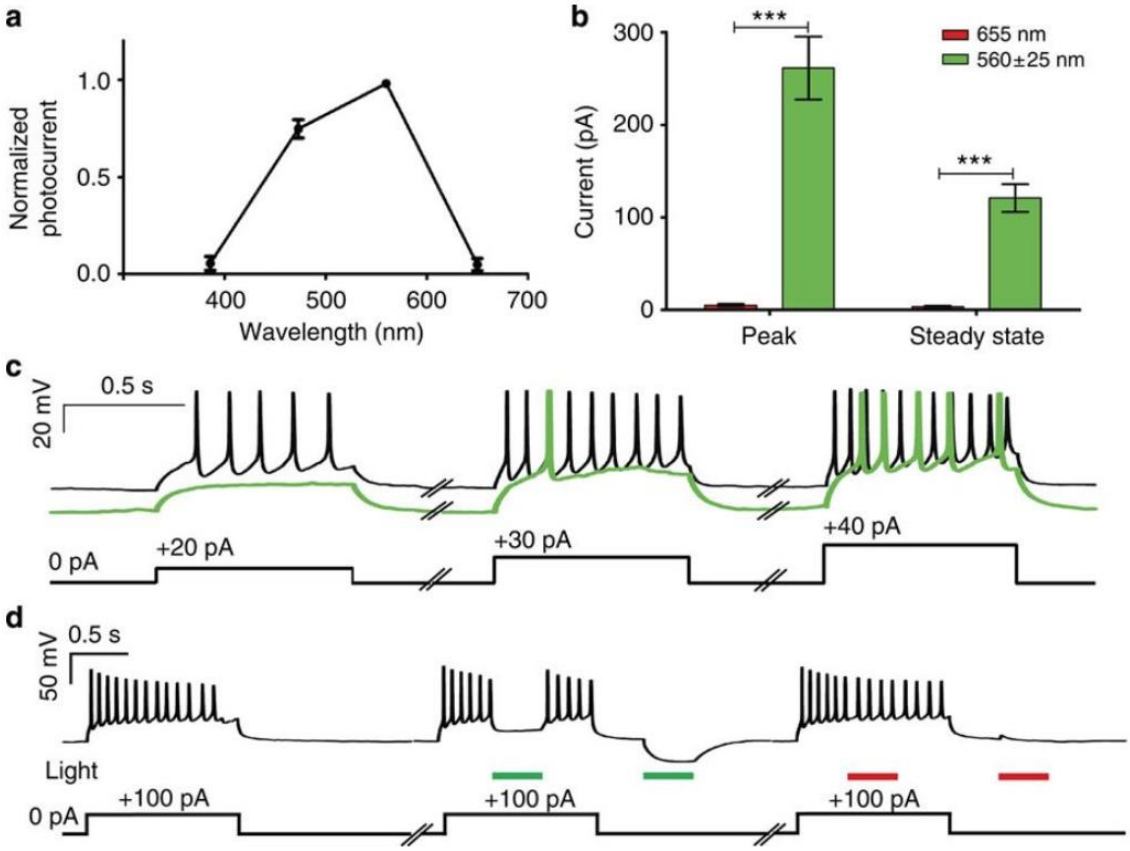

Figure 4: Archer1 acts as either a sensor or actuator at separate wavelengths. (**a**) Normalized steady-state activation spectrum of Archer1 spanning wavelengths between 386–650 nm (n=11). (**b**) Currents induced by low intensity green LED illumination (n=8, λ=560±25 nm; I=3 mW mm^{-2}) are significantly larger than those induced by high intensity red laser illumination (n=16, λ=655 nm; I=880 mW mm^{-2}). (**c**) Archer1 exposed to green light successfully inhibits action potentials induced by step current injections (at 20, 30 and 40 pA) when compared with non-illuminated current injections in the same cell. (**d**) Action potentials induced by a 100 pA current injection (900 ms) are inhibited by a pulse of green light (300 ms; I=3 mW mm^{-2}), while no inhibition of action potentials is observed with a pulse of red laser at the power used to excite fluorescence (300 ms; I=880 mW mm^{-2}). In addition, with no current injection, hyperpolarization is observed with exposure to green, but not red light. Error bars represent s.e.m. ***P<0.0001, unpaired Student's t-test.

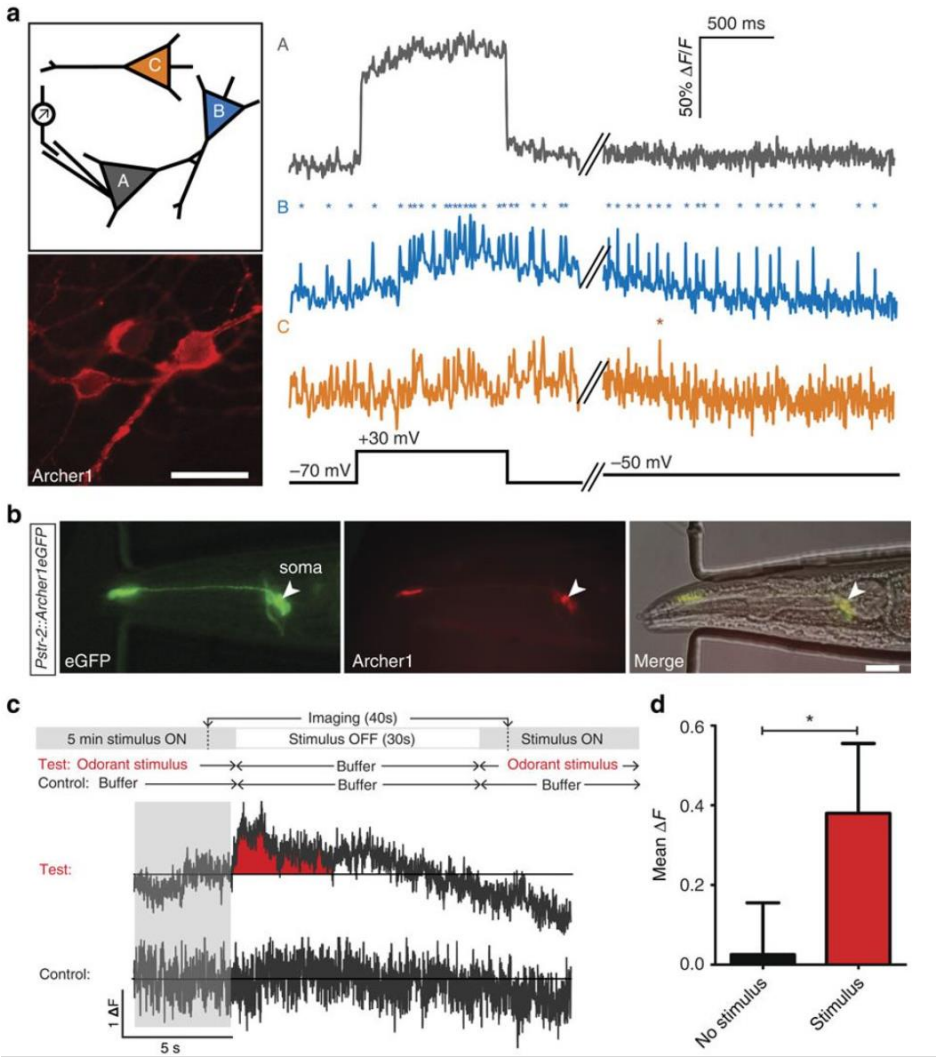

Figure 5: Archer1 tracks activity in populations of cultured neurons and behaving worms. (**a**) Monitoring fluorescence in three Archer1 expressing cultured neurons with electrical stimulation of one cell. Cell A undergoes a voltage clamped 100 mV step and fluorescence

changes in the population are measured simultaneously. Cell A exhibits a step-like increase in fluorescence corresponding to the voltage step. Cell B, whose fluorescence indicates spontaneous firing before the step, shows an increase in firing rate concurrent with the voltage step in Cell A, with continued firing after the step is completed. Fluorescence of Cell C appears not responsive to the voltage step in Cell A. Asterisks indicate action potential-like changes in fluorescence (~35–40% $\Delta F/F$ increase within 10 ms). Scale bar, 20 µm. (**b**) *C. elegans* expressing Archer1 in one AWC neuron shows opsin fluorescence (λ=655 nm; I=880 mW mm^{-2}, 100 ms exposure) co-localizing with fused EGFP fluorescence (λ=485±20 nm; I=0.05 mW mm^{-2}, 100 ms exposure). Scale bar, 20 µm. (**c**) Top: behavioral paradigm: worms are stimulated with odorant (Isoamyl alcohol, IAA) for 5 min, flow is switched to buffer (S Basal) for 30 s, and then odorant flow is restored. On the same worm, a control is performed where odorant is replaced with buffer. Bottom traces: imaging of Archer1 fluorescence (250 Hz) is performed continuously for 40 s, starting 5 s before flow switch. Averaged ΔF traces for two worms are shown. (**d**) Mean fluorescence of the 4-s time window after switch shows a significant increase with stimulus compared with no-stimulus controls (n=4 worms). Fluorescence traces imaged at λ=655 nm; I=880 mW mm^{-2}. Fluorescence traces in **a** and **b** have undergone background subtraction and Gaussian averaging. Error bars represent s.e.m. *P<0.05, paired student's t-test.

2.4.5 Supplementary figures and tables

a

```
Arch-1          MDPIALTAAVGADLLGDGRPETLWLGIGTLLMLIGTFYFIVKGWGVTDKEAREYYSITIL 60
Arch DETC       MDPIALQAGY--DLLGDGRPETLWLGIGTLLMLIGTFYFLVRGWGVTDKDAREYYAVTIL 58
Arch DETCAM     MDPIALQAGY--DLLGDGRPETLWLGIGTLLMLIGTFYFLVRGWGVTDKDAREYYAVTIL 58
                ****** *.   ****************************:*:*******:*****::***

Arch-1          VPGIASAAYLSMFFGIGLTEVQVGSEMLDIYYARYADWLFTTPLLLLDLALLAKVDRVSI 120
Arch DETC       VPGIASAAYLSMFFGIGLTEVTVGGEMLDIYYARYAEWLFCTPLLLLDLALLAKVDRVTI 118
Arch DETCAM     VPGIASAAYLSMFFGIGLTEVTVGGEMLDIYYARYAEWLFCTPLLLLDLALLAKVDRVTI 118
                ******************** **.**********:***:*****************:*

Arch-1          GTLVGVDALMIVTGLVGALSHTPLARYTWWLFSTICMIVVLYFLATSLRAAAKERGPEVA 180
Arch DETC       GTLVGVDALMIVTGLIGALSHTAIARYSWWLFSTICMIVVLYFLATSLRSAAKERGPEVA 178
Arch DETCAM     GTLVGVDALMIVTGLIGALSHTAIARYSWWLFSTICMIVVLYFLATSLRSAAKERGPEVA 178
                ***************:******.:****:**********************:**********

Arch-1          STFNTLTALVLVLWTAYPILWIIGTEGAGVVGLGIETLLFMVLDVTAKVGFGFILLRSRA 240
Arch DETC       STFNTLTALVLVLWTAYPILWIIGTEGAGVVGLGIETLLFMVLDVTAKVGFGFILLRSRA 238
Arch DETCAM     STFNTLTALVLVLWTAYPILWIIGTEGAGVVGLGIETLLFMVLDVTMKVGFGFILLRSRA 238
                ************************************************:*********

Arch-1          ILGDTEAPEPSAGAEASAAD 260
Arch DETC       ILGDTEAPEPSAGADVSAAD 258
Arch DETCAM     ILGDTEAPEPSAGADVSAAD 258
                *************:.****
```

b

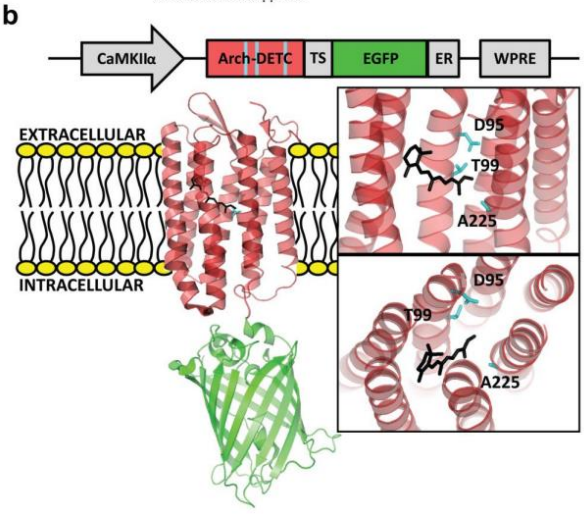

Supplementary Figure 1 | Structural alignment of Arch variants with Arch-1. (a) Sequence alignment via ClustalW2. Arch-1 (Uniprot P69051), Archer1, and Archer2 share 93% amino acid identity. The alignment shows the D95E, T99C and A225M mutations of Archer1 and Archer2 from Arch WT boxed in blue. (b) Archer1 construct design and schematic of location of opsin-fluorescent protein fusion in membrane. Locations of the mutated residues (D95, T99 and A225) are shown in blue and their relative positions to the retinal chromophore in black.

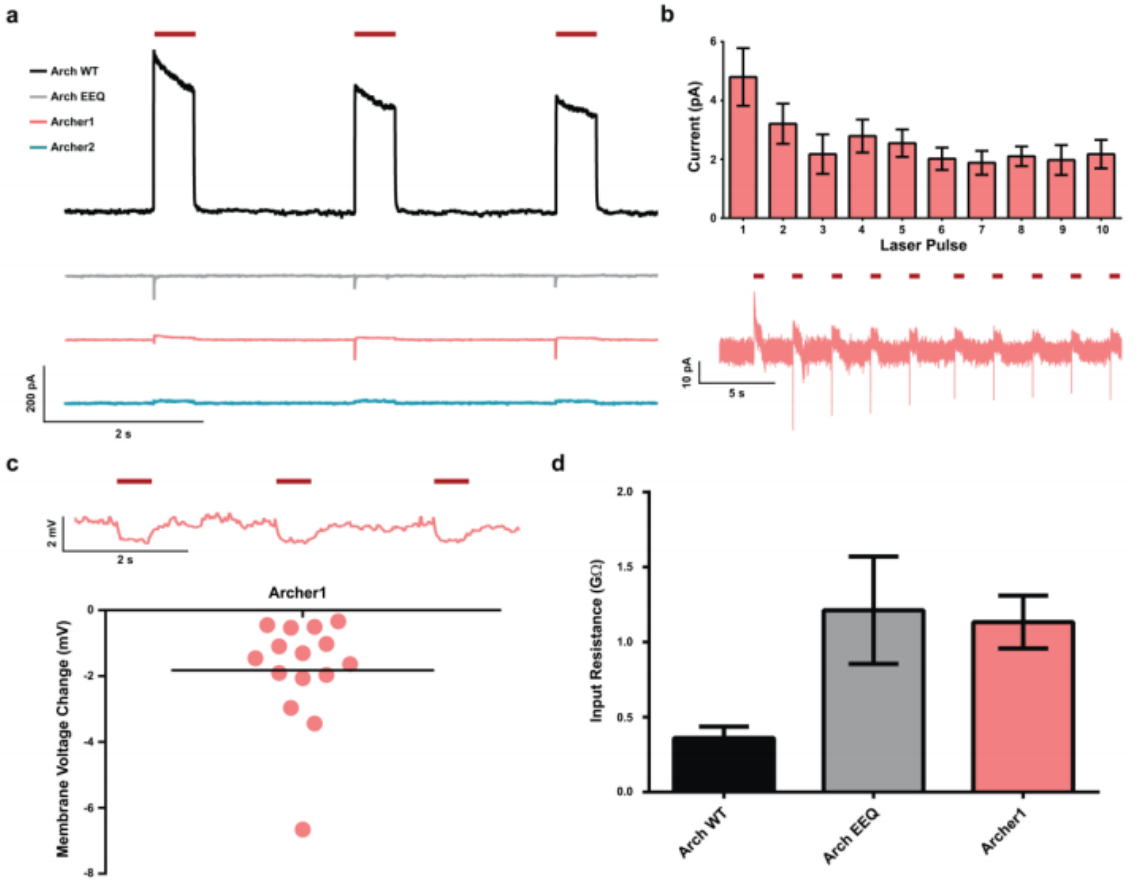

Supplementary Figure 2 | Residual photocurrents of Arch variants and effect on membrane potential. (a) Single trace voltage-clamp recordings of photocurrents in neurons expressing Arch WT and variants in response to three consecutive pulses of laser illumination at the intensity used for fluorescence imaging. Arch EEQ, as previously reported[67], shows no steady-state photocurrent in response to laser illumination, while Archer1 and Archer2 exhibit small steady-state currents. Arch EEQ and Archer1 both respond to laser illumination with a brief peak of depolarizing photocurrent before reaching steady state. This has been observed with microbial rhodopsin-based voltage sensors as previously reported for Mac[60]. (b) Archer1 photocurrent characteristics are measured in response to 10 consecutive laser pulses (n = 10). An initial peak current is generated in naïve cells exposed to laser illumination for the first time. Subsequent pulses reach a lower steady state without a peak. (c) Current clamp recordings of changes in membrane voltage

of neurons expressing Archer1 (n = 15) induced by pulses of laser illumination. (d) Input resistance of patched cells expressing Arch WT (n = 8), Arch EEQ (n = 10) and Archer1 (n = 10) recorded as a measure of quality of the seal break. Laser illumination for Arch WT, Archer1 and Archer2 (λ = 655 nm; I = 880 mW mm-2), and Arch EEQ (λ = 655 nm; I = 1,500 mW mm-2). Error bars represent standard error of the mean (s.e.m.).

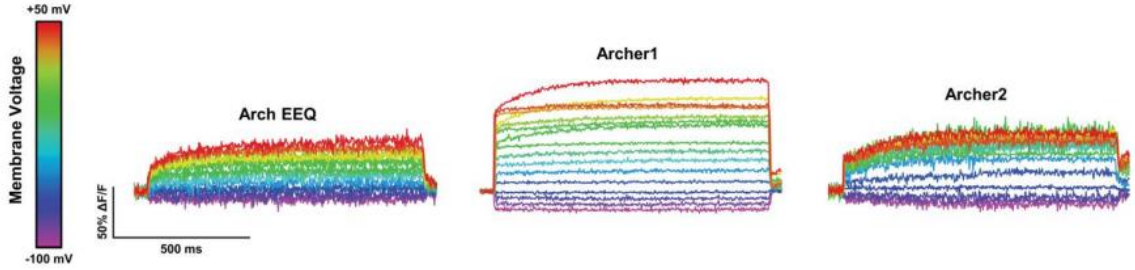

Supplementary Figure 3 | Averaged fluorescence sensitivity of Arch variants. Averaged fluorescence responses (imaged at 500 Hz) of neurons expressing Arch EEQ (n = 5), Archer1 (n = 10) and Archer2 (n = 3) to voltage clamped steps in membrane potential. Neurons are held at -70 mV and then stepped to voltages ranging from -100 mV to +50 mV in increments of 10 mV. Laser illumination for Archer1 and Archer2 (λ = 655 nm; I = 880 mW mm-2), and Arch EEQ (λ = 655 nm; I = 1,500 mW mm-2).

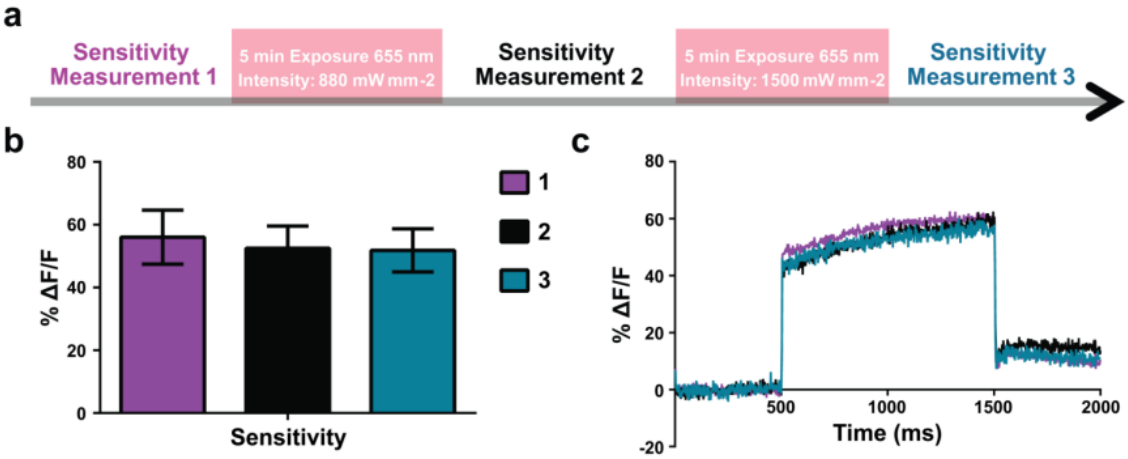

Supplementary Figure 4 | Archer1 fluorescence sensitivity is stable with prolonged illumination. (a) Laser exposure and sensitivity measurement paradigm consists of detecting the sensitivity of fluorescence response to 100 mV voltage step in three consecutive measurements separated by 5 minutes of continuous laser exposures, with the first exposure at 880 mW mm-2 and the second at 1,500 mW mm-2. (b) The average percentage change in fluorescence in response to 100 mV step in voltage does not significantly change after the first (n = 8) or second (n = 6) prolonged laser exposure. (c) Average fluorescence waveforms for the sensitivity measurements described in (a, b) show no change in the characteristics of fluorescence response. Laser illumination for Archer1 (λ = 655 nm; I = 880 mW mm-2). Error bars represent standard error of the mean (s.e.m.).

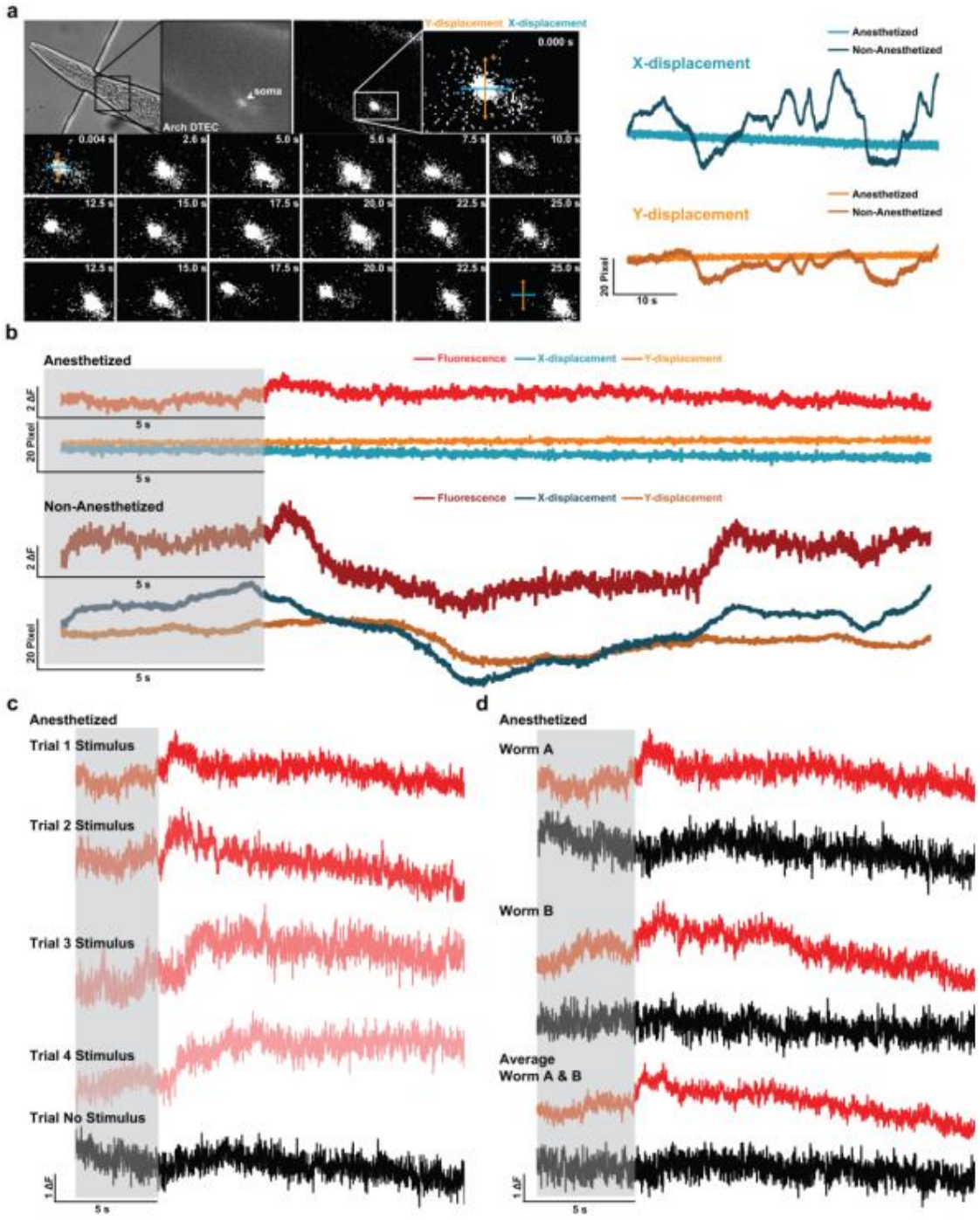

Supplementary Figure 5 | Worm movement and fluorescence in anesthetized vs. non-anesthetized worms. (a) Tracking fluorescence of an AWC cell. Cell location is determined by averaging coordinates of fluorescent pixels above a set threshold and monitoring their position on an x-y coordinate plane over time. Non-anesthetized worms show significant movement in both x (blue) and y (red) direction throughout the stimulation protocol compared to anesthetized worms. (b) Time locked fluorescence and cell movement traces

during a stimulus paradigm indicate that the frequent changes in fluorescence in non-anesthetized worms, not apparent in anesthetized worms, correlates with worm movement. (c) Fluorescence traces of repeated trials of stimulation (red) within the same worm compared to control (black). (d) Single trial fluorescence response to stimulus and control paradigms for two worms (A and B) and the average fluorescence trace of the two. Fluorescence traces imaged at $\lambda = 655$ nm; $I = 880$ mW mm-2. Fluorescence traces (ΔF) in (b)-(d) have undergone background subtraction and Gaussian averaging.

Construct	**Addgene #**
pLenti-CaMKIIa-eArch3.0-EYFP	35514
FCK-Arch-GFP	22217
pLenti-Arch-EEQ	45188

Supplementary Table 1 | Accession codes

Primer	Sequence	Used for
Archfwd	CCGGATCCGCCACCATGGACC	Forward primer for Arch amplification
ERrev	GGGAATTCTCATTACACCTCGTTCTCGTAGC	Reverse primer for Arch amplification
Arch3.0_D95E_T99C_fwd	GCCGAGTGGCTGTTTTGCACCCC	Insertion of D95E and T99C mutations into Arch
Arch3.0_D95E_T99C_rev	GGTGCAAAACAGCCACTCGGCGTAC	Insertion of D95E and T99C mutations into Arch
Arch3.0_A225M_fwd	TTATGGTGTTGGACGTGACTATGAAGGTCGG	Insertion of A225M mutation into Arch
Arch3.0_A225M_rev	AGTCACGTCCAACACCATAACAGCAGAG	Insertion of A225M mutation into Arch
TSrev_into_GFPstart	AGCTCCTCGCCCTTGCTCACCACGTTGATGTCGATCTGG TCCAGGG	Used for amplification and assembly of Arch-TS with EGFP-ERexport
GFPfwd_overlapTSend	ACCAGATCGACATCAACGTGGTGAGCAAGGGCGAGGAG CTG	Amplification of GFP out of FCK-Arch-GFP
FCK-GFPrev_ERexport	CCGAATTCTTACACCTCGTTCTCGTAGCAGAACTTGTAC AGCTCGTCCATGCCGAGAG	Amplification of GFP out of FCK-Arch-GFP and addition of ERexport domain
str-2p-SphI-F2(2K)	CGGGGCATGCGTGGGTAGTTTATGTTGCAATCATCAG	Amplification of *str-2* AWC specific promoter
str-2p-AscI-R2	GGCGGGCGCGCCTTTTATGGATCACGAGTATTCGGACA A	Amplification of *str-2* AWC specific promoter
Arch-NheI-AAA-F	CTTAGCTAGCAAAATGGACCCCATCGCTCTGCA	Amplification and insertion of Archer1eGFP into pSM vector
Arch-EcoRI-R	ATTGGAATTCTTACACCTCGTTCTCGTAGCAGAACTTGTA CAGCT	Amplification and insertion of Archer1eGFP into pSM vector

Supplementary Table 2 | Cloning primers

2.4.6 Supplementary movie captions

Supplementary Movie 1 | Archer1 fluorescence in response to a voltage step. Fluorescent response of an Archer1 expressing rat hippocampal neuron to a voltage-clamped step in membrane potential from -70 mV to +50 mV. Step begins 500 ms into the video and ends 1,000 ms later. Laser illumination for Archer1 is $\lambda = 655$ nm; I = 880 mW mm-2.[1]

Supplementary Movie 2 | Archer1 fluorescence tracks action potentials throughout a neuron. An 800 ms, 50 pA step current injection is applied to a current-clamped, Archer1 expressing rat hippocampal neuron. Action potentials (*) are generated at 11.5 Hz in response to the current injection and Archer1 fluorescence is monitored throughout, showing large changes in fluorescence in the cell body and individual neurites in response to each action potential (visualized as fluorescence blinking). Laser illumination for Archer1 is $\lambda = 655$ nm; $I = 880$ mW mm-2.[1]

[1] = data file is stored at data.caltech.edu

2.4.7 Materials and methods
Ethics statement

All experiments using animals in this study were approved by Institutional Animal Care and Use Committee (IACUC) at the California Institute of Technology.

Sensor constructs

Arch variant constructs were generated by first amplifying EGFP from FCK-Arch-GFP (Accession codes listed in Supplementary Table 1) and adding the ER export domain using GFPfwd_overlapTSend and FCK-GFPrev_ERexport primers (Supplementary Table 2) to make EGFP-ER. Arch-TS was then amplified from pLenti-CaMKIIa-eArch3.0-EYFP (Supplementary Table 1) using Archfwd and TSrev_into_GFPstart primers (Supplementary Table 2), assembled with EGFP-ER using Archfwd and ERrev primers (Supplementary Table 2), and subsequently cloned back into pLenti-CaMKIIa-eArch3.0-EYFP cut with *BamHI* and *EcoRI* restriction enzymes, to make pLenti-CaMKIIa-eArch3.0-EGFP. To make pLenti-CaMKIIa-Archer1-EGFP and pLenti-CaMKIIa-Archer2-EGFP, the D95E, T99C, and A225M mutations were introduced in the pLenti-CaMKIIa-eArch3.0-EGFP vector through overlap assembly PCR using Archfwd, ERrev, Arch3.0_D95E_T99C_fwd, Arch3.0_D95E_T99C_rev, Arch3.0_A225M_fwd, and Arch3.0_A225M_rev primers (Supplementary Table 2) and subsequent cloning back into the backbone via *BamHI* and *EcoRI* sites. pLenti-Arch-EEQ (Supplementary Table 1), an EYFP fusion, was used as a comparison.

To make *Pstr-2::Archer1eGFP::unc-54 3′UTR*, Archer1 was amplified from pLenti-CaMKIIa-Archer1-EGFP using Arch-NheI-AAA-F and Arch-EcoRI-R primers (Supplementary Table 2) and inserted into the pSM vector using *NheI* and *EcoRI* sites.

The *C. elegans* Kozak sequence AAA, and the restriction enzyme sites mentioned above were engineered into the primers[73]. The AWC-specific promoter, which is a 2 kb sequence 5′ to the start codon of *str-2*, was amplified from genomic DNA using str-2p-SphI-F2(2K) and str-2p-AscI-R2 primers (Supplementary Table 2) and cloned into the vector via *SphI* and *AscI* sites.

Primary neuronal cultures

Rat hippocampal cells were dissected from Wistar pups (postnatal days 0–1, Charles River Labs), and cultured at 37 °C, 5% CO_2 in Neurobasal media supplemented with B27, glutamine and 2.5% FBS. Three days after plating, glial growth was inhibited by addition of FUDR. Cells were transfected 4–5 days after plating with Arch WT and variants using calcium chloride. Neurons were imaged 3–5 days after transfection.

Fluorescence imaging

Imaging was performed concurrently with electrophysiology recordings of voltage- and current-clamped cultured rat hippocampal neurons. For both cultured neurons and *in vivo C. elegans* experiments, a Zeiss Axio Examiner.D1 microscope with a 20x 1.0 NA water immersion objective (Zeiss W Plan Apochromat × 20/1.0 DIC *D*=0.17 M27 75 mm) was used. A diode laser (MRL-III-FS-655-1.3W; CNI) with a 650/13 nm excitation filter, 685 nm dichroic mirror and 664 nm long-pass emission filter (all SEMROCK) was used for rhodopsin fluorescence excitation throughout. For cultured neuron experiments Arch WT, Archer1 and Archer2 fluorescence was excited with 880 mW mm^{-2} illumination intensity at the specimen plane, while for Arch EEQ, 1,500 mW mm^{-2} illumination intensity was used. Higher illumination intensity was used for Arch EEQ compared with other Arch variants due to its lower baseline fluorescence with our imaging setup. For *C. elegans* experiments, 880 mW mm^{-2} illumination intensity was used to visualize Archer1 fluorescence. For all experiments, fused EGFP fluorescence was imaged with 485±25 nm LED light using a Lumencor SPECTRAX light engine with quad band 387/485/559/649 nm excitation filter, quad band 410/504/582/669 nm dichroic mirror and quad band 440/521/607/700 nm emission filter (all SEMROCK) at 0.05 mW mm^{-2}.

All fluorescence traces were recorded using an Andor Neo 5.5 sCMOS camera cooled to −30 °C at 500 or 1,000 Hz. Pixels were binned up to 0.54 μm × 0.54 μm to achieve the image acquisition speeds. All recordings were taken using Andor's Solis software.

Electrophysiology

Conventional whole-cell patch-clamp recordings were done in cultured rat hippocampal neurons at >2 days post transfection. Cells were continuously perfused with extracellular solution at room temperature (in mM: 140 NaCl, 5 KCl, 10 HEPES, 2 $MgCl_2$, 2 $CaCl_2$, 10 glucose; pH 7.35) while mounted on the microscope stage. Patch pipettes were fabricated from borosilicate capillary glass tubing (1B150-4; World Precision Instruments, Sarasota, FL) using a model P-2000 laser puller (Sutter Instruments) to resistances of 2–5 MΩ. Pipettes were filled with intracellular solution (in mM): 134 K gluconate, 5 EGTA, 10 HEPES, 2 $MgCl_2$, 0.5 $CaCl_2$, 3 ATP, 0.2 GTP. Whole-cell patch-clamp recordings were made using a Multiclamp 700B amplifier (Molecular Devices, Sunnyvale, CA), a Digidata 1440 digitizer (Molecular Devices), and a PC running pClamp (version 10.4) software (Molecular Devices) to generate current injection waveforms and to record voltage and current traces.

Patch recordings were done simultaneously with imaging for measurements of voltage-sensitive fluorescence. For sensitivity measurements, cells were recorded in voltage clamp with a holding potential of −70 mV for 0.5 s and then 1 s voltage steps were applied ranging from −100 mV to +50 mV in 10 mV increments. Action potentials were generated in current clamp by current injection in either a long step (10–200 pA; 0.8 s) or in short pulses (100–500 pA; 2–10 ms).

Patch-clamp recordings were done with short light pulses to measure photocurrents. Photocurrents induced by the excitation wavelength used for voltage sensing were measured using a 655 nm laser at 880 mW mm^{-2}. Photocurrents induced by green light were measured using 560±25 nm LED at 3 mW mm^{-2}. Photocurrents were recorded from cells in voltage clamp held at −50 mV with 3–10 light pulse trains (0.5 s each pulse; 2 s apart). Voltage changes induced by 655 nm laser at 880 mW mm^{-2} were measured in a current clamp mode with three 0.5 s light pulses separated by 2 s and zero current injection.

To test for inhibitory capabilities of Arch mutants, pulses (300 ms) of illumination with either red laser (655 nm at 880 mW mm^{-2}) or green LED (560±25 nm at 3 mW mm^{-2}) were applied to cells during a 900 ms train of induced action potentials (generated in current clamp by current injections from 30–100 pA).

Action spectra measurements were performed for the following wavelengths: 386±23 nm, 438±24 nm, 485±20 nm, 513±17 nm, 560±25 nm and 650±13 nm with light intensity matched across all experiments at 0.08 mW mm^{-2}. Each light pulse was delivered for 0.6 s with 10 s breaks between light pulses. All wavelengths were produced using LED illumination from a SPECTRAX light engine (Lumencor). Cell health was monitored through holding current and input resistance.

Microinjection and germ line transformation in C. elegans

The transgenic line used in this work is PS6666 *N2; syEx1328[Pstr-2(2k)::Archer1eGFP(*75 ng μl^{-1}*); Pofm-1::RFP(*25 ng μl^{-1})]. *Pstr-2::Archer1eGFP::unc-54 3'UTR* was co-injected with a *Pofm-1::RFP*marker into Bristol N2 using the method described by Mello, *et al.*[74]. The two plasmids were diluted to the desired concentration in water to make a 5 µl injection mix. The injection mix was spun down at 14,000 r.p.m. for 15 min and transferred to a new tube before injection to prevent needle clogging. Late L4 hermaphrodites were transferred to a newly seeded plate and maintained at 22 °C 1 day before injection. The microinjection was performed the next morning when the worms had become young adults. Worms were glued on a 2% agarose pad and covered with Halocarbon Oil (Halocarbon Products Corporation, HC-700) before injection. A quantity of 0.8 µl of the injection mix was loaded into the injection needle. For generating this transgenic line, 32 hermaphrodites (P_0S) were injected for both arms of the gonad. 27 F_1 were identified 3 days after injection based on *Pofm-1::RFP* expression in coelomocytes. Among them, five eventually became stable lines. The best line used in this study was determined by the highest transmission rate and the strongest expression level of Archer1eGFP.

C. elegans in vivo stimulation experiments

Late L4 transgenic worms were transferred to a plate seeded with the mixture of OP50 and all-trans-Retinal (ATR) (Sigma-Aldrich, USA), and maintained at 22 °C in the dark 18 h before imaging. The final concentration of ATR in the mixture was 100 µm (diluted

from 100 mM stock: 100 mg ATR powder dissolved in 3.52 ml 100% ethanol) using fresh OP50. Five times higher concentration of ATR was previously used for wild-type Arch activity in worms. The microfluidic device is adapted for *in vivo* imaging. The PDMS chip contains four buffer inlets, one worm-loading channel and one suction channel connected to house vacuum. Two buffer inlets in the middle are the "buffer" and the "stimulus" channels, which are loaded with the default solution S Basal medium and 1:1,000 isoamyl alcohol (Sigma-Aldrich), respectively. S Basal medium containing 0.15% phenol red (Sigma-Aldrich) is loaded in the side channels for detecting the laminar flow. An ATR-fed worm was first transferred to an empty NGM plate and washed in a drop of S Basal. It was then loaded in the microfluidic chip, where its nose was presented with either the buffer or the stimulus streams. The switch between buffer and stimulus stream was accomplished by changing the flow pressure from the side channels, which was regulated via an external valve controlled using a LabView script (National Instruments). The worm was exposed to the stimulus stream for 5 min (stimulus on), to the buffer stream for 30 s (stimulus off), and to the stimulus stream again. For performing the control experiments on the same worm, the flow switch remained the same, but the stimulus channel was loaded with S Basal. Imaging of Archer1 fluorescence began 5 s before stimulus was switched off and lasted for 40 s. For anesthetized experiments only, 0.1% levamisole (Sigma-Aldrich) was added to the worm-loading channel to minimize movement artifacts.

Data analysis

Unless otherwise noted, all fluorescence analysis was done with raw measurements of cell fluorescence background subtracted. Cells and background regions were selected manually in ImageJ and fluorescence measurements were recorded for each region of interest (ROI) and background fluorescence was subtracted from cell fluorescence.

Sensitivity analysis was performed using background subtracted fluorescence recordings. Baseline fluorescence (mean fluorescence of the cell 20 ms before voltage step) and step fluorescence (fluorescence over whole 1 s voltage step) were used to generate $\%\Delta F/F$ traces for each voltage step. The mean $\%\Delta F/F$ over the entire 1 s step was calculated for each voltage step and then plotted ($\%\Delta F/F$ versus voltage step).

On and off kinetics analysis was performed on fluorescence traces in response to a 100 mV step (−70 mV to +30 mV). Percentage change in fluorescence %Δ*F*/*F* for each time point is normalized to the maximum step response (%Δ*F*/*F* averaged over the whole step).

SKi analysis was performed using time-locked, average %Δ*F*/*F* traces (voltage steps ranging from −100 mV to 50 mV in 10 mV increments) for all cells. At each time point throughout a voltage step (t=0 at time of voltage step trigger), %Δ*F*/*F* was plotted versus the respective voltage step. A linear best fit was then performed for the %Δ*F*/*F* versus voltage step for each time point. The slope of the best fit for each time point was then plotted over time (%Δ*F*/*F*/voltage step versus time).

SNR analysis for action potentials tracked by Archer1 and Arch EEQ fluorescence was performed. SNR was computed as $SNR=\mathrm{abs}(s-n)/\sigma$, where s=peak fluorescence during action potential, n=average of preaction potential noise and σ=s.d. of the preaction potential noise.

Worm AWC cell and background regions were selected manually in ImageJ, fluorescence measurements were recorded for each ROI, and background fluorescence was subtracted from cell fluorescence. The ROI for the fluorescent cell was drawn to contain the cell soma for all time points of the experiment. Δ*F* is reported instead of %Δ*F*/*F* due to low detected baseline fluorescence. Calculating %Δ*F*/*F* would result in amplified signal, as well as amplified noise.

Worm movement analysis was performed on the worm fluorescence traces, which were first thresholded so that only the pixels above a certain threshold are considered pixels of the cell. The cell location was then determined by averaging coordinates of pixels above the set threshold for the first frame in the 10,000 frame experiment to get the coordinates at the center of the cell. A 70 × 70 pixel region around the center of the cell was then set as the ROI. The center of the cell was corrected by again taking the averaging coordinates of pixels above the set threshold within the 70 × 70 pixel region to eliminate any influence of pixel noise within the full frame. The corrected cell center ($x_{c,1}$; $y_{c,1}$) was then calculated for every frame of the 10,000 frame experiment ($x_{c,1}$–$x_{c,10,000}$; $y_{c,1}$–$y_{c,10,000}$). The x and y displacement

(x_d; y_d) were calculated for each frame as the difference from $x_{c,1}$ and $y_{c,1}$. The x_d and y_d were then plotted over time.

Statistical methods

Paired and unpaired student's *t*-tests were performed using GraphPad Prism (version 6.04 for Windows, GraphPad Software, San Diego California, USA, www.graphpad.com).

2.4.8 Additional information

Nicholas C. Flytzanis & Claire N. Bedbrook

These authors contributed equally to this work.

Acknowledgements

We thank the entire Gradinaru lab for helpful discussions. We also thank Prof. David Anderson for helpful discussions and suggestions; Dr. Benjamin Judkewitz for valuable input on the optical setup for imaging; Bin Yang for assistance with optical setup and cultured neurons; Christopher Cronin and Ravi Nath for assistance with *C. elegans* experiments; and Dr. John Bedbrook and Dr. Jennifer Treweek for critical reading of the manuscript. This work was funded by the NIH/NINDS New Innovator (NIH IDP20D017782-01); startup funds from the President and Provost of California Institute of Technology and the Biology and Biological Engineering Division of California Institute of Technology; the Beckman Institute of Caltech; the Gordon and Betty Moore Foundation through Grant GBMF2809 to the Caltech Programmable Molecular Technology Initiative (to V.G.); by NIH 1R21MH103824-01 (to V.G. and F.H.A.); and by the Institute for Collaborative Biotechnologies through grant W911NF-09-0001 from the U.S. Army Research Office (to F.H.A.). The content of the information does not necessarily reflect the position or the policy of the Government, and no official endorsement should be inferred. V.G. is also supported by Human Frontiers in Science Program, the Mallinckrodt Foundation, the Pew Charitable Trust, the Michael J. Fox Foundation, the Kimmel Foundation, Caltech-GIST, NIH 1R01NS085910-01, NIH 1R01AG047664-01. P.W.S. is an investigator with the HHMI, which supported this research. N.C.F., C.N.B. and K.Y.C. acknowledge support from the Caltech Biology Division Training grant (NIH/NRSA 5T32GM07616). M.K.M.E.

acknowledges support from the German Research Foundation (DFG) under programme EN 957/1-1.

Affiliations

Division of Biology and Biological Engineering, California Institute of Technology, Pasadena, California 91125, USA

Nicholas C. Flytzanis, Claire N. Bedbrook, Hui Chiu, Cheng Xiao, Ken Y. Chan, Paul W. Sternberg, Frances H. Arnold & Viviana Gradinaru

Division of Chemistry and Chemical Engineering, California Institute of Technology, Pasadena, California 91125, USA

Martin K. M. Engqvist & Frances H. Arnold

Contributions

N.C.F., M.K.M.E., F.H.A. and V.G. conceived the project. N.C.F., C.N.B., H.C., P.S.W. and V.G. designed the experiments. N.C.F., C.N.B., H.C., C.X. and K.Y.C. performed the experiments. N.C.F. and C.N.B. analyzed all the data. N.C.F., C.N.B. and V.G. wrote the manuscript with support from all authors. V.G. supervised all aspects of the work.

Competing interests

The authors declare no competing financial interests.

Chapter 3

WHOLE-BODY TISSUE CLEARING FOR HIGH-RESOLUTION PHENOTYPING OF INTACT TISSUES

[1] Ezin, M.*, Flytzanis, N. C.* et al. “Bringing CLARITY to the classics: embryonic neural crest contribution in 3D”. *In preparation*.
[4] Treweek, J. B. et al. (2015). “Whole-body tissue stabilization and selective extractions via tissue-hydrogel hybrids for high-resolution intact circuit mapping and phenotyping”. In: *Nature Protocols* 10(11), pp. 1860-1896. doi: 10.1038/nprot.2015.122.

3.1 Summary

To facilitate fine-scale phenotyping of whole specimens, we describe here a set of tissue fixation-embedding, detergent-clearing, and staining protocols that can be used to transform excised organs and whole organisms into optically transparent samples within 1-2 weeks without compromising their cellular architecture or endogenous fluorescence. PACT (passive CLARITY technique) uses tissue-hydrogel hybrids to stabilize tissue biomolecules during selective lipid extraction, resulting in enhanced clearing efficiency and sample integrity. Furthermore, the macromolecule permeability of PACT-processed tissue hybrids supports the diffusion of immunolabels throughout intact tissue, whereas RIMS (refractive index matching solution) grants high-resolution imaging at depth by further reducing light scattering in cleared and uncleared samples alike. These methods are adaptable to all tissues, from thick slices of individual organs to entire organisms. Together, these protocols and solutions enable phenotyping of subcellular components and tracing cellular connectivity in intact biological networks.

Traditional experiments determining neural crest contributions in vertebrate embryos were performed with quail-chick grafts. Aside from the inadequacy of quail progenitors to correctly model the migrating chick neural crest due to species differences, these experiments also require tissue sectioning and staining, which can lead to populations of cells in distal locations being missed. Utilizing tissue clearing technologies optimized for use in amniote embryos, we can inspect lineage contributions in the whole, intact embryo, allowing a high resolution, three-dimensional representation of neural crest contribution throughout the

periphery. Grafts from the neural fold of GFP transgenic donor chickens were implanted into wild-type hosts and analyzed after up to six days of development. By coupling perfusion to remove autofluorescence, tissue clearing of the whole-mount embryo, and staining with antibodies or processing for fluorescent *in situ* hybridization (FISH), neural crest derivatives can be fully explored and characterized. The results reveal a surprisingly diverse array of cell types developing from the cardiac neural crest that contribute to the heart and outflow tract, as classically observed, but also to the enteric nervous system of the esophagus, Schwann cells along cranial nerves, pigment cells, and portions of cranial ganglia.

3.2 Developing passive clarity techniques for diverse tissue types

[4] Treweek, J. B. et al. (2015). "Whole-body tissue stabilization and selective extractions via tissue-hydrogel hybrids for high-resolution intact circuit mapping and phenotyping". In: *Nature Protocols* 10(11), pp. 1860-1896. doi: 10.1038/nprot.2015.122.

3.2.1 Characterizing hydrogel composition and buffer conditions on tissue structure, protein loss and antibody penetration

For selecting the parameters of one's tissue clearing experiment, multiple factors need to be considered, such as tissue size and density, lipid content, retention of macromolecules, clearing time, and others. To fully understand the effect of the tissue clearing process on experimental outcome, I characterized an array of parameters for the various steps of the procedure.

In unstabilized tissue, the prolonged incubation in detergent at 37 °C required for PACT and the perfusive force used in PARS would be detrimental to tissue integrity. Thus, the hybridization of amine-containing and PFA-cross-linked biomolecules to a hydrogel scaffold serves to stabilize tissue architecture and nonlipid content throughout all aspects of PACT and PARS tissue processing. During PARS, the rodent's intact connective tissue and inflexible skeleton provide an additional degree of structural support. To support rapid delipidation in the absence of potentially tissue damaging electrophoretic clearing (ETC)[75], the composition of the PARS/PACT[15] hydrogel monomer solution bares a few major changes from our originally proposed CLARITY hydrogel[14], which consisted of 4% (wt/vol) acrylamide, 4% (wt/vol) PFA and 0.05% (wt/vol) bis-acrylamide (A4P4B0.05). First, the

cross-linker bis-acrylamide must be excluded from the PARS hydrogel formulation to prevent hydrogel blockages in vasculature and perfusion lines. Its exclusion from the PACT hydrogel as well, and the reduced exposure of tissues to PFA in both protocols, accelerates clearing and immunolabeling steps. With a final composition of 4% (wt/vol) acrylamide and 0% PFA (A4P0), the resulting minimal polymeric scaffold of the PARS and PACT tissue-hydrogel matrices suffices not only to retain tissue proteins (Fig. 3a and Supplementary Fig. 2) and stabilize tissue macrostructure[15] during clearing, but it also allows SDS micelles to diffuse more freely through tissue for efficient clearing (Figs. 4a; Supplementary Fig. 2c). Similarly, a lower cross-link density ensures that antibodies can better access tissue epitopes during immunolabeling (Fig. 4b–d).

Traditionally, tissue clearing protocols have aimed to render samples transparent via homogenizing the RIs of the various tissue components and matching their RIs with the lens and mounting setup (e.g., glass coverslip interfaces). This has often been accomplished via exchanging the aqueous fraction of tissue (RI ~1.33) with a mounting medium of higher RI, which includes organic solvents such as BABB (RI ~1.53–1.57)[76–78], dibenzyl ether (RI ~1.56)[79,80] , methyl salicylate (RI ~1.52–1.54)[81] and 2,2′thiodiethanol (RI ~1.52)[82]; polyol and saturated sugar solutions such as glycerol (RI ~1.43–1.47)[14], sucrose and fructose (RI ~1.49–1.50)[83]; and amides such as formamide (RI ~1.44)[84] and urea (RI ~1.38)[85,86]. Aside from passive CLARITY[87] and PACT[15], few passive clearing protocols endeavor to alter the chemical composition of tissue, by removing major tissue components from samples so that they become less light-scattering. One notable example is CUBIC[86,88], which also combines the use of passive delipidation and RI matching to achieve transparency. Thus, we sought to compare the level of delipidation that was achieved with PACT-based clearing (A4P0 and A4P4 hydrogels) and CUBIC-based clearing. To examine the efficacy of tissue delipidation, we used transmission electron microscopy (TEM; Fig. 5b). Indeed, as illustrated by membrane permeabilization and extraction, lipid removal was noticed in all conditions, and it was highest in A4P0, in which a high degree of fine structure loss is evident. In contrast, A4P4 tissue, although extracted, still retains enough contrast for identifying fine structural detail, such as membrane-bound organelles and small neurites. With respect to structural preservation, the CUBIC samples are between the two PACT conditions, showing

nearly complete lipid extraction but with some cytoskeletal elements in the axon preserved. Although samples embedded in A4P0 hydrogel showed adequate protein and nucleic acid retention for imaging endogenous fluorescence (Fig. 5c) and detecting myelin-binding proteins (Fig. 5d), if an enhanced level of tissue preservation is desired, it is best to embed samples in a hydrogel with a higher order of tissue cross-linking by including PFA (for example, by adding 1–4% (wt/vol) PFA to the 4% acrylamide hydrogel solution, termed A4P1-4). Alternatively, samples can be processed in parallel, and adjacent areas can be directed either to TEM or to hydrogel-embedding and clearing to obtain both ultrastructural and volume information, respectively.

The denaturing anionic detergent sodium dodecyl sulfate (SDS), used for lipid removal in PACT/PARS, is also very effective in dissociating DNA from proteins (e.g., for cell nuclei removal) and in disrupting extracellular matrices to facilitate protein removal (e.g., ionic interactions of SDS with membrane proteins allow for their removal and purification). For example, retrograde perfusion of a cadaveric rat heart with 1% (wt/vol) SDS for 12 h results in its complete decellularization[89]. By contrast, SDS solubilization of lipid bilayers via a micellar mechanism is a slower process. Thus, to guard against the extraction of peptide and nucleic acid content during SDS clearing, it is important that nonlipid tissue components have been hybridized to a hydrogel scaffold.

In the initial *Nature* paper describing CLARITY[14], the dense tissue-hydrogel cross-linking conferred by A4P4B0.05 tissue embedding prohibited rapid passive clearing of large tissue blocks[75]. The advanced CLARITY protocol[87] suggests decreasing acrylamide concentrations to as low as 0.5% (A0.5P4B0.0125) when clearing is performed passively rather than with ETC-based rate enhancement. After the initial, thorough perfusion-fixation step with 4% PFA, PACT and PARS tissues are infused with A4P0 monomer[15]. Although bis-acrylamide may be included in the hydrogel formulation to stabilize fragile samples, we have not found the addition of bis-acrylamide to be beneficial in preventing protein loss (Fig. 3a) in either A4P0-hybridized (A4P0B0.05) or A4P4-hybridized (A4P4B0.05) tissues. Furthermore, although protein retention is similar for all A4P0-4 formulations (Fig. 3a), higher concentrations of PFA, which anchors tissue to the hydrogel mesh and increases tissue cross-linking, result in enhanced fine structure preservation (Fig. 5b) and limit anisotropic

tissue-hydrogel expansion (Fig. 3b,c). The resulting less-porous tissue-hydrogel matrix curtails protein solubilization by SDS (Fig. 3a and Supplementary Fig. 2b); clearing speed (Fig. 4a and Supplementary Fig. 2c), overall tissue transparency (Fig. 4a), and the efficiency of antibody labeling (Fig. 4b–d) are all reduced. Thus, PFA-containing hydrogel formulations are only recommended for samples that will be used for in-depth profiling of fine structures, in which protein and nucleic acid retention is of maximum importance.

Most protocols that render tissues transparent cause notable sample volume fluctuations. In general, clearing protocols that entail dehydration steps for clearing with organic solvents or some concentrated RI-matching solutions cause tissue shrinkage, whereas protocols that involve prolonged incubations in aqueous detergent-based solutions tend to cause gradual tissue expansion[83,85,90]. In part a consequence of the water-absorbing properties of polyacrylamide, a nitrogen-containing derivative of the super-absorber polyacrylic acid, tissue-hydrogel expansion has previously been reported with CLARITY and PACT-processing[14,15] (Fig. 3b,c), and indeed it has been used to great advantage in ExM[91]. Several factors have been shown to influence the swelling properties of water-absorbing hydrogels. The most notable are pH; the dissolved ion content of the aqueous swelling medium (i.e., clearing buffer) and the tissue-hydrogel microstructure, including the ordering of monomeric units within a polymerized hydrogel; the degree of cross-linking; and the mechanical rigidity of the embedded tissue. With respect to tissue clearing, as detergent gradually solubilizes and extracts tissue biomacromolecules, not only can water migrate into this additional space in the tissue-hydrogel matrix, but also there is less mechanical resistance from tissue components to polymer swelling as water continues to diffuse in. A modification to passive CLARITY-based protocols in order to counteract tissue expansion that occurs during clearing and to minimize the occurrence of morphological artifacts that could be introduced with fluctuating tissue size is by performing PACT with a hydrogel monomer formulation that contains increasing amounts of PFA (e.g., a hydrogel solution of 4% (wt/vol) acrylamide and 1–4% (wt/vol) PFA, A4P1–4)). The inclusion of PFA in hydrogel monomer compositions not only combats hydrogel swelling but also the expansion becomes increasingly isotropic (Fig. 3b). Thus, for improved tissue preservation, it is advisable to supplement the A4P0 hydrogel recipe with PFA (1–4% PFA in the monomer solution).

The inclusion of PFA in monomer solutions also curtails tissue size changes in mounting medium. Upon their initial immersion in RIMS, tissue samples contract during the first hour (~20% for A4P0-embedded coronal rodent brain sections), followed by a gradual rebound back to their pre-RIMS size. Imaging during this time window should be avoided, as these slight size fluctuations could introduce apparent tissue deformities or sample drift issues during image acquisition. With adequate equilibration in RIMS (e.g., hours to days, depending on sample size, tissue permeability, and so on), sample size and transparency will reach a steady state for high-resolution, deep imaging[15].

3.2.2 Main figures

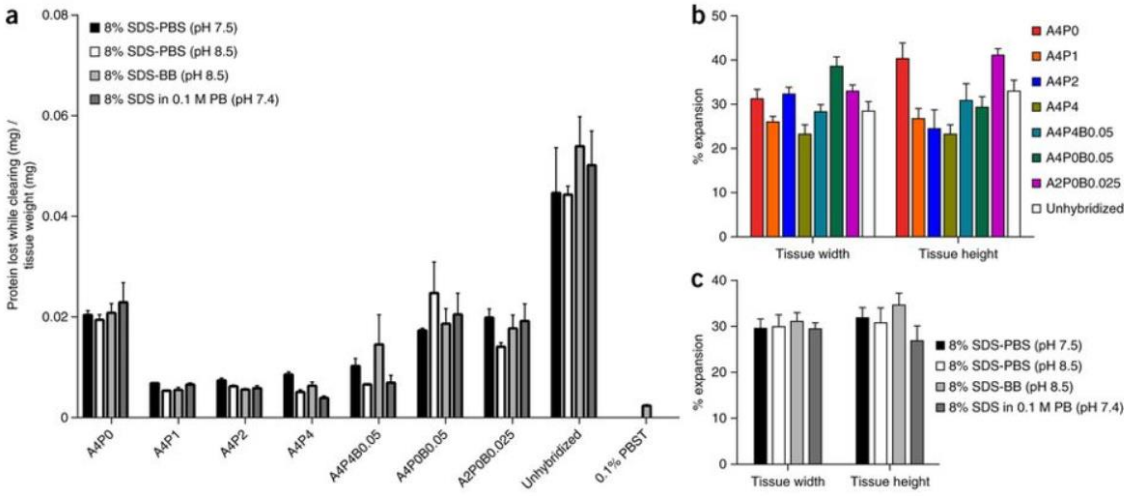

Figure 3: PACT protein loss and tissue expansion for different hydrogel and clearing conditions. A detailed comparison of the protein loss and tissue expansion for eight different hydrogel matrix compositions: A4P0, A4P1, A4P2, A4P4, A4P0B0.05, A4P4B0.05, A2P0B0.025 and unhybridized, and four different clearing buffers: 8% SDS-PBS (pH 7.5), 8% SDS-PBS (pH 8.5), 8% SDS-BB (pH 8.5) and 8% SDS in 0.1 M PB (pH 7.4). Perfused and fixed mouse brains were sliced into 1-mm-thick coronal slices, and combinations of all the different hydrogel and clearing conditions were performed on slices from comparable locations. Slices were monitored and imaged every 12 h, and the clearing buffer was collected for protein loss measurements and replaced. (**a**) Total protein content within each sample of clearing buffer collected throughout the clearing process was measured by the bicinchoninic acid assay by extrapolating the concentration of protein from a standard curve of BSA concentration in each clearing buffer (Supplementary Fig. 2a). Protein amounts from each time point were summed until each slice was completely clear, resulting in a measure for the total amount of protein lost while clearing for each slice. This total protein loss was then compared with the initial weight of each slice ($n = 3$). A comparison was also made with the protein loss of 100-μm-thick slices that were not cleared but were permeabilized with

PBST overnight (n = 9). (**b**) Comparison between total width and height tissue expansion between hydrogel compositions (n = 4). (**c**) Tissue expansion comparisons with different clearing conditions (n = 8). (**a**–**c**) Data are presented as mean ± s.e.m. Experiments on vertebrates conformed to all relevant governmental and institutional regulations, and they were approved by the Institutional Animal Care and Use Committee (IACUC) and by the Office of Laboratory Animal Resources at the California Institute of Technology.

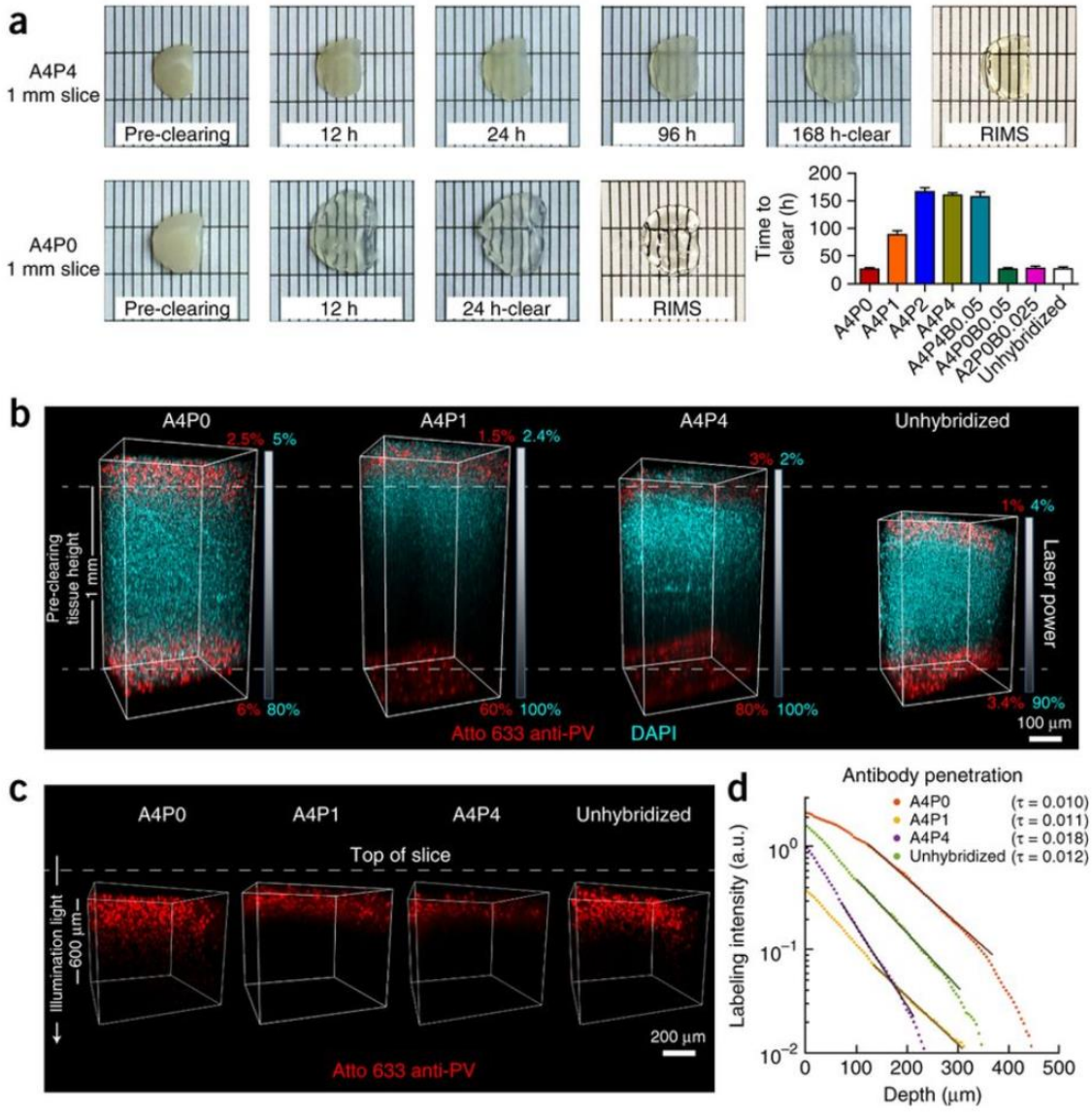

Figure 4: Clearing time course and antibody penetration of PACT-processed samples. Quantitative comparison of the effect of different hydrogel-embedding conditions and clearing buffers on time to clear and antibody penetration during immunostaining. 1-mm-thick mouse coronal slices were hybridized and cleared with the array of previously used PACT conditions (Fig. 3). Slices were monitored for the time they took to become

transparent. Once cleared, slices were washed and then immunostained. (**a**) Representative images of two 1-mm-thick coronal brain slices (~1.0–0.0 mm anterior to bregma) through the time course for PACT clearing and a comparison of time to clear (mean ± s.e.m.) for each PACT hydrogel composition. For the representative images, slices were cleared with 8% SDS-PBS (pH 8.5) and incubated in RIMS for 24 h. (**b**) Imaging of antibody penetration through different PACT tissue preparations. Previously cleared and washed 1-mm-thick slices were immunostained for parvalbumin (red) and nuclei stained with DAPI (cyan), using 2-d incubations with the primary and Fab format secondary antibodies, transferred to RIMS for 5 h and then RIMS-mounted. Samples from the cortex, traversing the depth of the slice, were imaged on a Zeiss LSM 780 confocal microscope with a Plan-Apochromat 10× 0.45 NA M27 air objective (w.d. 2.0 mm). To ensure even illumination throughout the depth of the slice for fair antibody detection, we applied laser power *z*-correction (Zen software, Zeiss): power was changed linearly for each slice, shown as a gradient next to each image; starting power values at the top were chosen to match the level of fluorescence at the surface across slices, whereas the range of powers varied for different PACT conditions. Shown are images of staining through A4P0, A4P1 and A4P4 hydrogel-embedded samples, as well as unhybridized tissue, cleared with 8% SDS-PBS (pH 7.5). As antibody and small-molecule dye diffused through both the top and bottom surfaces of the slice simultaneously, the images show that within 2 d DAPI has fully penetrated in all the conditions, whereas antibody labeling has progressed to varying extents, depending on the PACT condition. As slices cleared with the different conditions also swell to different extents during the process (indicated by their difference in height relative to the pre-clearing height of 1 mm, as indicated by the white dotted lines in **b**, penetration of antibody through a more swollen sample will either require longer diffusion time or faster diffusion rate to reach an equivalent anatomical depth as in a less swollen sample. Incomplete detection of the DAPI signal in A4P1 and A4P4 slices is due to the difficulty of achieving similar light penetration in highly cross-linked slices. (**c**) Depiction of parvalbumin staining through same slices as in **b**. DAPI signal has been removed to better show the variable penetration of the antibody over the course of a 2-d period. (**d**) Quantification of antibody penetration through PACT conditions depicted in **b** and **c**. Antibody fluorescence signal was scaled by the average DAPI intensity for each *z*-section inside the volume, and the average scaled fluorescence along a line perpendicular to the tissue surface produced a final estimate of labeling intensity (in arbitrary units, a.u.) as a function of tissue depth. Antibody diffusion was fit to an exponential model [$f(x) = a \times \exp(-\text{tau} \times x) + b$], with the exponent tau being inversely proportional to the square root of the diffusivity, wherein a larger tau indicates slower diffusion. Labeling intensities for A4P0, A4P1, A4P4 and unhybridized samples cleared with 8% SDS-PBS (pH 7.5), as a representative sample of all the different buffers, are plotted on a logarithmic scale. The amount of PFA contained in the hydrogel-tissue matrix is inversely proportional to immunohistochemical staining efficiency. Experiments on vertebrates conformed to all relevant governmental and institutional regulations, and they were approved by the Institutional Animal Care and Use Committee (IACUC) and by the Office of Laboratory Animal Resources at the California Institute of Technology.

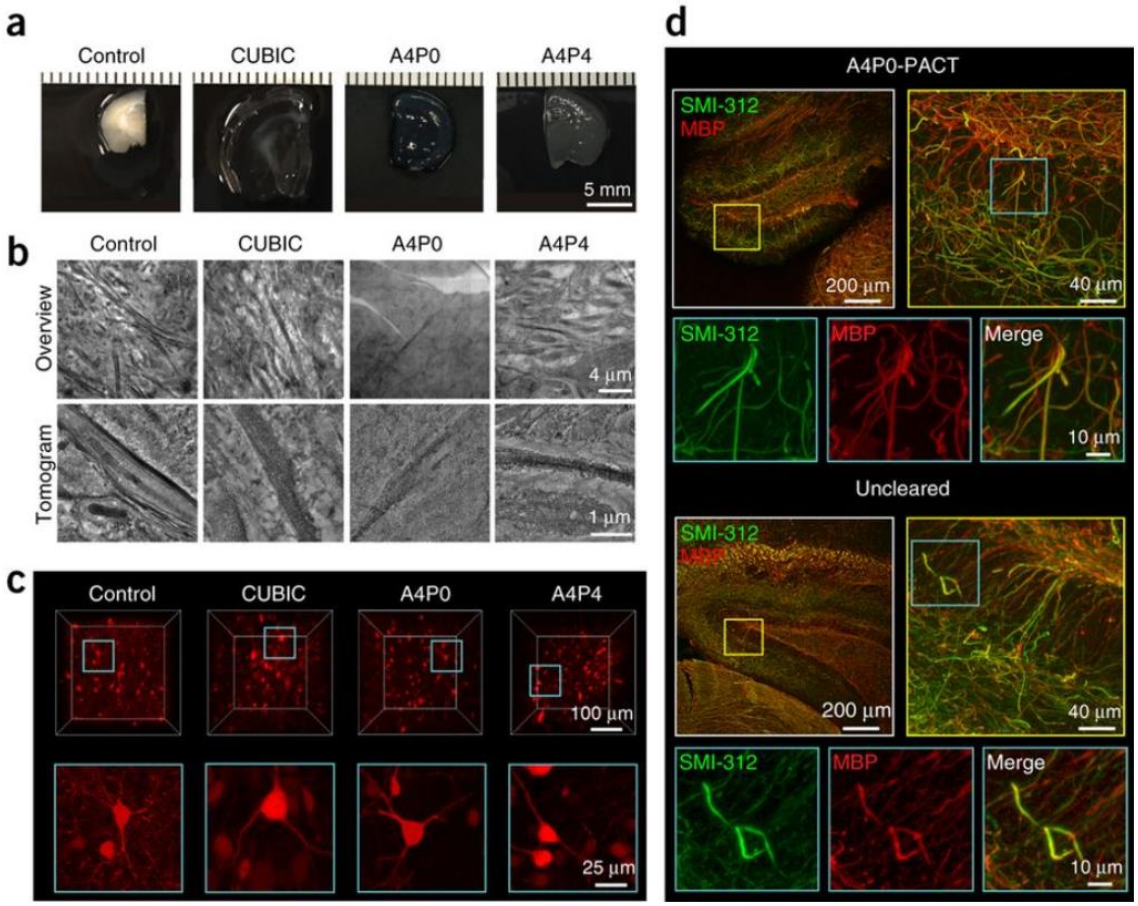

Figure 5: Preservation of tissue architecture during delipidation. The differential effects of individual clearing conditions on cellular architecture and endogenous and stained fluorescence imaging. (**a–c**) Mice that received bilateral intracranial injections in the lateral septum of AAV expressing the tdTomato transgene were perfusion-fixed with 4% PFA, and a subset of 1-mm-thick unhybridized coronal brain sections were prepared for microscopy without clearing (control, first column), or they were first rendered transparent via the CUBIC method[86,88] (second column). The second subset of 1-mm-thick sections underwent PACT-processing: A4P0 embedding (third column) or A4P4 embedding (fourth column) and clearing with 8% SDS-PBS (pH 7.5), followed by preparation for ultrastructural study or RIMS mounting. (**a**) Brain sections were photographed after fixation (control) or immediately after clearing (CUBIC, A4P0 and A4P4) to illustrate the degree of tissue swelling that occurred for each condition. (**b**) Control (unhybridized, uncleared), CUBIC-cleared and PACT-cleared (A4P0, A4P4) tissues were then processed identically for ultrastructural examination using electron microscopy and tomography. Overviews (top row) from each of the four samples illustrate the relative amount of lipid loss attributable to the different clearing methods, in terms of contrast between structures. Tomographic reconstruction (bottom row) of subregions of the overviews, each showing a portion of an axon and surrounding cellular structures, indicates the extent of change at the fine-structural level. (**c**) Control, PACT- and CUBIC-cleared brain sections were mounted in RIMS or

CUBIC reagent-2[86,88], respectively, and the endogenous expression of tdTomato was imaged on a Zeiss LSM 780 confocal microscope with the LD LCI Plan-Apochromat 25× 0.8 NA Imm Corr DIC M27 multi-immersion objective (w.d. 0.57 mm). Volume renderings (top: x,y,z = 300 μm for PACT- and CUBIC-cleared samples and x,y,z = 300, 300, 140 μm for control) and maximum intensity projections (bottom: x,y,z = 100,100,50 μm) are shown. In all images except the uncleared control, cells are visualized throughout the volume imaged. In the control image, light is unable to penetrate through the sample to image at depth. (**d**) Preservation of myelin proteins. 200-μm-thick A4P0-PACT-cleared mouse brain sections and 50-μm-thick uncleared sections were immunostained for SMI-312 and for myelin basic protein (MBP), using Atto 488–conjugated and Atto 647N–conjugated Fab format secondaries. After a 2-h RIMS incubation, the transparent sections were mounted and imaged on a Zeiss LSM 780 confocal microscope with the Plan-Apochromat 10× 0.45 NA M27 air objective (w.d. 2.0 mm) and the LD LCI Plan-Apochromat 25× 0.8 NA Imm Corr DIC M27 multi-immersion objective (w.d. 0.57 mm). The images correspond to a 50-μm-thick maximum intensity projection over the dentate gyrus; Top: A4P0-PACT cleared, Bottom: uncleared smaller panels are high-magnification images of the boxed areas showing myelinated axons. Experiments on vertebrates conformed to all relevant governmental and institutional regulations, and they were approved by the Institutional Animal Care and Use Committee (IACUC) and by the Office of Laboratory Animal Resources at the California Institute of Technology.

3.2.3 Supplementary figures

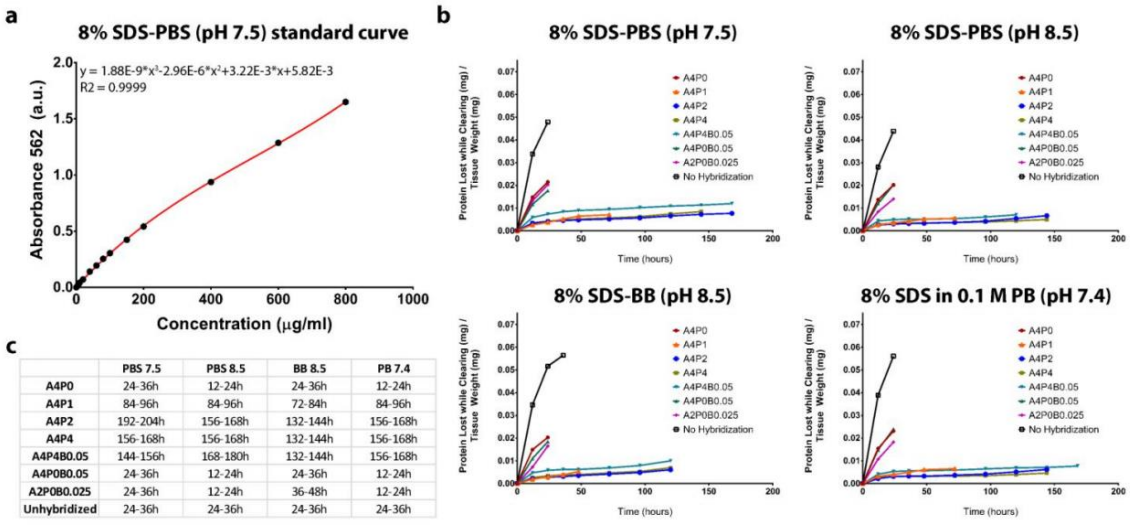

c

	PBS 7.5	PBS 8.5	BB 8.5	PB 7.4
A4P0	24-36h	12-24h	24-36h	12-24h
A4P1	84-96h	84-96h	72-84h	84-96h
A4P2	192-204h	156-168h	132-144h	156-168h
A4P4	156-168h	156-168h	132-144h	156-168h
A4P4B0.05	144-156h	168-180h	132-144h	156-168h
A4P0B0.05	24-36h	12-24h	24-36h	12-24h
A2P0B0.025	24-36h	12-24h	36-48h	12-24h
Unhybridized	24-36h	24-36h	24-36h	24-36h

Supplementary Figure 2. Protein loss over the course of PACT clearing. The amount of protein lost while clearing was measured by performing a BCA on the clearing buffer, which was collected and replaced periodically while 1 mm tissue samples were undergoing PACT. A standard curve of BSA protein concentration in each of the four different clearing buffers was generated. Standard curves were fit with a third order polynomial and used to extrapolate all protein loss measurements. (a) A representative case, in which the absorbance in arbitrary units (a.u.) of standard solutions at 562 nm is plotted against known BSA concentrations in

8% SDS-PBS (pH 7.5). (b) Graphs show single-trial, representative protein loss measurements for each hydrogel condition in each clearing buffer. Protein content was measured at 12 hours into clearing, at 24 hours, and then every 24 hours until the samples were clear and normalized to the initial weight of the slice. Experiments were performed in triplicates, representative single trials for each combination are shown. (c) Time to clear for 1 mm sections PACT-processed with all hydrogel embedding and clearing buffer combinations (n = 3 for A4P1, A4P2 and Unhybridized. n = 4 for all others).

3.3 Visualizing neural crest development in cleared chicken embryos

[1] Ezin, M.*, Flytzanis, N. C.* et al. "Bringing CLARITY to the classics: embryonic neural crest contribution in 3D". *In preparation*.

3.3.1 Applying passive tissue clearing to chicken embryos

Chicken embryos are a heterogenous tissue, requiring adaptation of the traditional tissue clearing parameters to combat variable lipid content and tissue density. To overcome these two problems, we adapted and optimized the previously published PACT conditions[15,16], allowing us to fully clear E6 embryos in four days (Fig. 1a). The first, and largest, modification was to perform tissue clearing with the help of convective flow (Fig. 1b), instead of relying on passive diffusion, which may have taken up to a month[16]. Second was to reduce the concentration of SDS while clearing to 4%, down from the 8% traditionally used by PACT, to account for the diversity in tissue types within the embryo. While this resulted in a reduction of clearing time, it helped to ensure more homogenous clearing, with the differences in clearing time and anisotropic expansion between lighter and denser tissues being removed. The rest of the clearing parameters were kept consistent with previously published[16]: embryos were fixed with 4% paraformaldehyde in PBS at 4^{o}C for 48 hours, stabilized by embedding into a tissue-hydrogel matrix (4% acrylamide in PBS) and then cleared. After progressive clearing over 4 days, refractive index matching was enabled by mounting in RIMS, and embryos were imaged.

An additional problem we encountered while clearing whole embryos was the presence of blood cells trapped by fixation within the embryo, and the excessive autofluorescence generated by these while imaging. To circumvent this problem, we adapted an established mammalian placental perfusion technique[92] for use in chicken embryos (Fig. 1c). Briefly, the embryonic vasculature was accessed by making a small incision in the

umbilical blood vessel[93] of the embryo, while still inside the egg, through which a microcatheter was inserted. Saline was perfused through the embryonic vasculature using a micro-peristaltic pump at an infusion rate of 5 µl/min. In some cases, the embryo was further perfused via direct cannulation of the carotid artery. Following exsanguination, the embryos were rapidly fixed *in situ* via perfusion of 4% PFA. This procedure resulted in a drastic reduction in autofluorescence in highly vascularized areas of the embryo, compared with un-perfused embryos (Fig. 1d), with the added benefit of more thoroughly fixing the tissue, due to active dissemination of PFA compared to passive diffusion.

3.3.2 Whole-mount immunohistochemistry and FISH

A major strength of tissue clearing via PACT is its ability to retain endogenous fluorescence of samples coupled with its compatibility with a variety of labeling techniques[16]. To test our ability to do a phenotypic characterization of cell-types within an intact, cleared embryo, three- and six-day old chick embryos were stained with several antibodies followed by refractive index matching and imaging using traditional confocal and light sheet microscopy. We focused on neuronal populations, labeling with antibodies against HuC/D (Fig. 2a) and Tuj1 (Fig. 2b), achieving embryo-wide labeling after two weeks combined of primary and secondary staining. In addition to antibody staining, we sought to determine if PACT processed embryos could be processed by *in situ* hybridization, which greatly increases the number of factors that can be identified simultaneously and is performed in a fraction of the time. To this end, we tested whether hybridization chain reaction (HCR)[94] could be applied to chick embryos after passive clearing. We processed transgenic GFP embryos in which all cells are GFP positive and stained them using probes against the transcription factor Sox10, which marks neural crest cells and their derivatives. The results review robust double staining of dorsal root ganglia in six-day old transgenic GFP chicks that are also brightly GFP positive (Fig. 2c,d).

3.3.3 Tracking cardiac crest derivatives

One of the most specialized neural crest contributions is the cardiac neural crest, which arises from the hindbrain just caudal to the otic vesicle and adjacent to the first three

somites. Quail/chick chimera by Kirby and colleagues[95] showed that these cells contribute to the aortic arches, cardiac outflow tract and septum, as well as the valves of the heart. Given that these experiments were analyzed by sectioning and staining the region of the embryos encompassing the heart and outflow tract of the chimeric embryos, we sought to get a three-dimensional view of cardiac crest contributions. We performed GFP grafts of GFP-labeled dorsal neural folds adjacent to the mid-otic to somite 3 level from 9-10 somite stage donor embryos and grafted these in place of the homologous region of wild-type neural folds of similarly staged embryos (Fig. 3a). Embryos (n=6) were then allowed to survive until embryonic day 6, by which time the four-chambered heart had formed. Embryos were perfused and cleared as described above and then imaged for GFP labeling (Fig.3b).

As expected, several mesenchymal derivates arose from the GFP-labeled cardiac neural crest. In the heart, we noted bright GFP signal in the aortic arch arteries[19,96] and in the outflow tract[96,97]. Specifically relating to the outflow tract, we found that the aorta, pulmonary trunk and aorticopulmonary septum were seeded with GFP-labeled cells in almost all embryos (Fig. 3c). Cardiac neural crest has also been shown to invade endocardial cushions and help form valves, notable among these the aortic semilunar valve[98]. Such contributions were also seen in our cleared embryos (Fig. 3c). The pharynx, clearly labeled by GFP (Fig. 3c), is another structure seeded by the cardiac neural crest[19], and as the buccal aspect of an embryo, will mature to function as part of both the respiratory and digestive systems. Cardiac neural crest cells are also known to help form other heart structures like the interventricular septum and the cardiac ganglia[95,98,99], as well as the endocrine glands of the thymus[19], parathyroids[19] and thyroid[100], and mechano- and chemoreceptors like the baroreceptors and carotid bodies[19]. These derivates arise at more advanced stages than we collected here and were therefore not observed in our work.

In addition to mesenchymal derivatives, the neural crest gives rise to neuronal and glial cells of the entire peripheral nervous system, as well as pigment cells. The cardiac neural crest, in particular, participates in the formation of cranial nerves IX (glossopharyngeal) and X (vagus[101,102]). Both these nerves are in part derived from transgenic GFP grafts and were labeled in multiple embryos (Fig. 3d). Fluorescent cells also often formed the nodose and petrosal ganglia which synapse with the vagus and glossopharyngeal nerves (Fig. 3d). The

jugular and superior ganglia[103], which associate with nerves IX and X, were also labeled. From all axial levels of the embryo, a subpopulation of neural crest cells will become melanocytes[19,104]. Our results corroborated these prior findings in that all embryos displayed melanocytes in their skin (Fig. 3e).

Even though the grafts were small, contributions by GFP-labeled cardiac neural crest cells were noted in several surprisingly anterior locations. The first unexpected result relates to the melanocytic lineage. Cardiac neural crest cells have been reported to give rise to melanocytes that populate the maturing dermis from the level of the otic vesicle to somite 7[19,104]. In some cases, we observed a more rostral extent of crest migration whereby pigment cells invaded the dermis up to the midbrain/hindbrain boundary (Fig. 3e). The second puzzling point deals with the branchial arch arteries. The axial crest origins of all branchial arch arteries have been carefully studied and documented, both spatially and temporally: neural crest participating in the formation of branchial arch arteries 1 and 2 arise in the dorsal neural tube at pre-otic levels, from rhombomeres 1 through 4[105]. Cardiac neural crest cells in one cleared embryo labeled branchial arch artery 2. In this embryo, the full pair of pharyngeal arch arteries 2 (Fig. 3c), located in the anterior section of these derivates, arose from the caudal-most cardiac neural crest from the level of somite 2 to 3. A set of third anterior derivatives was the paired dorsal aorta and carotid arteries past the common carotid branch point. Several embryos showed label in the internal carotid artery (Fig. 3c).

3.3.4 Figures

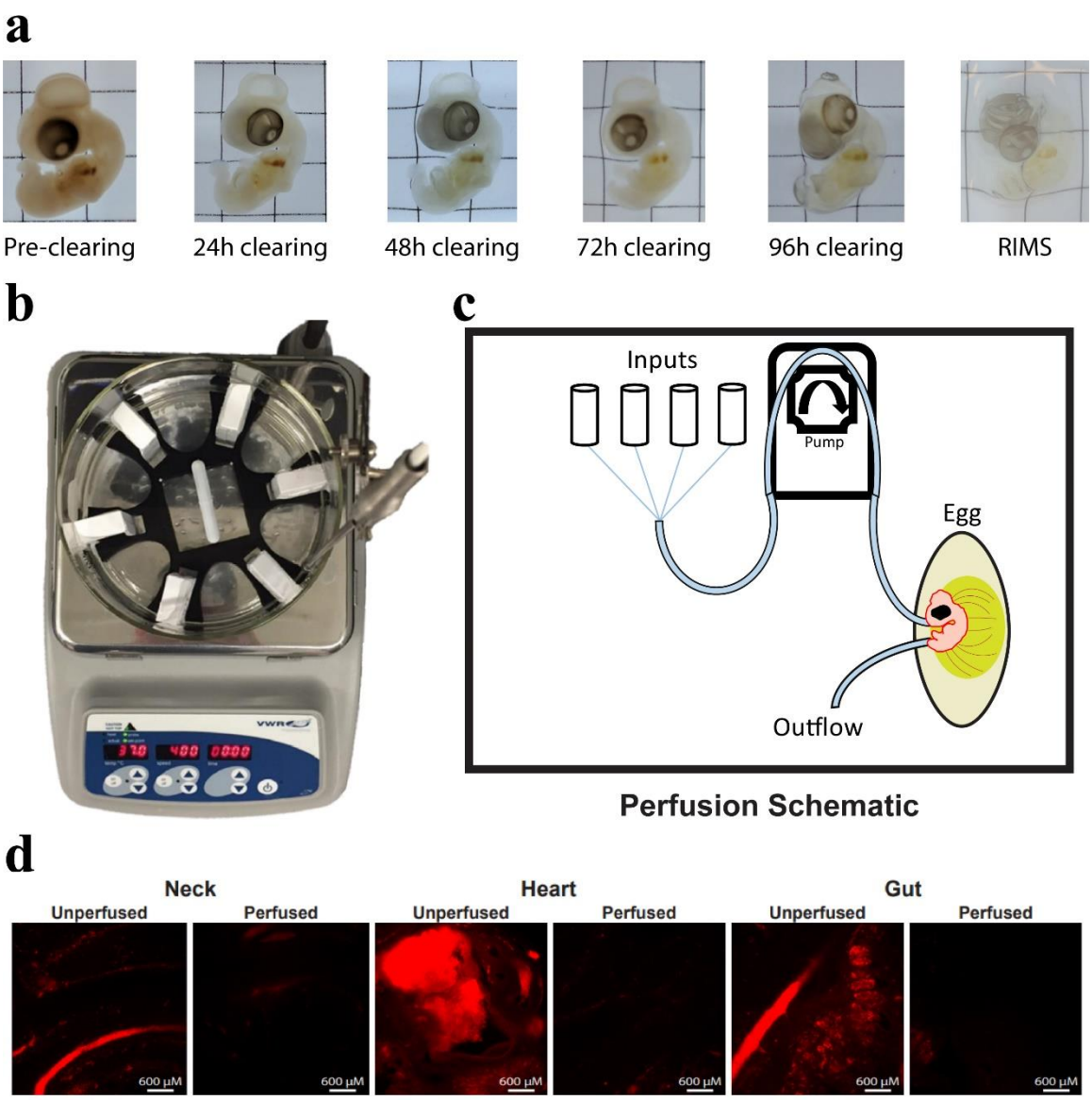

Figure 1. Adapting PACT to chicken embryos. The passive clarity technique is very adaptable to different kinds of tissues and applications. **(a)** for chicken embryos we fixed the tissue in paraformaldehyde, hybridized it to an A4P0 (4% acrylamide in PBS) hydrogel, and progressively cleared it in 4% SDS in PBS with convective flow for 4 days before refractive index matching in RIMS. **(b)** The flow assisted clarity chamber consists of white tissue cassettes housing the embryos, arrayed around the perimeter of a dish kept at a steady 37°C while constant flow is applied via magnetic stir bar. **(c)** The micro-peristaltic pump set up by which embryos are exsanguinated and fixed prior to removal from the egg. An incision is made in the embryo shell and a microcatheter inserted into the umbilical blood vessel or carotid artery. PBS is first flushed through at a rate of 5 µl/min to remove blood, and then

4% PFA for an extended period to fix the embryo well before removal from the egg. **(d)** Representative images of the difference between unperfused and perfused embryos regarding blood autofluorescence. When the embryo is not properly exsanguinated, blood gets trapped and fixed throughout the body, with especially egregious areas being the neck, heart and gut. Side by side images of similar areas of two different embryos are shown.

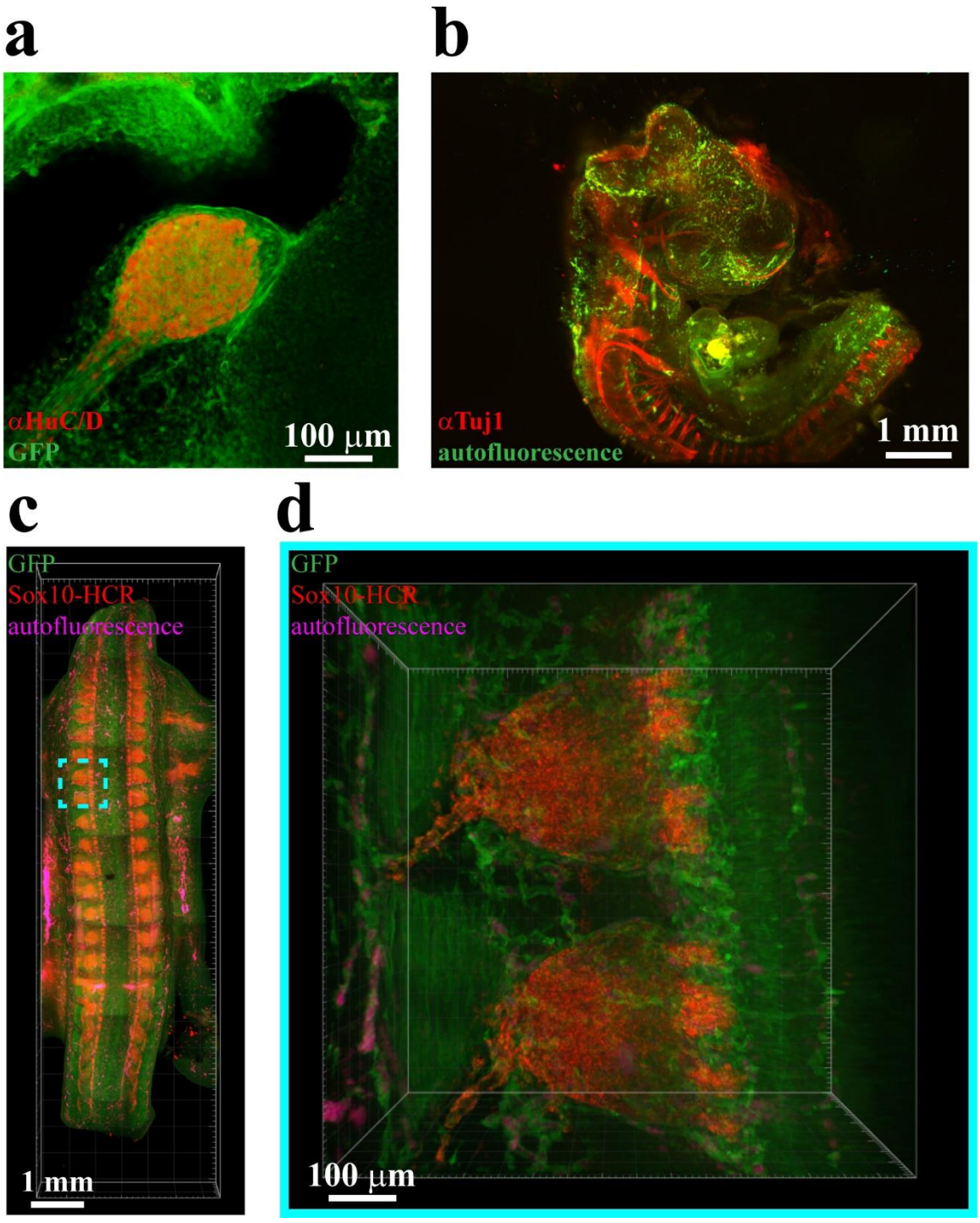

Figure 2. Immunohistochemistry and HCR in cleared chicken embryos. **(a and b)** Briefly, after 4 days of clearing, chicks are stained with primary antibody in PBS for 7 days, washed in 0.1% PBST 3-4 times over the course of two days, stained with secondary antibody in PBS for 7 days, washed another 3-4 times over two days in PBS and then refractive image matched with RIMS for 24 hours before imaging. **(a)** a ganglion labeled with anti-HuC/D primary antibody and Alexa633 secondary in an E6 GFP-transgenic chick. **(b)** whole-body image of an E3 wild-type chick labeled with anti-Tuj1 primary antibody and Alexa633 secondary. **(c and d)** Chicks are labeled using hybridization chain reaction with probes against Sox10 mRNA. Briefly, after 4 days of clearing, chicks are incubated overnight in hybridization buffer (10% dextran sulfate, 10% formamide in 2x SSC) containing paired oligo probes against Sox10, washed in 2x SSC with 30% formamide and then 2x SSC three times each for 30 minutes, incubated in amplification buffer (10% dextran sulfate in 2x SSC) containing Cy3B-coupled hairpins against the oligo probes for six hours at RT, washed three times in 2x SSC for 30 minutes each and then refractive image matched with RIMS for 24 hours before imaging. **c)** Dorsal view of the entire back of a GFP-transgenic embryo. Labeled in red is Sox10 which clearly labels the developing DRGs in this area. **(d)** Close up of two DRGs from **c**.

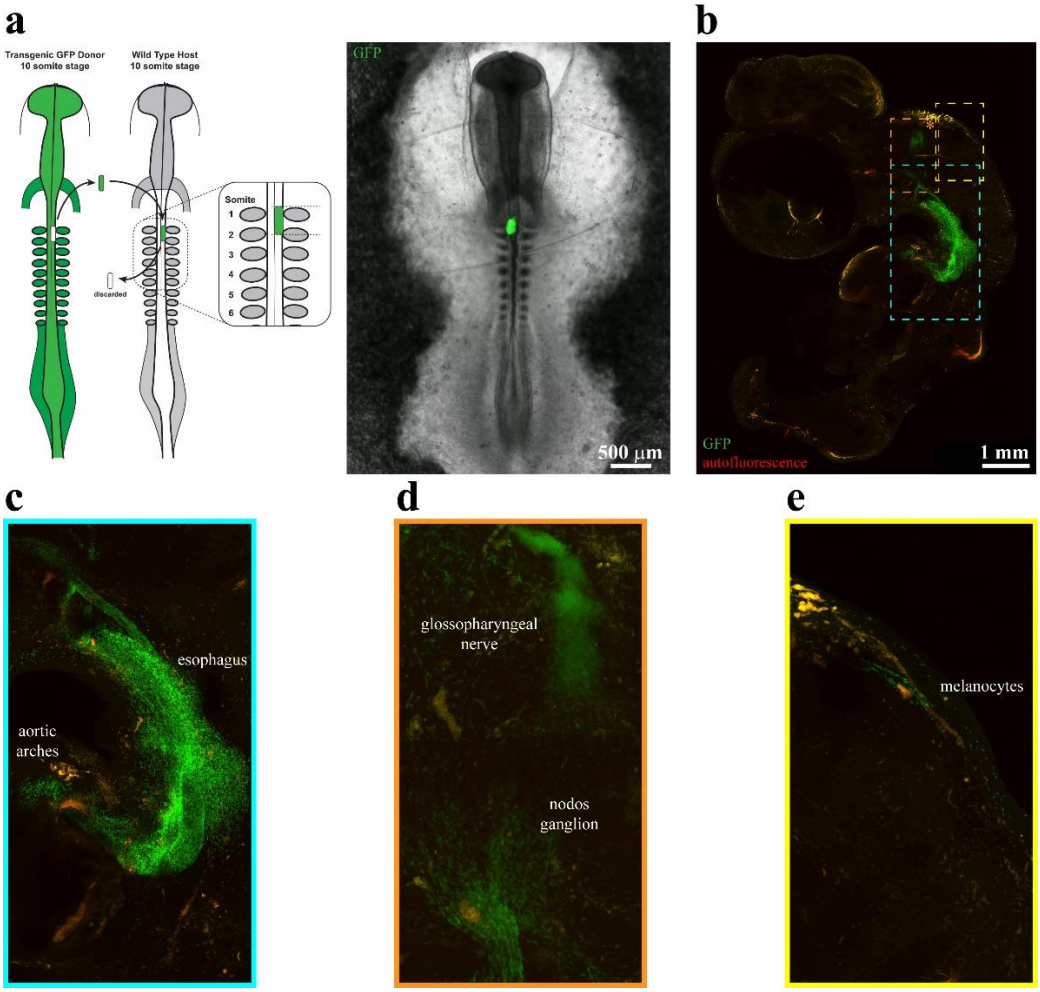

Figure 3. Cardiac neural crest derivatives in cleared chicken embryos. 1.5 somite-long orthotopic and isochronic grafts of GFP-labeled neural fold were made at various locations between somites 0 and 3 (cardiac neural crest) in different HH10 stage chick embryos. **(a)** Left - schematic of neural fold grafts from GFP-transgenic chick embryo into wild-type host. Right – Brightfield and fluorescence image of representative cardiac neural crest graft. **(b)** GFP-labeled cardiac neural crest derivatives throughout various expected and unexpected locations in a cleared E6 chick. ***** Taken from the same location of a different embryo. **(c)** Close-up of cardiac and esophageal region of neural crest derivatives. Expected labeling found in aorta, pulmonary trunk, aorticopulmonary septum, aortic semilunar valve, pharynx. Unexpected labeling found in branchial and pharyngeal arch arteries and paired dorsal aorta and carotid arteries. **(d)** Close-up of cranial nerves IX and X. Expected labeling found in glossopharyngeal and vagus nerves, as well as nodos ganglion. **(e)** Close-up of dermis near midbrain/hindbrain boundary. Expected labeling found in melanocytes, but their location was unexpectedly rostral of where cardiac neural crest derivates are supposed to be found.

3.3.5 Future directions

We speculate that the more anterior cardiac neural crest derivatives we discovered result from convergent extension and anterior shifting of the grafted neural tube. This may occur after most "cardiac" neural crest cells have left the neural tube, but we did see some apparently ganglion-like cells in the periphery at the same level as the labeled neural tube cells, as well as some mesenchymal GFP-labeled cells that are almost certainly melanocytes. As melanocytes are the last cells to migrate from the neural tube in the chick, this may suggest that convergent extension of the graft occurred prior to migration of pigment cells, which occurs at ~HH20-21 in the chick. It will be exciting to see whether less prominent derivatives of the cardiac neural crest can be detected in cleared embryos. Such tissues include the heart's coronary arteries[106,107] and a sparse population of cardiac ganglia cells before they coalesce. Whether the cardiac neural crest gives rise to nerve cells in the esophagus remains an issue under debate – indications from our grafts are that they probably do, at the caudal tip of the pharynx. Answering these questions, as well as further characterizing the derivatives that we have visualized, will require staining and further imaging, experiments currently under way.

Chapter 4

ENGINEERING TISSUE SPECIFIC AAVS FOR GENE THERAPY

[2] Flytzanis, N. C.*, Goeden, N. S.*, Deverman, B. E., Gradinaru, V. "Engineering tissue-specific AAVs for gene therapy". *In preparation*.

4.1 Summary

AAVs see widespread use for gene therapy as well as basic science applications. Their mostly conserved structure but diverse functionality presents an interesting problem for protein engineering. Specifically, directing systemically administered viruses toward distinct tissues allows for specialized treatment of target cells/organs, avoiding side-effects. Our efforts were two-fold: 1) engineer AAV9 to preferentially target specific tissues, and 2) further engineer PHP.eB, a variant of AAV9 previously engineered to efficiently cross the blood-brain barrier and transduce brain cells, to de-target it from all other regions of the body except the brain. To this end, we created a seven amino acid substitution library at the furthest surface-exposed loop (amino acids 452-458) and inserted it into both AAV9 and PHP.eB. After two rounds of Cre-dependent selection of our library *in vivo* in a panel of transgenic mice expressing Cre-recombinase in a variety of cell-types, we tested a variety of AAVs that targeted cells/organs of therapeutic significance. Coming out of the AAV9 substitution library, AAV9.RWT4 shows biased transduction to the lungs, an almost 5-fold increase over AAV9. From the PHP.eB substitution library, we discovered a variant, AAV9.ReB10, that targets the brain just as strongly as its parent, with a strong preference for neurons over any other cell type, while being almost fully de-targeted (~10-100-fold decrease) from all peripheral organs. Combined, these two variants present strong examples of the power of engineering AAVs for cell-type and organ specificity, as well as a strong foundation for further work developing tools for gene therapy.

4.2 Cre-dependent positive and negative selection of AAV9 libraries

An outstanding challenge for gene therapy is the means to safely and efficiently transfer large genomes exclusively to desired cells and organs. Thus, our engineering

efforts focus on selecting viruses that specifically transduce one tissue over the others. To this end, we utilize an updated version of the CREATE methodology developed by Deverman and colleagues[29] (Fig. 1a). With CREATE, a library of AAV capsids with mutations at a specific location is generated by PCR with degenerate primers, viruses packaging a replication-incompetent version of their own genome with a polyadenylation site flanked by Cre/Lox sites are produced in HEK cells, and the viral library is injected into transgenic animals expressing Cre in a specific population of cells. If variants of the library successfully transduce cells expressing Cre, their genome is flipped, and the sequences of those variants can be recovered in a Cre-dependent manner. In our version of CREATE, we utilize a similar strategy for generating libraries but perform selection in multiple transgenic mouse lines expressing Cre in different populations: Tek-Cre for endothelial cells throughout the body, hSyn1-Cre for neurons of the CNS and PNS, GFAP-Cre for astrocytes, TH-Cre for dopaminergic cells and Fev-Cre for serotonergic cells. By performing our selections in parallel in multiple transgenic lines, we can employ both positive and negative selection, allowing us to target sequences recovered from a specific tissue of interest, and explicitly not recovered from others. For this, the recovered viral DNA from our tissues of interest is indexed and sent for next-generation sequencing (NGS), allowing us to see the specific sequences we positively and negatively selected. We then rank sequences based on prevalence in our targets of interest and synthesize a second-round library containing only the top-performing sequences (Fig. 1a).

The AA455 loop of AAV9 is the furthest protruding from the surface of the capsid (Fig. 1b) and has previously been implicated in neutralizing antibody binding[108]. The most commonly manipulated loop in AAVs is the AA588 loop, due to it being the site of heparan sulfate binding of AAV2[109] and amenable to peptide display[110–112]. The only known receptor for AAV9 is N-linked terminal galactose[113,114], but many indications point toward there being others. As the furthest protruding, as an integral part of the three-fold symmetry of the AAV[115], and due to its proximity to the AA588 loop which is the second furthest protruding, we theorize that the AA455 loop may also play a role in cell-surface receptor binding, either on its own or by interaction with the AA588 loop. Thus, we decided to make two viral libraries (Fig. 1a,b) by randomly substituting the amino acids of

this loop, AA452-458, both in AAV9 and in PHP.eB, a variant of AAV9 previously engineered at the AA588 loop for increased efficiency in crossing the BBB and transducing neurons[34].

4.3 Engineering AAV9 toward lung specificity

Naturally occurring AAVs have specific tropism to certain organs[25]. AAV9 transduces muscle very efficiently, expresses at high levels in the liver[26,27] and lower in other organs of the periphery. AAV9 is also one of a few viruses to be able to cross the blood-brain barrier and transduce the brain[116]. We performed two rounds of selection of a 7AA substitution (AA452-458) library in AAV9 and analyzed the sequencing results for variants enriched more highly in one organ vs. the others.

After the first round of selection, we found no bias for certain amino acids in our library, either in the produced virus (Fig. 2a) or in individual tissues (data not shown). We pooled the highest enriched variants from each organ and synthesized a second round containing approximately 6,000 unique variants. After a second round of selection, enrichment data showed a bias of certain variants toward specific tissues and away from others, and we curated a list of the top variants to test (Fig. 2b,c). We packaged mNeonGreen under control of the ubiquitous CAG promoter, injected $5x10^{11}$ viral genomes into wild-type mice and allowed two weeks for expression. The resulting expression in various organs (Fig. 2d) showed expression patterns that didn't deviate too much from AAV9, except in the organs which correlated with high enrichment scores from the NGS data (Fig. 2c). Specifically, AAV9.RWT4 expressed highly in the lungs and AAV9.RWT14 in the intestines and stomach. The lungs are not a target that AAV9 transduces at high levels normally[117], and AAV9.RWT4 shows an almost 5-fold increase in lung transduction (Fig. 2e,f), achieving similar levels as the serotype that most efficiently targets lungs, AAV5.

4.4 Engineering PHP.eB away from peripheral expression

Chan and colleagues recently characterized a virus, PHP.eB[34], that transduces the brain of mice at higher levels than any other systemically delivered AAV. PHP.eB, a 2 amino acid substitution from the previously described PHP.B[29], is 10-20% more efficient

and brighter in most areas of the brain than PHP.B, which itself is roughly 40-fold more efficient than AAV9. Although not characterized in the original paper, PHP.eB also has reduced expression in peripheral organs when compared to AAV9. For this reason, PHP.eB presented a unique opportunity for further engineering, to retain or amplify brain transduction, while also making it specific for the brain by further reducing or ablating targeting to the periphery. We performed two rounds of selection of a 7AA substitution (AA452-458) library in PHP.eB and then tested the variants most highly enriched in the brain vs. periphery.

After the first round of selection, we analyzed recovered sequences and synthesized a second round containing approximately 82,000 unique variants enriched in the brain compared to peripheral organs. These sequences didn't seem to follow any trends regarding their amino acid distribution (Fig. 3a), which didn't offer any insights into which amino acids at this position conferred the brain specificity we sought. After a second round of selection which narrowed down the top performing variants by a couple orders of magnitude, we selected a small subset of sequences to test (Fig. 3b) that exhibited high levels of enrichment for the brain, and negative enrichment for the liver and other peripheral organs (Fig. 3c). We tested this subset individually in wild-type mice, injecting $5x10^{11}$ viral genomes packaging CAG-mNeonGreen and allowing for two weeks of expression. The resulting expression in the brains and livers (Fig. 3d) correlated very closely with the NGS enrichments, with variant AAV9.ReB10 standing out as exhibiting higher fluorescence in the brain than PHP.eB and negligible liver transduction.

To fully characterize the performance of AAV9.ReB10 in comparison with AAV9 and PHP.eB, we packaged a nuclear localized CAG-EGFP and injected $1x10^{11}$ viral genomes into animals, waiting three weeks for expression. This dose was chosen as an average dose for previous experiments utilizing systemic delivery to the brain. Our results show an increase, while insignificant, in the average number of cells transduced in the brain, as well as the average level of expression per cell, between AAV9.ReB10 and PHP.eB, while both are very significantly higher than AAV9 (Fig. 4a,c). In the spinal cord, AAV9.ReB10 performs at roughly 60% of the efficiency of PHP.eB, yet still almost 20-fold higher than AAV9 (Supplementary Figure 1). Conversely, AAV9.ReB10 is very

significantly reduced in the liver compared to both PHP.eB (~50-fold) and AAV9 (>100-fold), and slightly, yet insignificantly, dimmer in brightness/cell compared to PHP.eB, while both are significantly dimmer than AAV9 (~10-fold) (Fig. 4b,d). In the rest of the periphery, the results follow the same trend, with PHP.eB being lower than AAV9, and AAV9.ReB10 being a fraction of PHP.eB (Supplementary Figure 1).

The above results match our NGS enrichment findings for both brain and periphery and are not surprising given the choice of PHP.eB as a parent. In this case, the insertion at the AA588 loop to make PHP.eB seems to confer a brain phenotype, and the substitutions at AA455 seem to refine that phenotype, conferring specificity to the brain away from the periphery. To further characterize what expression within the brain looked like for AAV9.ReB10 compared to PHP.eB, we stained for neurons, astrocytes and oligodendrocytes, and quantified the efficiency of the viruses at targeting those cell-types in various regions of the brain. While AAV9.ReB10 and PHP.eB transduced neurons at a similar efficiency across brain regions (Fig. 5a,b), astrocytes and oligodendrocytes were targeted roughly 4-5-fold lower levels across the whole brain by AAV9.ReB10 compared to PHP.eB (Fig. 5c,d,e,f). This result indicates a bias for neurons compared to other cell-types conferred by the AAV9.ReB10 mutations, an interesting deviation from AAV9, which mostly targets astrocytes in the brain[118,119]. An interesting indication from the NGS data for AAV9.ReB10 (Fig. 3c) was the variant's negative enrichment in the cerebellum. When characterizing the expression of AAV.ReB10 compared to PHP.eB in the cerebellum, we did indeed find a significant, roughly 4-fold, decrease in transduction of purkinje cells (Supplementary Figure 2).

4.5 Figures

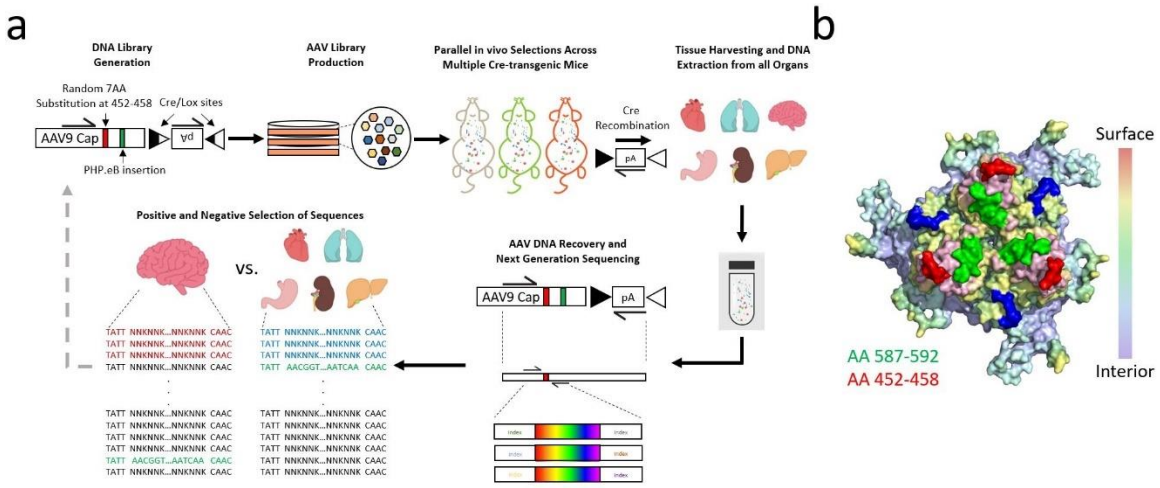

Figure 1. Viral engineering overview. (**a**) Using PCR, diversity is introduced in the form of a 7-amino acid insertion (PHP.eB insertion; green band) and/or substitution (AA 452-458; red band) in the rAAV9 genome, which harbors a Cre inducible switch surrounding the polyadenylation sequence. The DNA capsid library is transfected into HEK-293T cells, and diverse viral capsid libraries are harvested 60 hours later. The viral library is systemically injected into a panel of Cre-transgenic animals. Following three weeks of expression, tissue is harvested, and DNA extracted from all organs. Using PCR, sequences are selectively recovered from only those capsids which transduced Cre^{+} cells, flipping their polyadenylation sequence. The recovered sequences are subsequently prepared for next generation sequencing by PCR, adding dual-index barcodes unique to each specific Cre-tissue combination. Following NGS, the data is mined using positive and negative selection for enrichment (increased prevalence within a specific tissue compared to other sequences, normalized to their presence in the injected viral library) and specificity (increased prevalence within a specific tissue or cell type compared to other tissues or cell types). After one to two rounds of selection, individual variants are tested based on their enrichment and specificity scores. (**b**) Surface model of the AAV9 capsid, illustrating the location of the 7 amino acid substitution introduced in these libraries (red), with and without the 7 amino acid insertion introduced by PHP.eB (green).

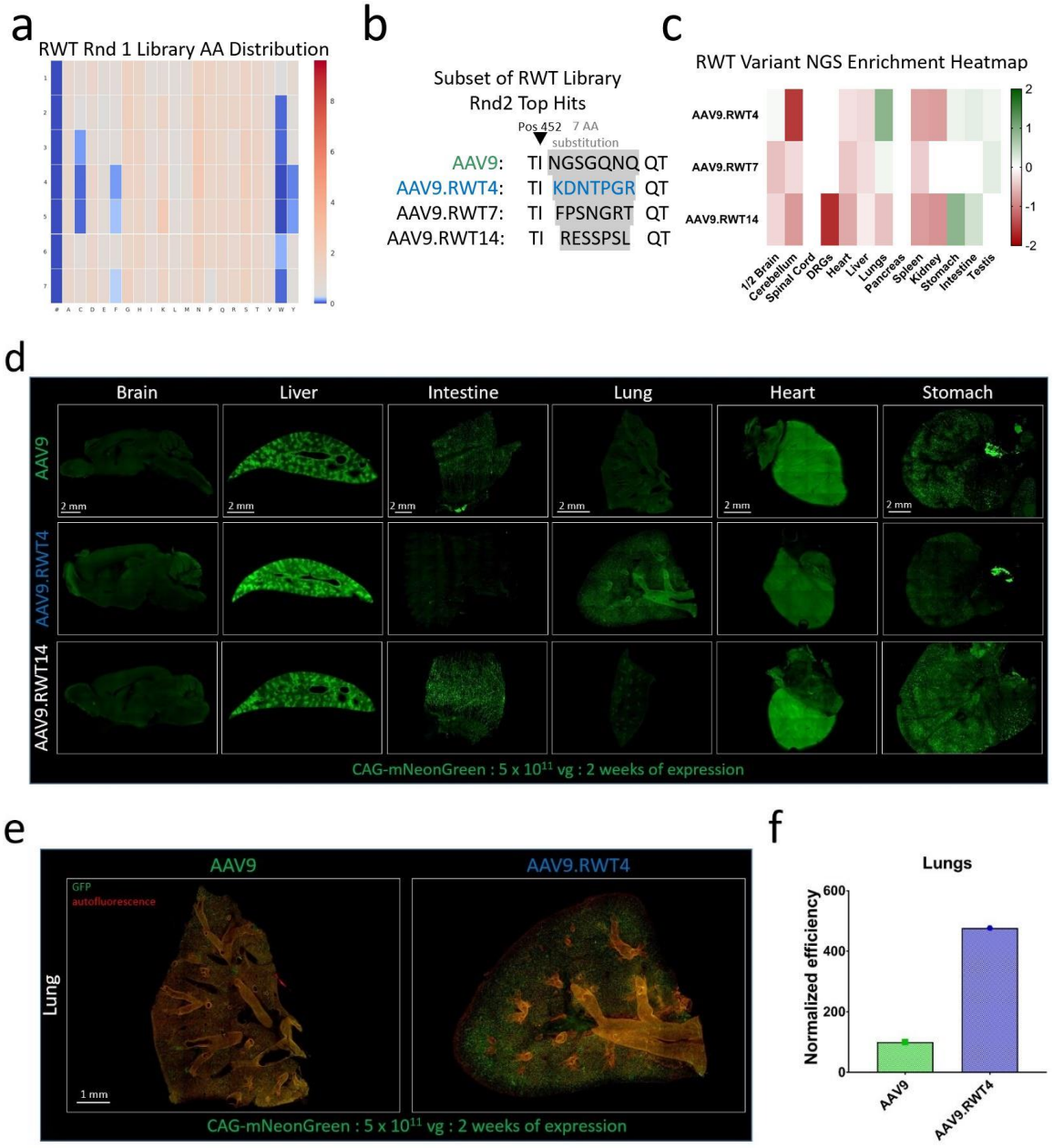

Figure 2. Characterization of the 7AA substitution library in AAV9. (**a**) The distribution across the 7 amino acid substitution in AAV9 introduced from AA452-458 demonstrates relatively little bias across the library, a low prevalence of stop codons, and no bias towards the WT AAV9 sequence (NGSGQNQ) following PCR generation of the DNA library and packaging of the viral capsid library in HEK-293T cells. (**b**) A subset of the top amino acid sequences recovered from two rounds of positive and negative selection for a variety of tissues and cell types. (**c**) A heat map plotting the log-scale enrichment scores of a subset of the top performers demonstrates diverse and non-overlapping enrichment and specificity in a variety of tissues. (**d**) ssAAV9:CAG-mNeonGreen, ssAAV9.RWT4:CAG-mNeonGreen orssAAV9.RWT14:CAG-mNeonGreen was intravenously injected into male adult mice at

5×10^{11} vg/mouse and mNeonGreen fluorescence assessed after two weeks. Direct comparison of the transduction profiles of two of the top performing variants specific for the lung and colon (RWT4 and RWT14, respectively) demonstrate strong fidelity between the selected tropism and NGS results. (**e, f**) Quantification of AAV9.RWT4 shows an approximately 4.7-fold increase in transduction efficiency in the lung when compared to AAV9 in n=1 mouse. Scale bars are 2 mm (d) and 1mm (e).

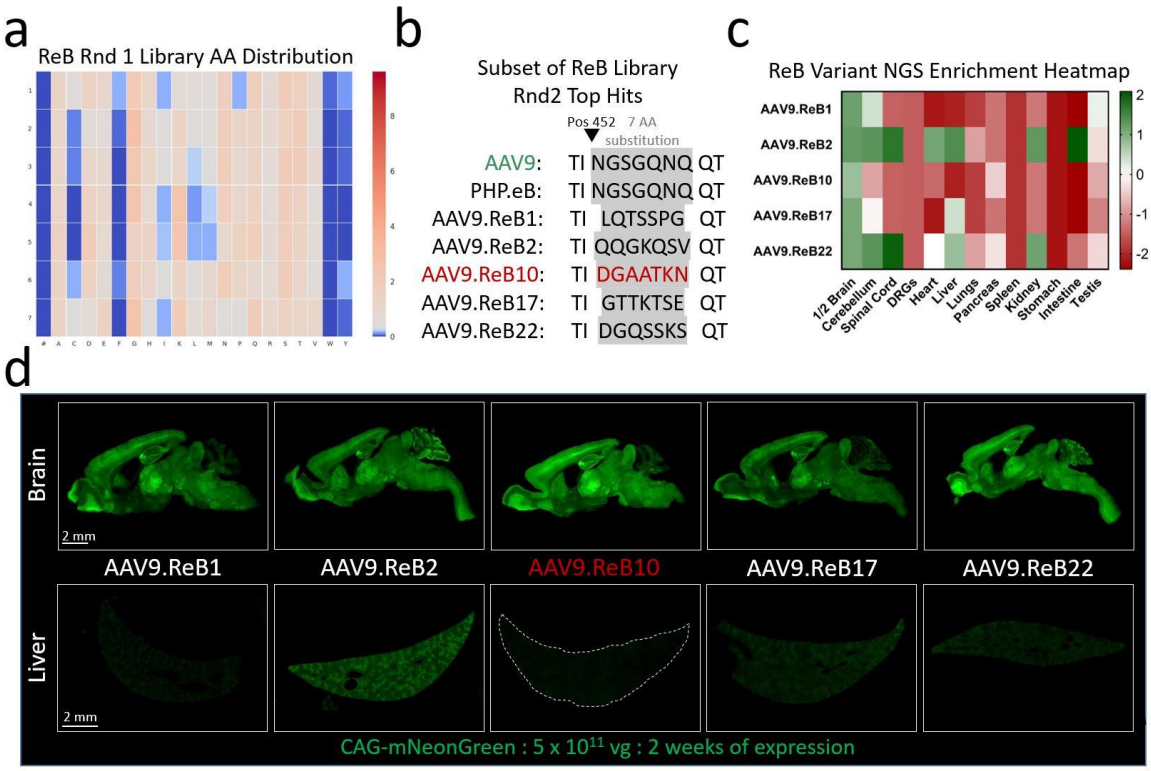

Figure 3. Characterization of the 7 AA substitution library in PHP.eB. (**a**) The distribution across the 7 amino acid substitution in PHP.eB shows a relatively uniform distribution, with a few notable exceptions, a low prevalence of stop codons, and no bias towards the WT AAV9 sequence (NGSGQNQ) following PCR generation of the DNA library and packaging of the viral capsid library. (**b**) A subset of the top performing variants obtained from two rounds of positive and negative selection are presented here, showing a strong divergence from the WT AAV9 sequence. (**c**) A heat map plotting the log-enrichment scores of a subset of the top performers demonstrates specificity for, and enrichment in, neuronal populations a target for which PHP.eB is already biased towards. (**d**) ssAAV9.ReB1:CAG-mNeonGreen, ssAAV9.ReB2:CAG-mNeonGreen, ssAAV9.ReB10:CAG-mNeonGreen, ssAAV9.ReB17:CAG-mNeonGreen or ssAAV9.ReB22:CAG-mNeonGreen was intravenously injected into male adult mice at 5×10^{11} vg/mouse and mNeonGreen fluorescence assessed after two weeks. Direct comparison of the transduction profiles of several of the top performing variants shows a strong correlation between validated tropisms, and those predicted by the NGS data. Scale bars are 2 mm.

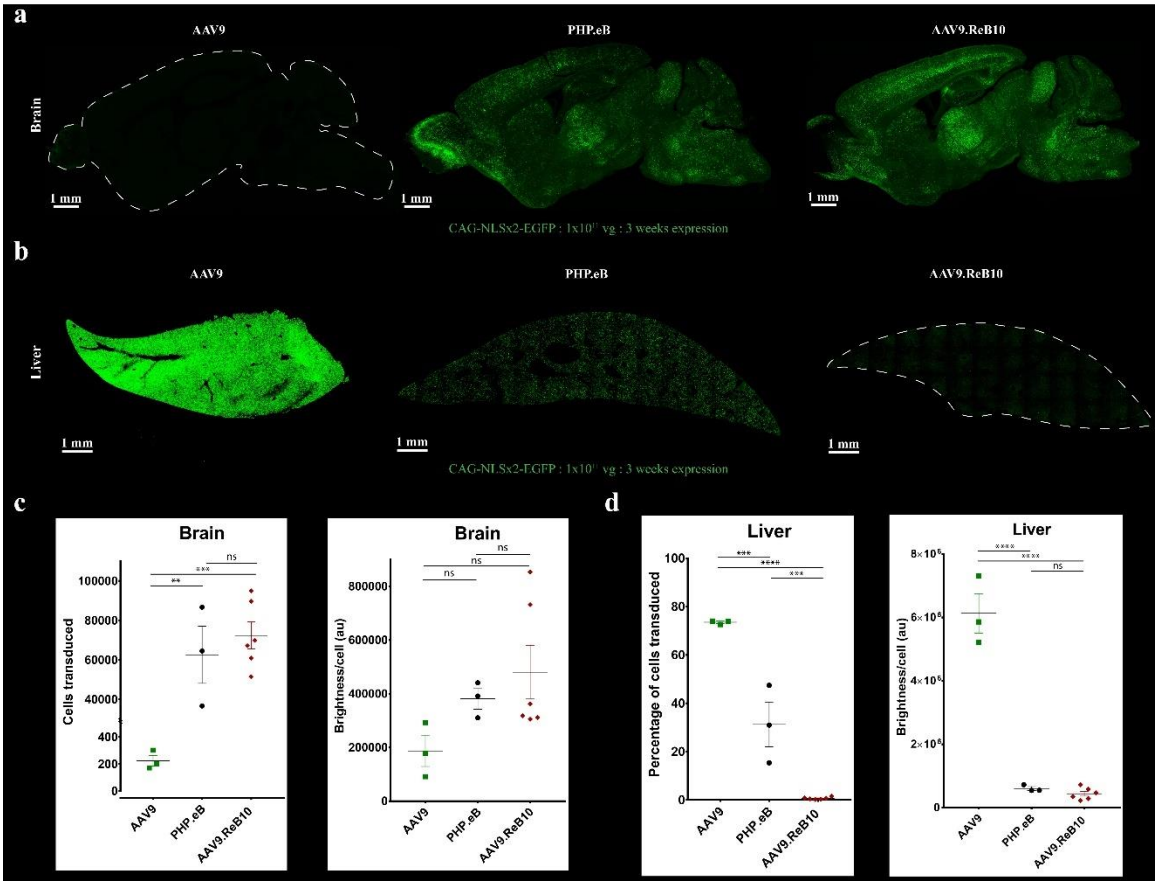

Figure 4. The tropism of AAV9.ReB10 is strongly biased towards the brain, with significant liver detargeting. ssAAV9:CAG-NLSx2-EGFP, ssPHP.eB:CAG-NLSx2-EGFP or ssAAV9.ReB10:CAG-NLSx2-EGFP was intravenously injected into male adult mice at 1×10^{11} vg/mouse. GFP fluorescence was assessed after three weeks of expression. (**a**) A comparison of BBB crossing and brain transduction in AAV9, PHP.eB, and AAV9.ReB10 shows a progressive increase in transduction efficiency in the brain following iterative engineering of the WT capsid. (**b**) Conversely, the same comparison in the livers shows a progressive decrease in transduction efficiency. (**c**) Quantification of the total number of cells transduced in the brain shows a non-significant increase in in total transduction for AAV9.ReB10 compared to PHP.eB, both of which are significantly increased compared to AAV9. Comparison of the average brightness per cell shows no significant difference between any of the variants. (**d**) Quantification of the total number of cells transduced in the liver shows a significant decrease comparing PHP.eB to AAV9. Furthermore, AAV9.ReB10 shows a significant decrease in transduction when compared to both AAV9 and PHP.eB. Brightness per cell is also significant decreased when comparing PHP.eB and AAV9.ReB10 to AAV9, with no significant difference observed between the two engineered variants. For quantification: n = 3 mice per group for AAV9 and AAV9.PHPeB, and 6 mice per group for AAV9.ReB10, mean ± SE, one-way ANOVA (*P ≤ 0.05; n.s., P ≥ 0.05). Scale bars are 1 mm.

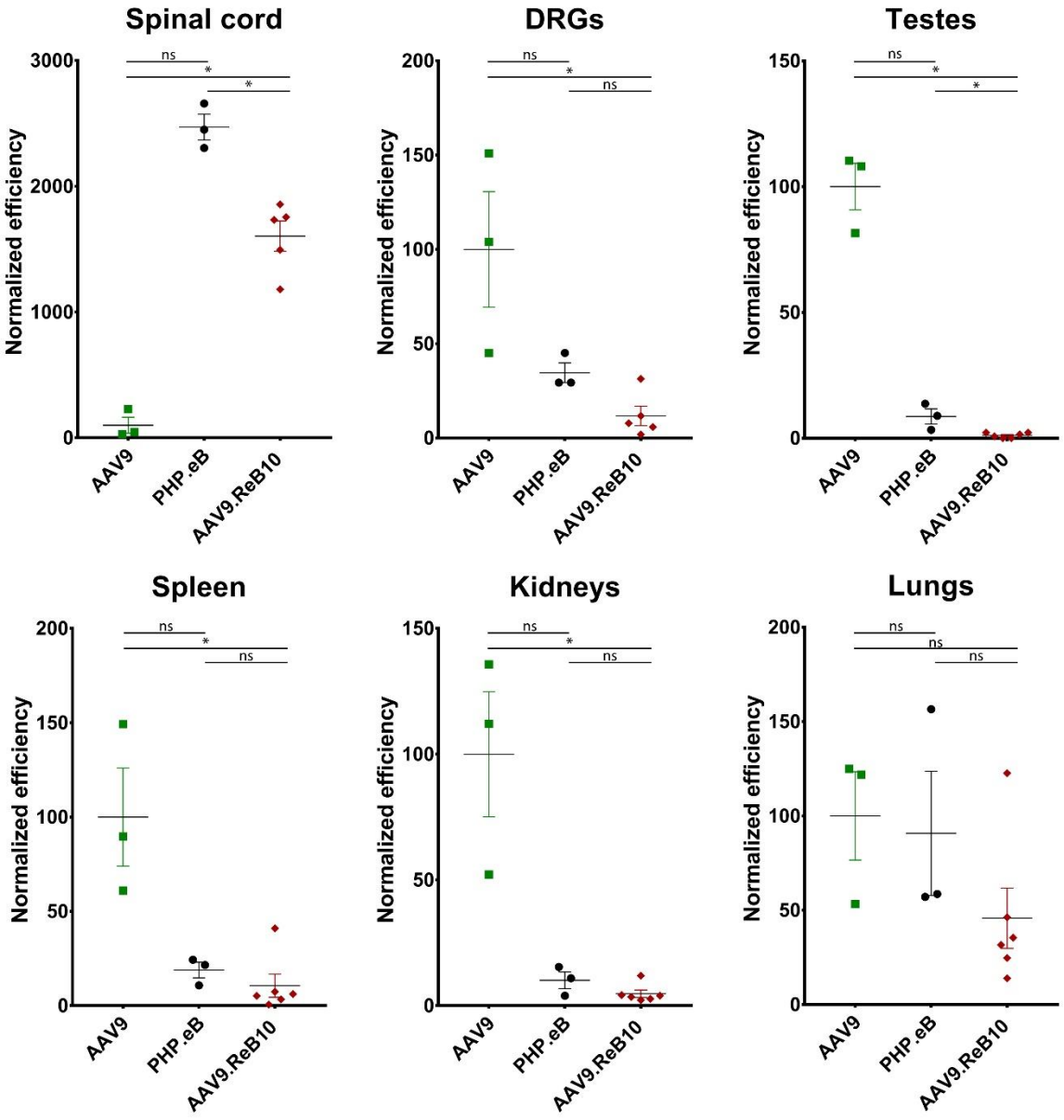

Supplementary Figure 1. AAV9.ReB10 is detargeted from peripheral organs. ssPHP.eB:CAG-NLSx2-EGFP or ssAAV9.ReB10:CAG-NLSx2-EGFP was intravenously injected into male adult mice at 1×10^{11} vg/mouse. GFP fluorescence was assessed after three weeks of expression. Transduction efficiencies in peripheral tissues show a significant increase in spinal cord transduction for AAV9.ReB10 when compared to AAV9, but a significant decrease when compared to PHP.eB. In the DRGs, AAV9.ReB10 is significantly decreased when compared to AAV9, and non-significantly decreased when compared to PHP.eB. In the testis, AAV9.ReB10 is significantly decreased when compared to both AAV9 and PHP.eB. In the spleen, AAV9.ReB10 is significantly decreased when

compared to AAV9, and non-significantly decreased when compared to PHP.eB. In the Kidneys, AAV9.ReB10 is significantly decreased when compared to AAV9, and non-significantly decreased when compared to PHP.eB. In the lungs, AAV9.ReB10 is non-significantly decreased when compared to both AAV9 and PHP.eB. For quantification: n = 3 mice per group for PHP.eB, and 6 mice per group for AAV9.ReB10, mean ± SE, Mann-Whitney test (*P ≤ 0.05; n.s., P ≥ 0.05).

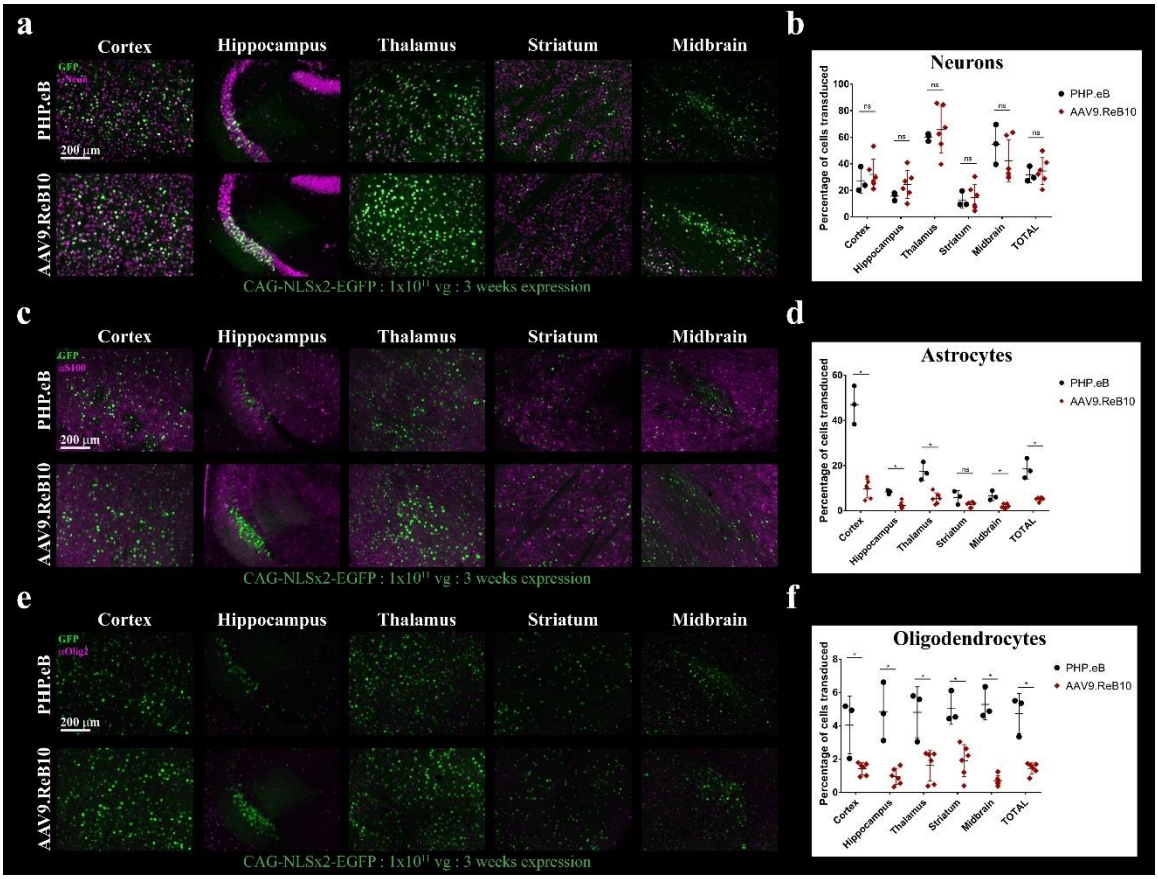

Figure 5. Within the brain, AAV9.ReB10 is strongly biased towards neurons. ssPHP.eB:CAG-NLSx2-EGFP or ssAAV9.ReB10:CAG-NLSx2-EGFP was intravenously injected into male adult mice at 1×10^{11} vg/mouse. GFP fluorescence was assessed after three weeks of expression. (**a**) Across multiple brain regions, AAV9.ReB10 showed non-significant increases in the total number of neurons transduced compared to PHP.eB, except for the midbrain, where AAV9.ReB10 showed a non-significant decrease. When taken as a whole, AAV9.ReB10 has a non-significant increase in the total number of neurons transduced compared to PHP.eB. (**b**) AAV9.ReB10 shows significantly reduced transduction of astrocytes across all brain regions quantified, except the striatum where it is trending towards significance. Total astrocyte transduction is also significantly decreased. (**c**) AAV9.ReB10 shows significantly reduced transduction of oligodendrocytes across all brain regions quantified. For quantification: n = 3 mice per group for PHP.eB, and 6 mice

per group for AAV9.ReB10, mean ± SE, Mann-Whitney test (*P ≤ 0.05; n.s., P ≥ 0.05). Scale bars are 200 µm.

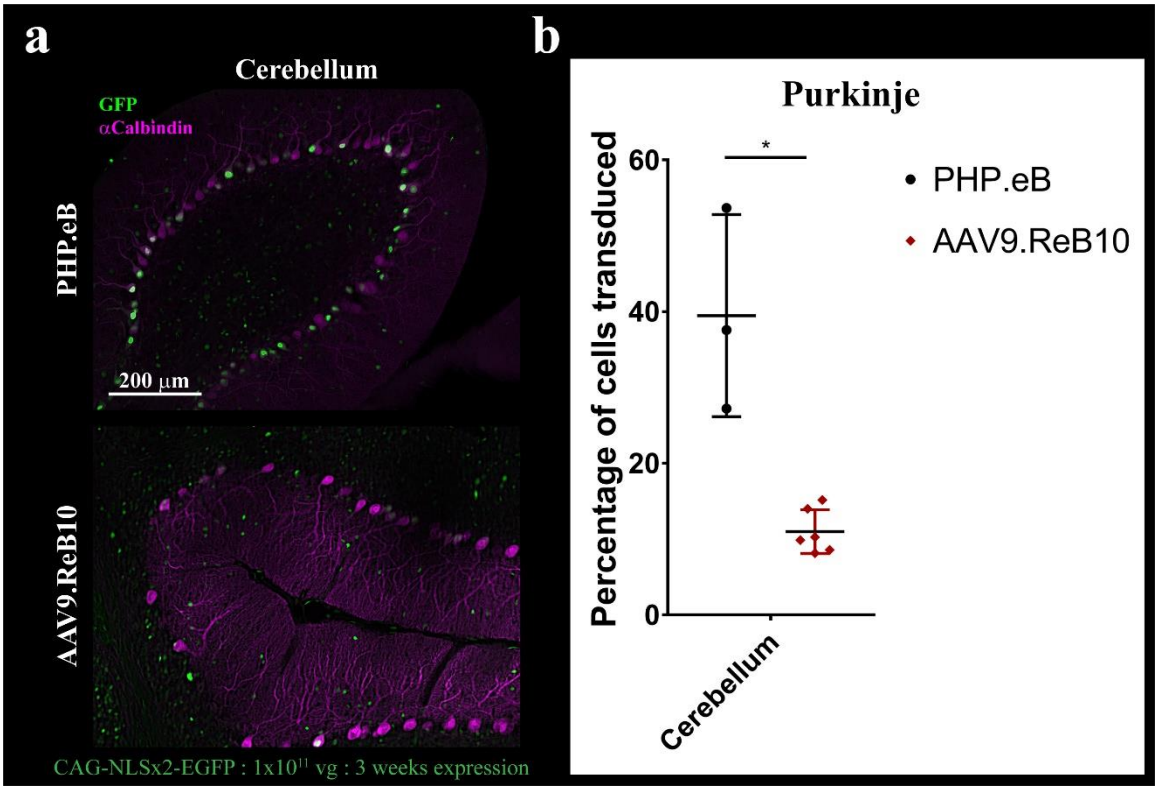

Supplementary Figure 2. AAV9.ReB10 is significantly detargeted from purkinje cells in the cerebellum. ssPHP.eB:CAG-NLSx2-EGFP or ssAAV9.ReB10:CAG-NLSx2-EGFP was intravenously injected into male adult mice at 1×10^{11} vg/mouse. GFP fluorescence was assessed after three weeks of expression. (**a, b**) Quantification of purkinje cell transduction in the cerebellum shows significantly fewer purkinje cells transduced by AAV.ReB10 when compared to PHP.eB. For quantification: n = 3 mice per group for PHP.eB, and 6 mice per group for AAV9.ReB10, mean ± SE, Mann-Whitney test (*P ≤ 0.05; n.s., P ≥ 0.05). Scale bar is 200 µm.

4.6 Future directions

Taken together, our results show that AAVs can be engineered for tissue or cell-type specificity, and that the resulting variants build upon previous engineering efforts. Our engineering efforts in the AAV9 background provided a panel of variants with increased or decreased specificity for certain peripheral organs compared to the AAV9 parent, without extreme deviations. Viruses overall hit similar targets to AAV9, with certain variants providing notable exceptions in specificity to certain organs, like AAV9.RWT4 to the

lungs. Our engineering efforts in the PHP.eB background also provided an array of variants with overall similar efficiency of targeting to the brain as PHP.eB. In this case, deviations from the parent were found in terms of targeting to other organs, where AAV9.ReB10 was significantly detargeted from the liver and other peripheral organs, or in terms of cell-type specificity, where AAV9.ReB10 transduced similar levels of neurons, but significantly lower in other cell-types. These results indicate that future engineering efforts should also take a step-wise approach toward attaining specificity for certain targets, with each variant building upon the previous. Both in the case of AAV9.RWT4 and AAV9.ReB10, further engineering can be done to further increase liver specificity and detargeting from other organs or change specificity toward other cell-types in the brain, respectively.

Regarding their therapeutic use for treating disease, both newly engineered viruses present notable findings toward more specific delivery vehicles. Both the lungs and the brain represent prime targets for gene therapy, for diseases like Cystic Fibrosis and COPD[120–122], or Huntington's, Parkinson's, and Friedreich's Ataxia[123–126]. Both organs are best targeted via systemic administration of AAVs, due to size of coverage needed and method of administration. In this case, specificity toward the therapeutic target of interest with decreased off-target expression is necessary to minimize side-effects. For these viruses to find eventual use in gene therapy applications, though, they need to be tested and characterized in non-human primates. Those experiments are forthcoming.

BIBLIOGRAPHY

1. Spudich, J. L., Yang, C.-S., Jung, K.-H. & Spudich, E. N. Retinylidene Proteins: Structures and Functions from Archaea to Humans. *Annu. Rev. Cell Dev. Biol.* **16,** 365–392 (2000).
2. Sakmar, T. P. Structure of rhodopsin and the superfamily of seven-helical receptors: the same and not the same. *Curr. Opin. Cell Biol.* **14,** 189–195 (2002).
3. Boyden, E. S., Zhang, F., Bamberg, E., Nagel, G. & Deisseroth, K. Millisecond-timescale, genetically targeted optical control of neural activity. *Nat. Neurosci.* **8,** 1263–1268 (2005).
4. Klapoetke, N. C. *et al.* Independent optical excitation of distinct neural populations. *Nat. Methods* **11,** 338–346 (2014).
5. Bedbrook, C. N. *et al.* Structure-guided SCHEMA recombination generates diverse chimeric channelrhodopsins. *Proc. Natl. Acad. Sci.* **114,** E2624–E2633 (2017).
6. Engqvist, M. K. M. *et al.* Directed Evolution of Gloeobacter violaceus Rhodopsin Spectral Properties. *J. Mol. Biol.* **427,** 205–220 (2015).
7. Lenz, M. O. *et al.* First Steps of Retinal Photoisomerization in Proteorhodopsin. *Biophys. J.* **91,** 255–262 (2006).
8. Kralj, J. M., Douglass, A. D., Hochbaum, D. R., Maclaurin, D. & Cohen, A. E. Optical recording of action potentials in mammalian neurons using a microbial rhodopsin. *Nat. Methods* **9,** 90–95 (2012).
9. Chen, T.-W. *et al.* Ultrasensitive fluorescent proteins for imaging neuronal activity. *Nature* **499,** 295–300 (2013).
10. Knöpfel, T., Gallero-Salas, Y. & Song, C. Genetically encoded voltage indicators for large scale cortical imaging come of age. *Curr. Opin. Chem. Biol.* **27,** 75–83 (2015).
11. Emiliani, V., Cohen, A. E., Deisseroth, K. & Häusser, M. All-Optical Interrogation of Neural Circuits. *J. Neurosci.* **35,** 13917–13926 (2015).
12. McIsaac, R. S. *et al.* Directed evolution of a far-red fluorescent rhodopsin. *Proc. Natl. Acad. Sci.* **111,** 13034–13039 (2014).
13. Flytzanis, N. C. *et al.* Archaerhodopsin variants with enhanced voltage-sensitive fluorescence in mammalian and *Caenorhabditis elegans* neurons. *Nat. Commun.* **5,** 4894 (2014).
14. Chung, K. *et al.* Structural and molecular interrogation of intact biological systems. *Nature* **497,** 332–337 (2013).
15. Yang, B. *et al.* Single-Cell Phenotyping within Transparent Intact Tissue Through Whole-Body Clearing. *Cell* **158,** 945–958 (2014).
16. Treweek, J. B. *et al.* Whole-body tissue stabilization and selective extractions via tissue-hydrogel hybrids for high-resolution intact circuit mapping and phenotyping. *Nat. Protoc.* **10,** 1860–1896 (2015).
17. Vega-Lopez, G. A., Cerrizuela, S., Tribulo, C. & Aybar, M. J. Neurocristopathies: New insights 150 years after the neural crest discovery. *Dev. Biol.* (2018). doi:10.1016/j.ydbio.2018.05.013
18. Huang, X. & Saint-Jeannet, J.-P. Induction of the neural crest and the opportunities of life on the edge. *Dev. Biol.* **275,** 1–11 (2004).
19. Le Lièvre, C. S. & Le Douarin, N. M. Mesenchymal derivatives of the neural crest: analysis of chimaeric quail and chick embryos. *J. Embryol. Exp. Morphol.* **34,** 125–154 (1975).

20. Bellairs, R., Ireland, G. W., Sanders, E. J. & Stern, C. D. The behaviour of embryonic chick and quail tissues in culture. *J. Embryol. Exp. Morphol.* **61,** 15–33 (1981).
21. Gaudet, D., Méthot, J. & Kastelein, J. Gene therapy for lipoprotein lipase deficiency. *Curr. Opin. Lipidol.* **23,** 310–320 (2012).
22. Ameri, H. Prospect of retinal gene therapy following commercialization of voretigene neparvovec-rzyl for retinal dystrophy mediated by RPE65 mutation. *J. Curr. Ophthalmol.* **30,** 1–2 (2018).
23. Evens, H., Chuah, M. K. & VandenDriessche, T. Haemophilia gene therapy: From trailblazer to gamechanger. *Haemoph. Off. J. World Fed. Hemoph.* **24 Suppl 6,** 50–59 (2018).
24. Kabra, A., Sharma, R., Kabra, R. & Baghel, U. S. Emerging and alternative therapies for Parkinson disease: an updated review. *Curr. Pharm. Des.* (2018). doi:10.2174/1381612824666180820150150
25. Srivastava, A. In vivo tissue-tropism of adeno-associated viral vectors. *Curr. Opin. Virol.* **21,** 75–80 (2016).
26. Xie, J. *et al.* MicroRNA-regulated, Systemically Delivered rAAV9: A Step Closer to CNS-restricted Transgene Expression. *Mol. Ther.* **19,** 526–535 (2011).
27. Pulicherla, N. *et al.* Engineering Liver-detargeted AAV9 Vectors for Cardiac and Musculoskeletal Gene Transfer. *Mol. Ther.* **19,** 1070–1078 (2011).
28. Calcedo, R., Chichester, J. A. & Wilson, J. M. Assessment of humoral, innate, and T-cell immune responses to adeno-associated virus vectors. *Hum. Gene Ther. Methods* (2018). doi:10.1089/hum.2018.038
29. Deverman, B. E. *et al.* Cre-dependent selection yields AAV variants for widespread gene transfer to the adult brain. *Nat. Biotechnol.* **34,** 204–209 (2016).
30. Grimm, D. *et al.* In Vitro and In Vivo Gene Therapy Vector Evolution via Multispecies Interbreeding and Retargeting of Adeno-Associated Viruses. *J. Virol.* **82,** 5887–5911 (2008).
31. Excoffon, K. J. D. A. *et al.* Directed evolution of adeno-associated virus to an infectious respiratory virus. *Proc. Natl. Acad. Sci.* **106,** 3865–3870 (2009).
32. Maheshri, N., Koerber, J. T., Kaspar, B. K. & Schaffer, D. V. Directed evolution of adeno-associated virus yields enhanced gene delivery vectors. *Nat. Biotechnol.* **24,** 198–204 (2006).
33. Dalkara, D. *et al.* In Vivo–Directed Evolution of a New Adeno-Associated Virus for Therapeutic Outer Retinal Gene Delivery from the Vitreous. *Sci. Transl. Med.* **5,** 189ra76-189ra76 (2013).
34. Chan, K. Y. *et al.* Engineered AAVs for efficient noninvasive gene delivery to the central and peripheral nervous systems. *Nat. Neurosci.* **20,** 1172–1179 (2017).
35. Black, S. D. & Mould, D. R. Development of hydrophobicity parameters to analyze proteins which bear post- or cotranslational modifications. *Anal. Biochem.* **193,** 72–82 (1991).
36. Kim, S. Y., Waschuk, S. A., Brown, L. S. & Jung, K.-H. Screening and characterization of proteorhodopsin color-tuning mutations in Escherichia coli with endogenous retinal synthesis. *Biochim. Biophys. Acta BBA - Bioenerg.* **1777,** 504–513 (2008).
37. Sudo, Y. *et al.* A Blue-shifted Light-driven Proton Pump for Neural Silencing. *J. Biol. Chem.* **288,** 20624–20632 (2013).
38. Otto, H. *et al.* Substitution of amino acids Asp-85, Asp-212, and Arg-82 in bacteriorhodopsin affects the proton release phase of the pump and the pK of the Schiff base. *Proc. Natl. Acad. Sci.* **87,** 1018–1022 (1990).
39. Saeedi, P. *et al.* Generation and analysis of bacteriorhodopsin mutants with the potential for biotechnological applications. *Bioengineered* **3,** 275–279 (2012).

40. Saeedi, P., Moosaabadi, J. M., Sebtahmadi, S. S., Behmanesh, M. & Mehrabadi, J. F. Site-directed mutagenesis in bacteriorhodopsin mutants and their characterization for bioelectrical and biotechnological equipment. *Biotechnol. Lett.* **34,** 455–462 (2012).
41. Tittor, J. *et al.* Chloride and proton transport in bacteriorhodopsin mutant D85T: different modes of ion translocation in a retinal protein11Edited by A.R.Fersht. *J. Mol. Biol.* **271,** 405–416 (1997).
42. Briand, J., Léonard, J. & Haacke, S. Ultrafast photo-induced reaction dynamics in bacteriorhodopsin and its Trp mutants. *J. Opt.* **12,** 084004 (2010).
43. Russell, T. S., Coleman, M., Rath, P., Nilsson, A. & Rothschild, K. J. Threonine-89 Participates in the Active Site of Bacteriorhodopsin: Evidence for a Role in Color Regulation and Schiff Base Proton Transfer. *Biochemistry* **36,** 7490–7497 (1997).
44. Perálvarez-Marín, A., Bourdelande, J.-L., Querol, E. & Padrós, E. The role of proline residues in the dynamics of transmembrane helices: the case of bacteriorhodopsin. *Mol. Membr. Biol.* **23,** 127–135 (2006).
45. Subramaniam, S., Marti, T. & Khorana, H. G. Protonation state of Asp (Glu)-85 regulates the purple-to-blue transition in bacteriorhodopsin mutants Arg-82----Ala and Asp-85----Glu: the blue form is inactive in proton translocation. *Proc. Natl. Acad. Sci.* **87,** 1013–1017 (1990).
46. Subramaniam, S., Greenhalgh, D. A., Rath, P., Rothschild, K. J. & Khorana, H. G. Replacement of leucine-93 by alanine or threonine slows down the decay of the N and O intermediates in the photocycle of bacteriorhodopsin: implications for proton uptake and 13-cis-retinal----all-trans-retinal reisomerization. *Proc. Natl. Acad. Sci.* **88,** 6873–6877 (1991).
47. Jang, D. J., el-Sayed, M. A., Stern, L. J., Mogi, T. & Khorana, H. G. Effect of genetic modification of tyrosine-185 on the proton pump and the blue-to-purple transition in bacteriorhodopsin. *Proc. Natl. Acad. Sci.* **87,** 4103–4107 (1990).
48. Hashimoto, S., Obata, K., Takeuchi, H., Needleman, R. & Lanyi, J. K. Ultraviolet Resonance Raman Spectra of Trp-182 and Trp-189 in Bacteriorhodopsin: Novel Information on the Structure of Trp-182 and Its Steric Interaction with Retinal. *Biochemistry* **36,** 11583–11590 (1997).
49. Wang, W.-W., Sineshchekov, O. A., Spudich, E. N. & Spudich, J. L. Spectroscopic and Photochemical Characterization of a Deep Ocean Proteorhodopsin. *J. Biol. Chem.* **278,** 33985–33991 (2003).
50. Tamogami, J. *et al.* Photoinduced Proton Release in Proteorhodopsin at Low pH: The Possibility of a Decrease in the pKa of Asp227. *Biochemistry* **51,** 9290–9301 (2012).
51. Maiti, T. K., Yamada, K., Inoue, K. & Kandori, H. L105K Mutant of Proteorhodopsin. *Biochemistry* **51,** 3198–3204 (2012).
52. Gradinaru, V. *et al.* Molecular and cellular approaches for diversifying and extending optogenetics. *Cell* **141,** 154–165 (2010).
53. Göbel, W., Kampa, B. M. & Helmchen, F. Imaging cellular network dynamics in three dimensions using fast 3D laser scanning. *Nat. Methods* **4,** 73–79 (2007).
54. Cao, G. *et al.* Genetically Targeted Optical Electrophysiology in Intact Neural Circuits. *Cell* **154,** 904–913 (2013).
55. Peters, A. J., Chen, S. X. & Komiyama, T. Emergence of reproducible spatiotemporal activity during motor learning. *Nature* **510,** 263–267 (2014).
56. Quirin, S., Jackson, J., Peterka, D. S. & Yuste, R. Simultaneous imaging of neural activity in three dimensions. *Front. Neural Circuits* **8,** (2014).

57. Mutoh, H., Akemann, W. & Knöpfel, T. Genetically Engineered Fluorescent Voltage Reporters. *ACS Chem. Neurosci.* **3,** 585–592 (2012).
58. St-Pierre, F. *et al.* High-fidelity optical reporting of neuronal electrical activity with an ultrafast fluorescent voltage sensor. *Nat. Neurosci.* **17,** 884–889 (2014).
59. Gong, Y., Wagner, M. J., Zhong Li, J. & Schnitzer, M. J. Imaging neural spiking in brain tissue using FRET-opsin protein voltage sensors. *Nat. Commun.* **5,** 3674 (2014).
60. Hochbaum, D. R. *et al.* All-optical electrophysiology in mammalian neurons using engineered microbial rhodopsins. *Nat. Methods* **11,** 825–833 (2014).
61. Tian, L. *et al.* Imaging neural activity in worms, flies and mice with improved GCaMP calcium indicators. *Nat. Methods* **6,** 875–881 (2009).
62. Akerboom, J. *et al.* Optimization of a GCaMP Calcium Indicator for Neural Activity Imaging. *J. Neurosci.* **32,** 13819–13840 (2012).
63. Jin, L. *et al.* Single Action Potentials and Subthreshold Electrical Events Imaged in Neurons with a Fluorescent Protein Voltage Probe. *Neuron* **75,** 779–785 (2012).
64. Mattis, J. *et al.* Principles for applying optogenetic tools derived from direct comparative analysis of microbial opsins. *Nat. Methods* **9,** 159–172 (2012).
65. Lin, J. Y., Knutsen, P. M., Muller, A., Kleinfeld, D. & Tsien, R. Y. ReaChR: a red-shifted variant of channelrhodopsin enables deep transcranial optogenetic excitation. *Nat. Neurosci.* **16,** 1499–1508 (2013).
66. Chow, B. Y. *et al.* High-performance genetically targetable optical neural silencing by light-driven proton pumps. *Nature* **463,** 98–102 (2010).
67. Gong, Y., Li, J. Z. & Schnitzer, M. J. Enhanced Archaerhodopsin Fluorescent Protein Voltage Indicators. *PLOS ONE* **8,** e66959 (2013).
68. Chalasani, S. H. *et al.* Dissecting a circuit for olfactory behaviour in *Caenorhabditis elegans*. *Nature* **450,** 63–70 (2007).
69. Kato, S., Xu, Y., Cho, C. E., Abbott, L. F. & Bargmann, C. I. Temporal Responses of C. elegans Chemosensory Neurons Are Preserved in Behavioral Dynamics. *Neuron* **81,** 616–628 (2014).
70. Nickell, W. T., Pun, R. Y. K., Bargmann, C. I. & Kleene, S. J. Single Ionic Channels of Two Caenorhabditis elegans Chemosensory Neurons in Native Membrane. *J. Membr. Biol.* **189,** 55–66 (2002).
71. Gao, S. & Zhen, M. Action potentials drive body wall muscle contractions in Caenorhabditis elegans. *Proc. Natl. Acad. Sci.* **108,** 2557–2562 (2011).
72. Looger, L. L. Running in reverse: rhodopsins sense voltage. *Nat. Methods* **9,** 43–44 (2012).
73. Grishkevich, V., Hashimshony, T. & Yanai, I. Core promoter T-blocks correlate with gene expression levels in C. elegans. *Genome Res.* **21,** 707–717 (2011).
74. Mello, C. & Fire, A. DNA transformation. *Methods Cell Biol.* **48,** 451–482 (1995).
75. Chung, K. & Deisseroth, K. CLARITY for mapping the nervous system. *Nat. Methods* **10,** 508–513 (2013).
76. Dodt, H.-U. *et al.* Ultramicroscopy: three-dimensional visualization of neuronal networks in the whole mouse brain. *Nat. Methods* **4,** 331–336 (2007).
77. Ertürk, A. *et al.* Three-dimensional imaging of solvent-cleared organs using 3DISCO. *Nat. Protoc.* **7,** 1983–1995 (2012).
78. Ertürk, A. *et al.* Three-dimensional imaging of the unsectioned adult spinal cord to assess axon regeneration and glial responses after injury. *Nat. Med.* **18,** 166–171 (2012).

79. Becker, K., Jährling, N., Saghafi, S., Weiler, R. & Dodt, H.-U. Chemical Clearing and Dehydration of GFP Expressing Mouse Brains. *PLOS ONE* **7,** e33916 (2012).
80. Renier, N. *et al.* iDISCO: A Simple, Rapid Method to Immunolabel Large Tissue Samples for Volume Imaging. *Cell* **159,** 896–910 (2014).
81. Bucher, D., Scholz, M., Stetter, M., Obermayer, K. & Pflüger, H.-J. Correction methods for three-dimensional reconstructions from confocal images: I. tissue shrinking and axial scaling. *J. Neurosci. Methods* **100,** 135–143 (2000).
82. Staudt, T., Lang, M. C., Medda, R., Engelhardt, J. & Hell, S. W. 2,2'-Thiodiethanol: A new water soluble mounting medium for high resolution optical microscopy. *Microsc. Res. Tech.* **70,** 1–9 (2007).
83. Ke, M.-T., Fujimoto, S. & Imai, T. SeeDB: a simple and morphology-preserving optical clearing agent for neuronal circuit reconstruction. *Nat. Neurosci.* **16,** 1154–1161 (2013).
84. Kuwajima, T. *et al.* ClearT: a detergent- and solvent-free clearing method for neuronal and non-neuronal tissue. *Development* **140,** 1364–1368 (2013).
85. Hama, H. *et al.* Scale: a chemical approach for fluorescence imaging and reconstruction of transparent mouse brain. *Nat. Neurosci.* **14,** 1481–1488 (2011).
86. Susaki, E. A. *et al.* Whole-Brain Imaging with Single-Cell Resolution Using Chemical Cocktails and Computational Analysis. *Cell* **157,** 726–739 (2014).
87. Tomer, R., Ye, L., Hsueh, B. & Deisseroth, K. Advanced CLARITY for rapid and high-resolution imaging of intact tissues. *Nat. Protoc.* **9,** 1682–1697 (2014).
88. Tainaka, K. *et al.* Whole-Body Imaging with Single-Cell Resolution by Tissue Decolorization. *Cell* **159,** 911–924 (2014).
89. Ott, H. C. *et al.* Perfusion-decellularized matrix: using nature's platform to engineer a bioartificial heart. *Nat. Med.* **14,** 213–221 (2008).
90. Grace, A. A. & Llinás, R. Morphological artifacts induced in intracellularly stained neurons by dehydration: Circumvention using rapid dimethyl sulfoxide clearing. *Neuroscience* **16,** 461–475 (1985).
91. Chen, F., Tillberg, P. W. & Boyden, E. S. Expansion microscopy. *Science* **347,** 543–548 (2015).
92. Goeden, N. & Bonnin, A. Ex vivo perfusion of mid-to-late-gestation mouse placenta for maternal-fetal interaction studies during pregnancy. *Nat. Protoc.* **8,** 66–74 (2013).
93. Mohammed, R., Cavallaro, G., Kessels, C. G. A. & Villamor, E. Functional differences between the arteries perfusing gas exchange and nutritional membranes in the late chicken embryo. *J. Comp. Physiol. [B]* **185,** 783–796 (2015).
94. Choi, H. M. T. *et al.* Third-generation in situ hybridization chain reaction: multiplexed, quantitative, sensitive, versatile, robust. *Dev. Camb. Engl.* **145,** (2018).
95. Kirby, M. L., Weidman, T. A. & McKenzie, J. W. An ultrastructural study of the cardia ganglia in the bulbar plexus of the developing chick heart. *Dev. Neurosci.* **3,** 174–184 (1980).
96. Boot, M. J., Gittenberger-De Groot, A. C., Van Iperen, L., Hierck, B. P. & Poelmann, R. E. Spatiotemporally separated cardiac neural crest subpopulations that target the outflow tract septum and pharyngeal arch arteries. *Anat. Rec. A. Discov. Mol. Cell. Evol. Biol.* **275,** 1009–1018 (2003).
97. Phillips, M. T., Kirby, M. L. & Forbes, G. Analysis of cranial neural crest distribution in the developing heart using quail-chick chimeras. *Circ. Res.* **60,** 27–30 (1987).

98. Waldo, K., Miyagawa-Tomita, S., Kumiski, D. & Kirby, M. L. Cardiac neural crest cells provide new insight into septation of the cardiac outflow tract: aortic sac to ventricular septal closure. *Dev. Biol.* **196,** 129–144 (1998).
99. Komatsu, K. *et al.* Meltrin beta expressed in cardiac neural crest cells is required for ventricular septum formation of the heart. *Dev. Biol.* **303,** 82–92 (2007).
100. Maeda, K. *et al.* Postotic and preotic cranial neural crest cells differently contribute to thyroid development. *Dev. Biol.* **409,** 72–83 (2016).
101. Narayanan, C. H. & Narayanan, Y. Neural crest and placodal contributions in the development of the glossopharyngeal-vagal complex in the chick. *Anat. Rec.* **196,** 71–82 (1980).
102. Verberne, M. E., Gittenberger-de Groot, A. C., van Iperen, L. & Poelmann, R. E. Distribution of different regions of cardiac neural crest in the extrinsic and the intrinsic cardiac nervous system. *Dev. Dyn. Off. Publ. Am. Assoc. Anat.* **217,** 191–204 (2000).
103. Thompson, H., Blentic, A., Watson, S., Begbie, J. & Graham, A. The formation of the superior and jugular ganglia: Insights into the generation of sensory neurons by the neural crest. *Dev. Dyn.* **239,** 439–445 (2010).
104. Kalcheim, C. & Kumar, D. Cell fate decisions during neural crest ontogeny. *Int. J. Dev. Biol.* **61,** 195–203 (2017).
105. Lumsden, A., Sprawson, N. & Graham, A. Segmental origin and migration of neural crest cells in the hindbrain region of the chick embryo. *Dev. Camb. Engl.* **113,** 1281–1291 (1991).
106. Hood, L. C. & Rosenquist, T. H. Coronary artery development in the chick: origin and deployment of smooth muscle cells, and the effects of neural crest ablation. *Anat. Rec.* **234,** 291–300 (1992).
107. Arima, Y. *et al.* Preotic neural crest cells contribute to coronary artery smooth muscle involving endothelin signalling. *Nat. Commun.* **3,** 1267 (2012).
108. Adachi, K., Enoki, T., Kawano, Y., Veraz, M. & Nakai, H. Drawing a high-resolution functional map of adeno-associated virus capsid by massively parallel sequencing. *Nat. Commun.* **5,** 3075 (2014).
109. Kern, A. *et al.* Identification of a Heparin-Binding Motif on Adeno-Associated Virus Type 2 Capsids. *J. Virol.* **77,** 11072–11081 (2003).
110. Girod, A. *et al.* Genetic capsid modifications allow efficient re-targeting of adeno-associated virus type 2. *Nat. Med.* **5,** 1052–1056 (1999).
111. Michelfelder, S. *et al.* Successful Expansion but Not Complete Restriction of Tropism of Adeno-Associated Virus by In Vivo Biopanning of Random Virus Display Peptide Libraries. *PLOS ONE* **4,** e5122 (2009).
112. Michelfelder, S. *et al.* Peptide Ligands Incorporated into the Threefold Spike Capsid Domain to Re-Direct Gene Transduction of AAV8 and AAV9 In Vivo. *PLOS ONE* **6,** e23101 (2011).
113. Bell, C. L. *et al.* The AAV9 receptor and its modification to improve in vivo lung gene transfer in mice. *J. Clin. Invest.* **121,** 2427–2435 (2011).
114. Shen, S., Bryant, K. D., Brown, S. M., Randell, S. H. & Asokan, A. Terminal N-Linked Galactose Is the Primary Receptor for Adeno-associated Virus 9. *J. Biol. Chem.* **286,** 13532–13540 (2011).
115. DiMattia, M. A. *et al.* Structural Insight into the Unique Properties of Adeno-Associated Virus Serotype 9. *J. Virol.* **86,** 6947–6958 (2012).

116. Manfredsson, F. P., Rising, A. C. & Mandel, R. J. AAV9: a potential blood-brain barrier buster. *Mol. Ther. J. Am. Soc. Gene Ther.* **17,** 403–405 (2009).
117. Limberis, M. P. & Wilson, J. M. Adeno-associated virus serotype 9 vectors transduce murine alveolar and nasal epithelia and can be readministered. *Proc. Natl. Acad. Sci.* **103,** 12993–12998 (2006).
118. Foust, K. D. *et al.* Intravascular AAV9 preferentially targets neonatal neurons and adult astrocytes. *Nat. Biotechnol.* **27,** 59–65 (2009).
119. Samaranch, L. *et al.* Adeno-Associated Virus Serotype 9 Transduction in the Central Nervous System of Nonhuman Primates. *Hum. Gene Ther.* **23,** 382–389 (2011).
120. Al-Jamal, R., Wallace, W. a. H. & Harrison, D. J. Gene therapy for chronic obstructive pulmonary disease: twilight or triumph? *Expert Opin. Biol. Ther.* **5,** 333–346 (2005).
121. Guggino, W. B. & Cebotaru, L. AAV gene therapy for cystic fibrosis: current barriers and recent developments. *Expert Opin. Biol. Ther.* **17,** 1265–1273 (2017).
122. Oh, D. K., Kim, Y.-S. & Oh, Y.-M. Lung Regeneration Therapy for Chronic Obstructive Pulmonary Disease. *Tuberc. Respir. Dis.* **80,** 1–10 (2017).
123. Coune, P. G., Schneider, B. L. & Aebischer, P. Parkinson's Disease: Gene Therapies. *Cold Spring Harb. Perspect. Med.* **2,** (2012).
124. Combs, B., Kneynsberg, A. & Kanaan, N. M. Gene Therapy Models of Alzheimer's Disease and Other Dementias. *Methods Mol. Biol. Clifton NJ* **1382,** 339–366 (2016).
125. Piguet, F. *et al.* Rapid and Complete Reversal of Sensory Ataxia by Gene Therapy in a Novel Model of Friedreich Ataxia. *Mol. Ther.* **26,** 1940–1952 (2018).
126. Miniarikova, J. *et al.* AAV5-miHTT gene therapy demonstrates suppression of mutant huntingtin aggregation and neuronal dysfunction in a rat model of Huntington's disease. *Gene Ther.* **24,** 630–639 (2017).